Andreas Westermoen

Modelling of Dynamic Arc Behaviour in a Plasma Reactor

Thesis for the degree of philosophiae doctor

Trondheim, March 2007

Norwegian University of
Science and Technology
Facuty of Natural Sciences andTechnology
Department of Material Sciences and Engineering

NTNU
Innovation and Creativity

NTNU
Norwegian University of Science and Technology

Thesis for the degree of philosophiae doctor

Facuty of Natural Sciences andTechnology
Department of Material Sciences and Engineering

ISBN 978-82-471-0816-1 (printed ver.)
ISBN 978-82-471-0833-8 (electronic ver.)
ISSN 1503-8181
IMT-report 2007:90

Doctoral Theses at NTNU, 2007:38

Printed by Tapir Uttrykk

Acknowledgements

Den største takken går til Jon Arne Bakken for fire år med tett samarbeid, god veiledning, inspirasjon, smittende entusiasme, god humor, side på side med håndregnede ligninger og betrakninger, nitidig bepirking av alt jeg har skrevet, utallige kaffekopper med tilhørende diskusjoner, samt for å vise at man kan finne balansen mellom arbeid og moro.

Takk til alle som har vært innom PPM-prosjektet på Sintef i løpet av tiden der. Takk til Benjamin Ravary for opplæring og samarbeid på modelleringsiden. Takk til prosjektleder Bodil Monsen for å alltid ta seg tid, for å holde orden på alle løse tråder, for all oppmuntringen og for det gode humøret. Takk til Roar Jensen for gode diskusjoner og hjelp til å se sammehengene mellom eksperimentelle og beregnede resultater. Takk til Ola Raaness for å dele sin erfaring og for gode tips og tilbakemeldinger i diverse sammenhenger.

Takk til Merete Tangstad som plutselig fikk veilederansvaret, og som har gjort den tunge jobben med å kreve tidsplaner, effektivitet og resultater der hvor jeg og Jon Arne drev avsted på digresjon etter digresjon.

Takk til Gudrun Sævarsdottir, Hilde L.Larsen og resten av Jon Arnes tidligere stipendiater for gode råd, gode avhandlinger og følelsen av å stå i en sammenheng. Takk også for at dere lærte meg at 'numerisk depresjon' er helt normalt og går over etter en stund.

Takk til min kone Solveig for å la meg bruke så mye tid på jobb, og for å overleve så mye fagprat hjemme og i andre sammenhenger. Takk også til resten av familien for støtte og evig optimisme i forhold til arbeidet.

Takk til Kantineteknikk-gruppa, stipendiatgjengen på prossessmetallurgi og alle kolleger i Alfred Getz vei for å gi meg et interessant, vennlig og stimulerende arbeidsmiljø. Takk til Hilde og Åse Lill for smil og varm kaffe på begynnelsen av hver arbeidsdag.

Takk til Kåre Olaussen for drilling i C++, C og Latex, verktøy som har vært sentrale i Ph.D-arbeidet. Takk til strømningsgruppa på Sintef for hjelp og tips med Fluent.

Til slutt, takk til Norges Forskningsråd og Sintef-ledelsen for finansiering og videreføring av PPM-prosjektet. Uten deres finansielle støtte hadde ikke dette arbeidet vært mulig.

Symbols and abbreviations

The following list includes most of the used symbols and abbreviations.

Abbrevations:

AC	Alternating Current
CFD	Computational Fluid Dynamics
CNT	Carbon Nanotubes
DC	Direct Current
IMPC	Integral Method of Partial Characteristics
LTE	Local Thermal Equilibrium
MFD	Magneto-Fluid Dynamic
MFD-β	reference to the MHD-β model (ch.3)
PPM	Plasma Production of Materials (Sintef research prosject)
SD, SD-I, SD-II	ref. to the Source Domain models (ch.5)
UDF	User-Defined Functionality
UDS	User-Defined Scalar equation
VP, MFD-VP	ref. to the Vector Potential models (ch.4)

Greek letters:

β	Shorthand notation for rB_θ	[T m]
β_{inf}	The value of β outside the current distribution	[T m]
Γ	Diffusivity	[m^2/s]
Γ_m	Magnetic diffusivity $1/\mu_0\sigma$	[m^2/s]
ϵ_0	Electric permeability of vacuum	[A^2 s^4/kg m^3]
λ_D	Debye length	[m]
μ	Molecular viscosity	[Pa s]
μ_{eff}	Effective viscosity for a turbulent system	[Pa s]
μ_0	Magnetic permittivity of vacuum	[kg m/ s^2A^2]
ν	Kinematic viscosity	[m^2/ s]
ρ	Mass density	[kg/m^3]
ρ_e	Charge density	[C/m^3]
σ	Electrical conductivity	[S/m]
Φ	Electric potential	[V]
ϕ	(in ch.8) Deflection angle	[1]
ϕ_i	(in ch.3) Scalar variable in the general UDS equation	
ω, ω_0	Angular frequency, characteristic frequency	[1/s]

Latin letters:

$\vec{A}$, A_i	Electromagnetic vector potential	[T m]
$\vec{B}$, B_i	Magnetic flux density	[T]
C, c_0	Constants	[1]
C_p	Specific heat capacity	[J/kg K]
$\hat{C}_p$	Molar heat capacity	[J/mol K]
c	Speed of light	[m/s]
c_e	Expansion parameter for prescribed arc-shape	[1]
$\vec{D}$	Electric displacement	[C/m^2]
$\vec{E}$	Electric field strength	[V/m]
E	Energy (average kinetic particle energy)	[J]
e	Electron charge	[C]
$\vec{F}$, F_i	External force (after ch.1: Lorentz force)	[N]
$\vec{H}$	Magnetic field strength	[A/m]
h	Specific enthalpy	[J/kg]
I	Electrical current	[A]
I_{tot}, J_{tot}	Total arc current	[A]
I_ν^{Bb}	Planck function for a black body	[W/m^2]
J_{eq}	Equilibrium current	[A]
$\vec{j}$, j_i	Electrical current density	[A/m^2]
k	Thermal conductivity	[W/m K]
k_{eff}	Effective k for a turbulent system	[W/m K]
k_B	Boltzmann constant	[J/K]
l, l_0	Lengthscale, characteristic lengthscale	[m]
n_e	Electron number density	[1/m^3]
Pe	Peclét number = $RePr$	[1]
Pr	Prandtl number = $C_p\mu/k$	[1]
p	Pressure	[Pa]
p_e	Electron pressure	[Pa]
R, r	Radius	[m]
R_c	Cathode spot radius	[m]
R_{eff}	Effective radiation reabsorbtion radius	[m]
Re	Reynolds number = vl_0/ν	[1]
Re_m	Magnetic Reynolds number = vl_0/Γ_m	[1]
S	(in ch.9) Geometric scaling factor	[1]
S_i	Source term for fluent UDS equation	
S_{rad}	Radiation source term	[W/m^3]
ΔSim	*Partial characteristic* in the IMPC model	
Som	*Partial characteristic* in the IMPC model	
T	Temperature	[K]
t	Time	[s]
U	Voltage	[V]
$\vec{v}$, v_i	Velocity	[m/s]

Contents

Chapter 1

Introduction and background

1.1 What is this work all about?

This thesis is about modeling of electric arcs in a plasma reactor. Focus for the PhD work was twofold: The first task was to develop and implement a model in Fluent 6 that could simulate 3D dynamic arc behaviour, especially rotation motion due to an external magnet field. The second task was to support the design and operation of the reactor in the Sintef PPM project. This included investigating temperature and flow patterns for various geometries, an investigation of helium and helium-carbon mixtures as plasma gas, and in the later stages investigations of stability and control in rotating arc motion.

The results presented in this thesis and on the attached CD include cases with different dynamic behaviour (extinction and re-ignition, stable and unstable rotation, linear deflection due to magnet field or external gas flow), test cases to compare different models, test cases to compare different plasma gases, and cases with direct relevance to the PPM project.

1.2 The plasma state

We start with a definition of plasma [9]:

A plasma is a quasineutral gas of charged and neutral particles which exhibits collective behaviour

This definition tells us three important things about plasmas: First, and most obviously, plasma contains charged electrons and ions. This gives it the ability to conduct electricity, which is the most useful characteristic from the viewpoint of process met-

allurgy and chemical engineering.

The ionisation can be caused by two effects: very low pressure or very high temperature. In this work, only *thermal plasmas* will be addressed, i.e. plasmas generated by very high temperatures at near-atmospheric pressure. Cold plasmas (low-pressure plasmas) are not as interesting for metallurgical systems and can not be modeled with the same underlying assumptions as thermal plasmas.

Second, the definition states that the plasma is quasineutral. Significant deviations from neutrality can only occur within a length scale given by the *Debye length*

$$\lambda_D = \sqrt{\epsilon_0 k_B T / e^2 n_e} \tag{1.1}$$

where k_B is the Boltzmann constant and T, e and n_e are electron temperature, charge and density, respectively. Although things get a bit more complicated near electrode surfaces, the bulk of the plasma can be treated as electrically neutral as long as the characteristic size for the arc is much larger than the Debye length. A typical value of λ_D for the PPM arc plasma is 0.03 μm

Third, plasma has a *collective behaviour*. To get an understanding of this, normal kinetic gas theory is not sufficient: In addition to ionization and recombination reactions, the charged particles act on each other with electrostatic forces. Finally, all charged particles contribute to electric currents flowing in the plasma and thereby to a magnetic field affecting all other charged particles.

These forces are the ones that keep the tiny electrons from just passing between the heavy particles and escape the system. Instead, the charged particles tend to stick together. When applying some external condition to a plasma, the response of the individual particles is always modified by the total magnetic and electric field of all the charged particles, giving the collective behaviour.

The tiny mass of the electron still makes for problems, however. Because of the relative collision cross section sizes, heavy particles collide with each other all the time while electrons effectively only collide with heavy particles. In an elastic collision between two equal masses the energy is distributed evenly afterwards, but in collisions between electron and ion, the electron loses very little of its energy. Therefore electrons need multiple collisions in order to get their energies averaged, and their temperature distribution will be wider than that of the heavy particles.

1.2.1 Temperature concept and LTE

At this time, it may be a good idea to review our understanding of temperature. Temperature is defined by Boltzmann from the average kinetic particle energy

$$E = \frac{3}{2} k_B T \tag{1.2}$$

But because of the different collision rates, or because of electric fields causing currents, the electrons and the heavy particles *may have different Maxwellian distributions* and thus different temperatures. In a typical fluorescent light tube, electron temperatures can reach maybe 2000 K, while the heavy particles are just above room temperature. To successfully model this, we need a model with two temperatures.

On the other hand, if the pressure is high enough, collision rates will be high and the temperature will be the same for all species: we get *Local Thermal Equilibrium* (LTE). In this work, like in so many others, we assume that we have LTE in the whole plasma and thus need *only one temperature*, the so-called plasma temperature. This is one of the most critical assumptions for the models, and there will be further discussion of this later.

1.2.2 Electric arcs

As defined above, the term plasma is broad in the sense that it covers all cases of ionized gases, whether caused by low pressure, high temperature or induced by rapidly oscillating magnet fields. In this work, as in metallurgical industry, we will focus only on electric arcs. Electric arcs, or plasma arcs, are powered by a high current being driven through the plasma, and the large resistive heating provides the energy for ionization.

It is customary to distinguish between *non-transferred* and *transferred* arcs. In the non-transferred arc, the arc burns between two electrodes forming an electrode assembly, and typically gas blows the plasma plume outwards to make a so-called plasma jet. The anodic electrode is often shaped as a nozzle.

In the transferred arc, the material to be processed also functions as anode, and the plasma zone follows the current. Figure 1.1 is more illustrative.

From a modeling point of view, these cases are the same in the sense that all the equations for the plasma phase are identical. The difference is that transferred arcs generally are well-behaved, with near-symmetric current distributions and velocities mainly following the arc, whereas the non-transferred arcs generally have a more complex shape. Therefore, only very special non-transferred arcs can be successfully modeled by a 2D model. For a true 3D model, though, the differences lie only in the boundary conditions and not in the model itself. Note though that for a transferred

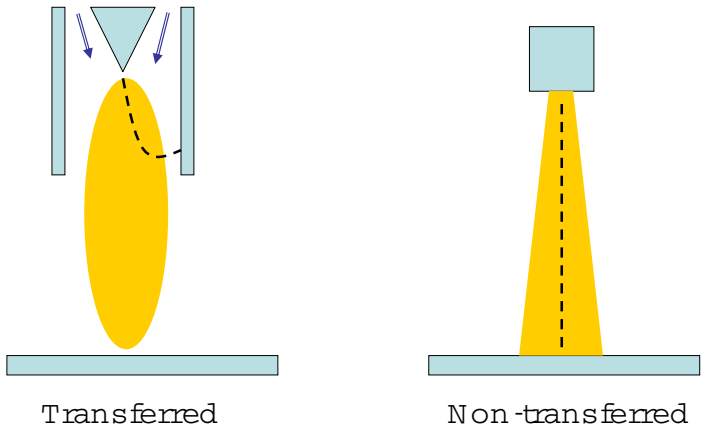

Figure 1.1: Conceptual transferred and non-transferred arc. The dashed line illustrates the current path

arc burning against a molten metal pool, the model must be expanded to take into account anode deformation due to electromagnetic and mechanical forces acting on the liquid metal[30].

The arcs modeled in this work are all transferred arcs, and are based on the assumption that we know the position and radius of the cathode spot as well as the total current through the arc. For our lab-scale arcs of about 1 kA, we assume a average current density in the cathode spot of around $10^7 A/m^2$.

1.3 Plasma arc processes in laboratory and industry

Plasma arc processes are attractive for the materials industry because the temperature generated by an electric arc is much higher than that obtained by gaseous flames. Electric Arc Furnaces (EAF) have been used in steel making since Siemens started in 1878, and are still used throughout the world for steel making. Other applications include Submerged Arc Furnaces (SAF) for silicon and ferrosilicon production, as well as scrap metal remelting, metal refining and tundish and ladle heating. Plasma torches are used for cutting, welding and spray coating. In addition, arc technology

is ideal for destruction of all kinds of hazardous materials. Newer applications of the technology include particle spheroidisation and solidification, as well as production of nanoscale powders and structures.

Crudely put, the extreme temperature available in an electric arc makes it useful for anything that needs to be melted or vapourised quickly. The drawback of the technology is that the temperature in the arc may be too high for the wanted reagents. In the Sintef PPM project described below, a constant danger is that uncontrolled arc spots may well pass over deposited nanotubes and vapourise them.

For a more complete overview of the different applications and research on thermal plasmas, E.Pfender's overview [46] from 1998 is still recommended.

1.4 The Sintef PPM project

This whole work has been done as a part of the Sintef Strategic Institute Project "Plasma Production of Materials" (PPM). The aim of the PPM project is to develop a commercial method for industrial production of carbon nanotubes (CNT). The project is financed by the Norwegian Research Council and Sintef.

The PPM project combines several areas of expertise. Designing, constructing and operating a plasma arc reactor is the first field. A good understanding of arc behaviour and processes inside the reactor is another. Analyzing, separating and quantifying the produced material is a third. Numerical simulation of arcs and transport processes in the reactor is a fourth. In addition, cooperation, organization and communication skills were critical for the success of the project.

The modeling work for the process forms the basis of this work. In the design phase of the project, emphasis was on developing the fast, cheap Source Domain (SD) model that could investigate qualitative differences between different proposed geometry variants. Later, emphasis changed to updating and further developing the Magneto-Fluid Dynamic (MFD) model used in the group's previous modeling work. After encountering big difficulties with generalising the model to 3D, work started on finding a robust numerical model that in principle can model all types of arc behaviour. The result was the Vector Potential (MFD-VP) model which is also a MFD model, but solves the equations for the electromagnetic vector potential rather than for the magnetic field.

1.4.1 Why a plasma process?

The reason for choosing a plasma process for CNT production (instead of say chemical vapour deposition) has to do with scaling. Simply put, most other processes

will encounter problems of some kind if trying to upscale. Some methods require very detailed control and thus a lot of manpower, other methods only work on small scales. Using a thermal plasma method has the advantage that evaporating large amounts of carbon just needs a bigger reactor with more current. Similarly, recondensing large amounts of carbon vapour should be possible with some large cooled surfaces, it is just a matter of finding the right conditions so we get CNT instead of f.ex. amorphous carbon. So even if other methods perhaps are better at a lab-scale, plasma processes are very strong contenders if the goal is to produce nanotubes per ton instead of per gram. Patent applications for the PPM process have been sent nationally and internationally [62][63][64].

Another advantage of using a thermal plasma method is that the produced nanotubes typically are very straight with a good length-diameter ratio, as shown in figure 1.2).

1.4.2 Modeling for making nanotubes?

It is perhaps not obvious why developing a model for a rotating arc is necessary in order to produce carbon nanotubes. The connection is process control. What reactor parameters give best yield is found through experiment, but to understand what thermal conditions these represent, we need modeling. When proposing a change in the operating or reactor geometry, simulations can estimate how the thermal conditions change, making the experimental investigation more systematic. Finally, to reach the goal of industrial scale production, we need to know how conditions change due to upscaling - a very expensive task if done in the lab instead of on the computer.

1.5 Arc modeling: what have others done?

Modeling of electric arcs is almost as old as the first electric arc furnace or electric arc welders. But until computing power became inexpensive, focus was on modeling the arc as an element in an electric circuit. Modeling of the heat and momentum transport inside the reactor did not develop significantly until the eighties.

1.5.1 Prescribed-current models

The oldest type of model for investigating the inside of a furnace is by assuming a known current distribution in the whole arc. This type of model was used by Ramakrishnan et al.[47] in 1978, and has been used later to investigate simple DC arcs [2][30][32] and to approximate dynamic arc systems [43].

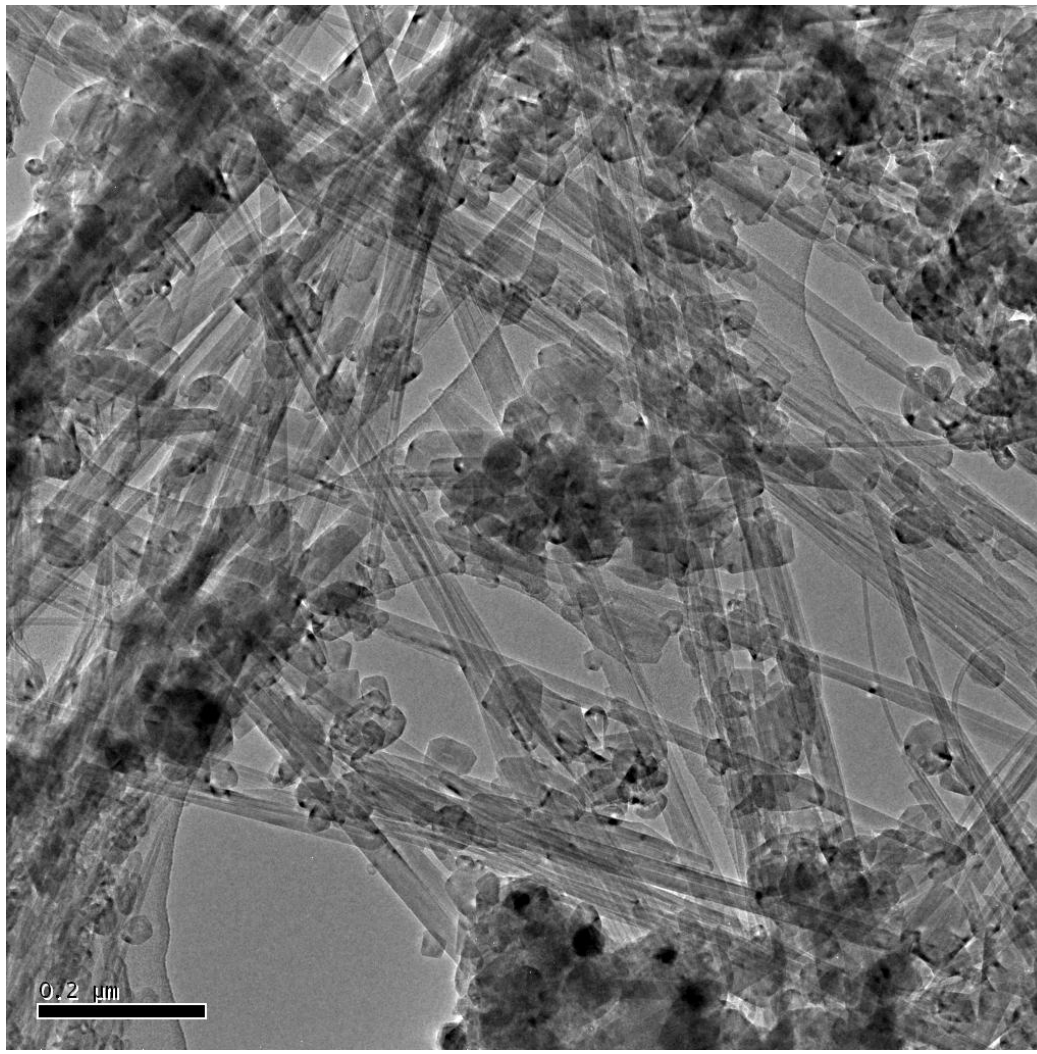

Figure 1.2: Carbon Nanotubes produced in the PPM project

1.5.2 Electric potential models

This type of model is based on solving the electric potential and calculating the current from this, then integrate the magnetic field from the given current. This functions well in axisymmetric DC arcs and has been used in various works [30][33][34][42].

1.5.3 The "MFD-B model"

A new generation of arc model is the MFD-B model where a transport equation is solved for the B field. This model was implemented by H.L.Larsen[40], and was further developed by G.A.Sævarsdottir[51]. It can model transient effects in AC arcs, but only for axisymmetric cases.

1.5.4 Vector potential models

The concept here is to solve transport equations for the electromagnetic scalar and vector potentials instead of for the B field. This type of model has been widely used in the recent years for different applications. Groups in Chatou ([14][15]), Minnesota ([35][38][45]), Bejing ([10][35]), Bologna ([11][12][13][26]) and Sherbrooke ([6]) have all developed 3D transient codes for investigation of different arc phenomena. Much focus has been on anode behaviour and downstream conditions in plasma torches, but also on more general investigations of deflection by external gas flow[38], magnetic fields [6], electrical instabilities [16], LES turbulence modeling [14] and non-LTE plasmas [10]. Another inspiration for this work was the simulation by Dr.Toh [56] of an arc controlled by a AC magnetic field .

1.5.5 Rotating arcs

To the authors knowledge at the time of writing, no publications had been made for simulation of rotating arcs. A theoretical model [18] and experimental results exists for coaxial systems with metal electrodes, but it is not applicable to the PPM reactor geometry or to carbon electrodes.

1.6 Which cases to investigate, and why

One of the main goals of this work was to develop a code that could in principle simulate *any* kind of arc behaviour (in a LTE plasma). However, certain classes of cases are much faster to solve with specialized models. Some 'standard cases' are required to compare the different models to each other and to experiments, and cases that resemble the real PPM reactor were more directly useful for that project.

1.6.1 Different problem classes

Stationary, symmetric cases

Investigating these basic cases is very important. The most obvious reason is to validate models against previously published results for the symmetric cases. This also means that models can be compared with each other for these cases.

Obviously, symmetric cases can be solved in 2D for much faster investigations of many effects, but only if we are really sure that the solution is symmetric.

Non-symmetric cases

The difference between a small and large deviation from symmetry is often only dependent on how far outside the arc our domain reaches. For the 'almost symmetric' cases, boundary conditions and some assumptions may be much safer to make. On the other hand, a larger domain means longer computation times. A code that only manages to solve for small deviations is not acceptable though, so the focus in the 3D model has been the truly non-symmetric cases. Note though that cases with symmetric geometry and symmetric boundary conditions may very well have non-symmetric (and transient) solutions!

Transient cases

Stationary solvers are fine for validation and for the simplest cases, but all the really interesting effects are transient. Again, stationary boundary conditions may very well give a time-dependent solution (such as rotation). The transient solver may in many stationary cases have a faster convergence than the stationary one, and experience shows that it is often a good idea to use a similar case as the initial solution, then use a transient solver to let the arc adapt to new conditions.

1.6.2 Physics vs engineering: what information do we want?

To decide what cases to simulate, we must know what information we want. From the perspective of testing the model, the perhaps most interesting parameter is the current distribution and how it is affected by various phenomena. Anode spot behaviour, arc deformation due to rotation, anode constriction, extinction and re-attachment are all very interesting phenomena to investigate when we want to understand the physics of the arc. Proving that our model can simulate such phenomena is then very tempting.

For the engineer designing or operating the reactor, the picture is very different. Now, the focus is on process control: we would rather avoid instabilities than study them. The important parameters are the voltage drop and total power of the arc,

the gas flow pattern and velocities, and how the temperature is distributed on the reactor volume and on the surfaces. Because operation parameters are changed dynamically to counter changes in arc behaviour, it can be very difficult to reproduce actual experimental results with a complicated model. On the other hand, because the arc is kept actively under control, it is possible to assume a stationary solution and perhaps to use simpler models.

In the PPM project, the novel idea is that a rapidly rotating arc will create a voluminous plasma zone and thus make it easy to evaporate carbon in-flight. At the beginning of the project, there was no model capable of simulating arc rotation, and the work started in two directions simultaneously. The short-term aim was to update existing models and produce 'engineering results' based on the assumption that the arc was rotating fast enough to be treated like a symmetric hollow cone. For the 2D calculations, the focus is on how gas flow patterns and temperature distributions are affected by changes in geometry and arc current. The long-term aim was to make a model that could simulate rotation. For the 3D transient calculations, the focus is then on how the current distribution is affected by external forces or non-symmetric geometry.

1.7 Energy and momentum transport: common ground for the models

The model descriptions in later chapters deal only with the electromagnetic part of the models: computing the time-varying current and the electromagnetic field distributions needed to calculate resistive heating and magnetic forces. But of course we also need to solve the equations for momentum and energy transport. Using a commercial code as basis for our implementation has the advantage that these equations are already included and optimised. An overview is in order though, to give a more complete picture of the models used:

Momentum can be transported by convection and diffusion. Momentum is generated by pressure difference and external forces, and can dissipate due to friction and turbulent breakdown. Assuming a Newtonian, incompressible fluid[1], the standard (Navier-Stokes) momentum equation straight from the book [5] reads:

$$\rho\left(\frac{\partial\vec{v}}{\partial t}+(\vec{v}\cdot\nabla)\vec{v}\right)=-\nabla p+\mu_{eff}\nabla^2\vec{v}+\vec{F} \tag{1.3}$$

where $\vec{F}$ is the sum of all external forces - normally only $\rho\vec{g}$, and μ_{eff} is the effective viscosity, i.e. the sum of molecular and turbulent viscosities.

[1]For industrial-scale arcs, compressibility effects should be included like in [51].

Gravity is the only external force taken into account in normal fluid mechanics software, so the electromagnetic (Lorentz) force acting on our plasma must be included as a source term. Neglecting gravity so that the Lorentz force, $\vec{j} \times \vec{B}$, is the only external force, the momentum equation becomes

$$\rho \left(\frac{\partial \vec{v}}{\partial t} + (\vec{v} \cdot \nabla)\vec{v} \right) = -\nabla p + \mu_{eff} \nabla^2 \vec{v} + \vec{j} \times \vec{B} \tag{1.4}$$

or, conceptually:

(momentum change) = - (pressure force) + (friction force) + (source term)

where the source term, $\vec{j} \times \vec{B}$, must be supplied from the outside (i.e. through extra equations added to the Fluent solver).

Energy is governed by the same type of transport equation. Convection, conduction, and generation of heat combine to give the energy equation

$$\rho \left(\frac{\partial h}{\partial t} + (\vec{v} \cdot \nabla)h \right) = \nabla \cdot (k_{eff} \nabla T) + S_{tot} \tag{1.5}$$

Similar to above, the k_{eff} is the sum of laminar and turbulent heat conduction. Fluent does not use enthalpy directly in these equations, but makes the assumption that $h = \hat{C}_p T$ i.e. that the enthalpy difference between two cells is proportional to the temperature difference (but with a proportionality constant that can depend on temperature). Pressure gradients are assumed to be so small that the pressure dependence of the enthalpy and k is negligible, and $k_{lam} >> k_{turb}$. Finally, we must assume that the k gradient is small between two adjacent cells so that the $\nabla T \cdot \nabla k$ term vanishes. The energy equation solved by Fluent is then

$$\rho \hat{C}_p \left(\frac{\partial T}{\partial t} + (\vec{v} \cdot \nabla)T \right) = k \nabla^2 T + S_{tot} \tag{1.6}$$

In our case, the heating source term consists of Ohmic heating j^2/σ, but also emitted radiation S_{rad}. In addition to these, we want to add a different type of heat transport: that of electron diffusion. This is caused by the fact that the current carrying electrons in our system can transport energy by moving between atoms. The effect of this is a source $\frac{5}{2}\frac{k_B}{e}(j_r \frac{\partial}{\partial r}T + j_z \frac{\partial}{\partial z}T)$, and must be included in the total source term S_{tot} together with radiation and resistive heating.

The energy equation in our arc models is then 1.6, where the source term that must be added is

$$S_{tot} = \frac{j^2}{\sigma} + S_{rad} + \frac{5}{2}\frac{k_B}{e}\left(j_r \frac{\partial T}{\partial r} + j_z \frac{\partial T}{\partial z} \right) \tag{1.7}$$

1.8 Using FLUENT on thermal plasmas

All simulations in this work were done using Fluent 6.0, 6.1 or 6.2 versions. Fluent was chosen because of the high expertise available in Sintef, and because the previous MFD codes were written in Fluent. However, the old codes were implemented in Fluent version 2.97 with access to the source code[2], and it was not possible to transfer them to version 6.0. The code used in this work then had to be made from scratch.

1.8.1 Fluent MHD package

Fluent 6 has an optional MHD package. However, closer inspection reveals that although it is perfect for simulating magnetic effects in molten metals, it is not usable on plasmas. Specifically, the equations include an assumption that the magnetic diffusivity (effectively the inverse electrical conductivity) is constant or only slowly varying. In thermal plasmas, this parameter can change by two orders of magnitude over a few millimeters. So the conclusion was that this package could not do the work for us.

1.8.2 Fluent UDF methods

The only option left then was to feed Fluent with User-Defined Functions (UDF). Fluent 6 has a procedure for this (fortunately much improved from 6.0 to 6.2), and any equation can be imported if it fits on a standard transport equation form. Material data and boundary conditions were also included in the UDF code, except for heat capacities that must be manually added into the Fluent materials database.

Basically, the UDF code is a C/C++ code [48], but is compiled inside Fluent (in 6.2 version) and uses specific macros to communicate with the Fluent core program. Refer to the fluent documentation [22] for details.

1.8.3 Turbulence and other features

In all the cases presented here, *laminar flow has been assumed*. However, any turbulence model included in Fluent 6.2 can simply be turned on for the arc model. For some of the axisymmetric 'standard cases' different turbulence models were compared, and the conclusion was that turbulent effects were negligible.

Similarly, for tracing particles in the flow field around the arc, simply turn on the Discrete Particle Model included in Fluent. Basically anything Fluent can do on normal fluids can be done on plasmas.

[2] by special arrangement, Fl 2.97 was never an open source code.

1.8.4 Parallellisation

The UDF code is not written for multiple processor interface (MPI), and thus the cases must be solved on a single computer. In theory it is possible to modify the code to MPI, but that was outside the scope of this work.

Chapter 2

Material properties

2.1 Calculation of material properties

The thermodynamic properties and transport coefficients used in this work were obtained from several sources. Most importantly, all data for Helium and He-C mixtures were computed by a tailor-made code CHECOMP[31] by Dr. Gu Liping. The computed composition was compared to that computed as a part of Dr. V.G.Sevastyanenko's radiation data program[49] and is shown in figure (2.1.1). The transport coefficients for He were compared to tabulated values in the book by Pfender/Bolous/Fauchais [21]. For Argon gas, the same data was used as in previous work in the institute [40][51].

2.1.1 Computing plasma composition

All the sources compute their data in the same general way, by first computing the equilibrium composition of species at a given temperature and pressure, and secondly computing the transport data from the composition.

For instance, the relatively simple pure He plasma consists of four species: He, He^{+}, He^{2+} and e^{-} . In this system it's obvious what reactions can take place, and given tabulated ionization energies for the different species, we can calculate the equilibrium composition in the normal way. For a mixed He-C or Ar-C system (we need carbon vapour to make nanotubes), the number of species and reactions increases severely, but the methodology is the same.

The CHECOMP code calculates ionization energies taking into account micro-electric fields in the plasma (Debye-Hückel model), and must be considered state-of-the-art for computing plasma composition. The radiation data program produces results that deviate a little from the CHECOMP results, but the deviation is small compared to the other assumptions we will make about radiation.

The code calculates composition at any specified pressure. In this work, a standard operating pressure of 0.6 bar is used as default for the He cases, as this is the operating pressure of the PPM reactor. The reason for choosing that particular pressure has to do with experiences from other projects on carbon nanotube production [24].

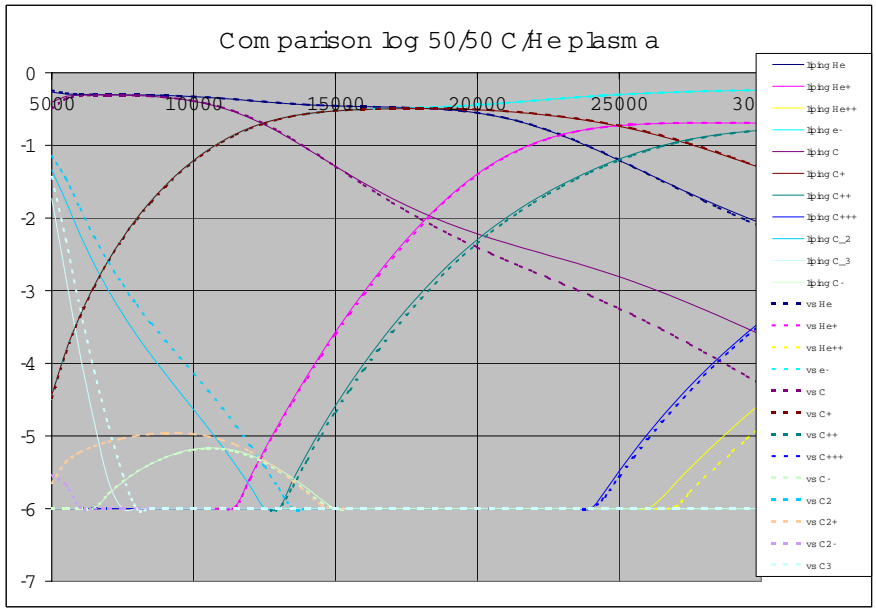

Figure 2.1: Plot of species composition of a He-C mixture as function of temperature. Logarithmic mole fractions. The whole lines are from Dr. Gu Liping's program ('liping') to compute transport properties, the dashed lines are from Dr. V.G.Sevastyanenko's program ('vs') to compute radiation.

2.1.2 Computing thermodynamic properties and transport coefficients

When the composition is known, the thermodynamic properties can be calculated. Mass density is simply the number densities multiplied by the mass of the species. Enthalpy is calculated from the partition function of each species, and then summed over all species. Specific heat is derived from the enthalpy.

For the transport properties, things are a bit more difficult. Classical kinetic theory cannot be used as species are charged and react with each other. Neither do we know any reliable mixing rules for the plasma systems. In essence, we have a very complicated Boltzmann equation to solve and cannot use the normal tricks. What we *can* do, is to split the Boltzmann equation in two parts: one for the electrons and one for the heavy particles. Because the mass ratio of electron to heavy particles is so low, their collision terms can be neglected from the heavy-particle equation and vice versa. The CHECOMP uses this method, as developed by Devoto[17], and uses 3rd order approximations for electrical conductivity and electron translational thermal conductivity, 2nd order for heavy particle translational thermal conductivity and 1st order approximations for all other transport coefficients.

For more technical data about how the various properties are computed, refer to the documentation of the CHECOMP code[31].

2.2 The calculated plasma properties

Plots of various thermodynamic properties and transport coefficients for Ar, He, SiO+CO (1:1 mol fraction) and C systems, all at 1bar. Data for He at 0.6 bar and 0.3 bar and 1 bar He-C mixtures (1:9 and 1:1 mol fraction) are included at the end of this chapter. No simulations with SiO+CO or pure C was done in this work, these data are included to help comparison with other's work [30][51][40].

Density ρ

See figure 2.2 for comparison between different plasma gases and figure 2.14 for investigation of He-C mixtures.

Electrical conductivity σ

See figure 2.3 for comparison between different plasma gases and figure 2.15 for investigation of He-C mixtures.

Thermal conductivity k

See figure 2.4 for comparison between different plasma gases and figure 2.16 for investigation of He-C mixtures.

Viscosity μ

See figure 2.5 for comparison between different plasma gases and figure 2.17 for investigation of He-C mixtures.

Enthalpy h and heat capacity C_p

Specific enthalpy is the parameter calculated, but Fluent needs data for specific heat capacity. The heat capacity shown here is just $\Delta h/\Delta T$ for each interval. See figures 2.6, 2.7 for comparison between different plasma gases and figures 2.18, 2.19 for investigation of He-C mixtures.

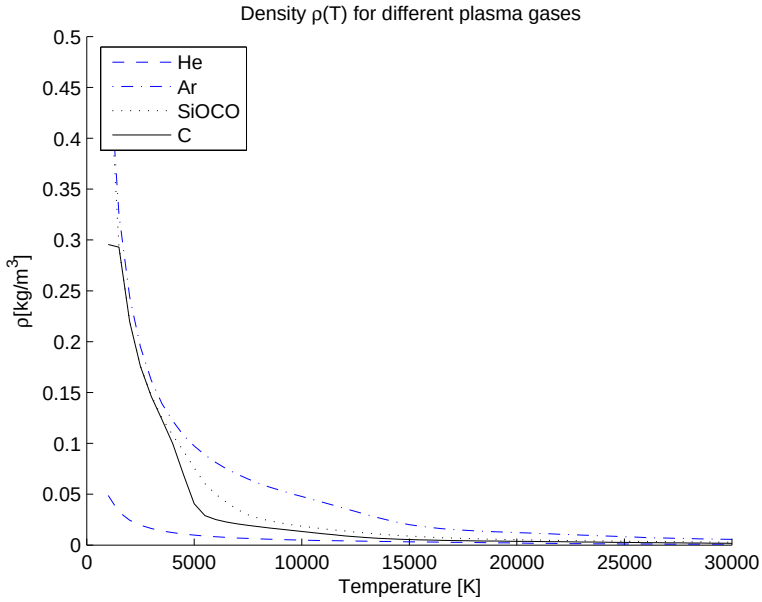

Figure 2.2: Density [kg/m^3] as function of temperature for different plasma gases

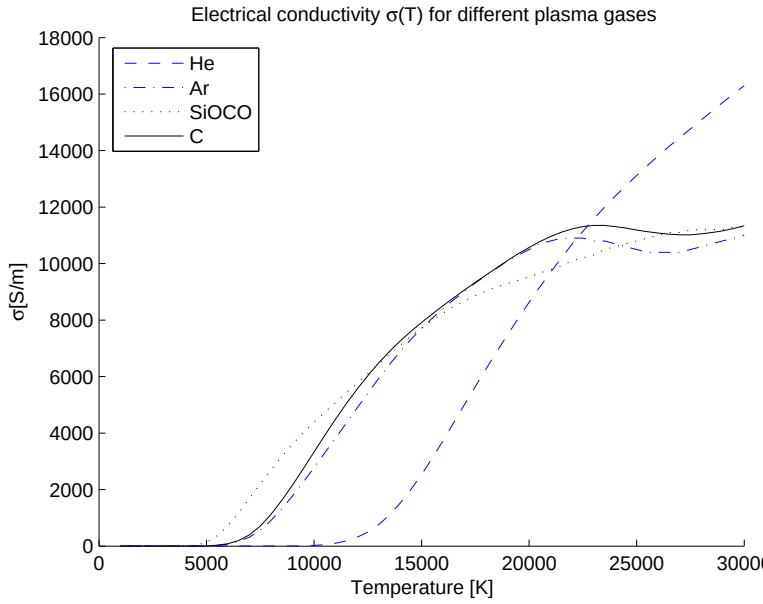

Figure 2.3: Electrical conductivity [S/m] as function of temperature for different plasma gases

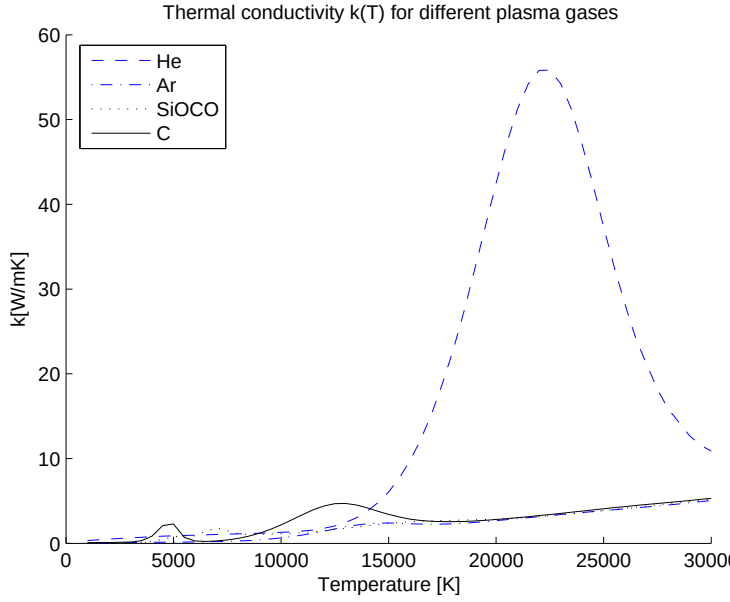

Figure 2.4: Thermal conductivity [W/m K] as function of temperature for different plasma gases

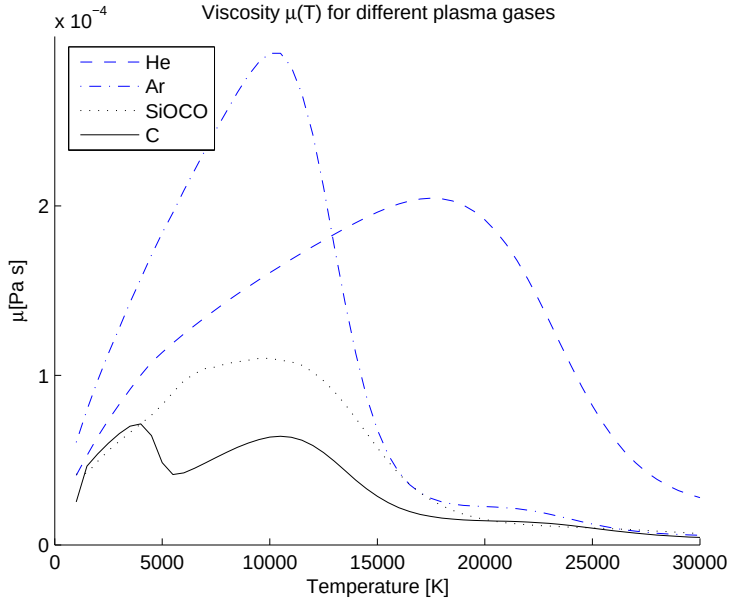

Figure 2.5: Viscosity [Pa s] as function of temperature for different plasma gases

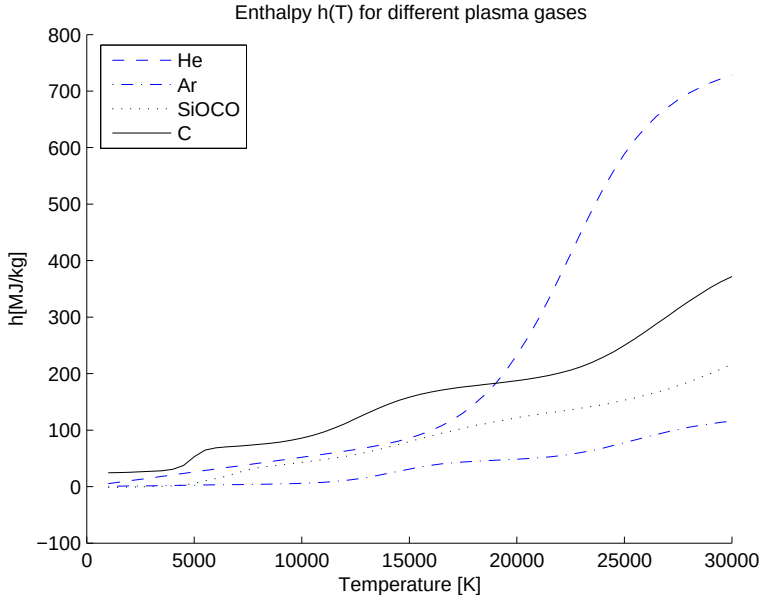

Figure 2.6: Specific enthalpy [J/kg] as function of temperature for different plasma gases

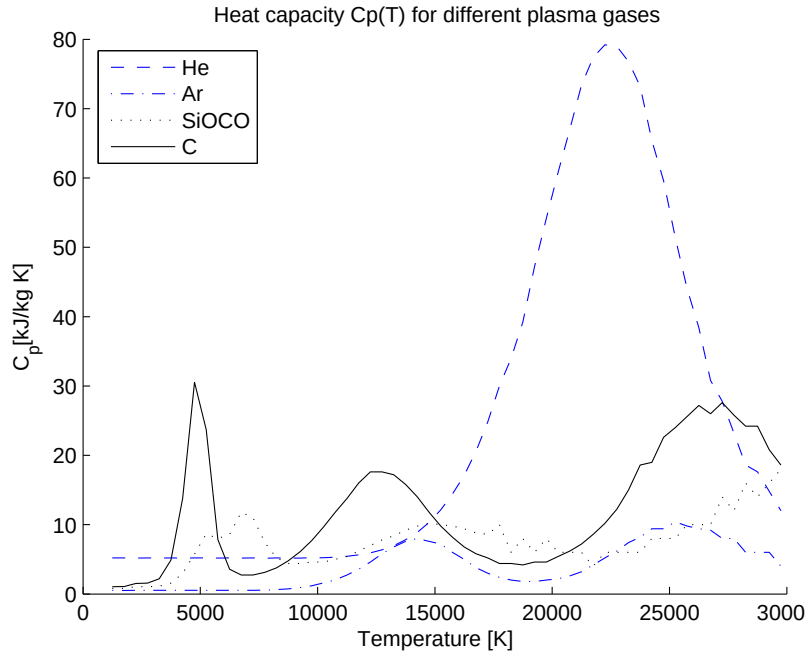

Figure 2.7: Specific heat capacity [J/kg K] as function of temperature for different plasma gases

2.2.1 Data format, gradients and numerical pitfalls

All CHECOMP computed thermodynamic properties are given as vectors of values for given temperatures. Specifically, values were given for temperatures [1000 K, 1500 K, 2000 K, ..., 30000 K]. Radiation density values were given for [5000 K, 6000 K, ..., 30000 K]. Simple linear interpolation was used between the points, either explicitly in the UDF code or implicitly by entering data as piecewise-linear tables directly into the Fluent materials database.

For certain expressions and models, gradients of transport coefficients were used (mostly conductivity gradient). The piecewise-constant gradient derived from the tabulated values is not continuous, and may cause some rounding error around specific temperatures. For the MFD model, the gradient of the magnetic diffusivity Γ_m was used, computed from tabulated σ values, resulting in a seemingly piecewise-hyperbolic temperature dependence for Γ_m.

Near the electrodes, temperature gradients are large. This also gives large gradients for all transport coefficients. Normally, one would want a high cell resolution at these places. However, testing indicates that too abruptly varying cell sizes introduce much more error than the gradients do. Also, for an unstable or periodic moving arc, the grid would have to be adapted in time, contributing significantly to the number of things that can go wrong. Another issue for discussion is that of the LTE (see below); at the regions of high gradients, the real electrical conductivity and radiation will deviate some from the computed ones. The smaller the cells, the greater the effect of this error. For the computations in this work, a homogenous grid was found to be the most trustworthy. Still, one must be aware of this dangerous territory and consider it every time a model is improved: suddenly we may have reached the point where these errors are the biggest remaining obstacle.

2.3 Radiative heat transfer

In electric arcs, with their extreme temperatures, radiative heat transfer is highly important. As usual, the real situation is quite complicated, and when modeling we must reduce the problem to a manageable size.

The emitted energy density from a point in the arc depends on the local plasma composition and the temperature (and the pressure in some cases). This is maybe all we need to know if we assume that the gas in the reactor is optically thin for all wavelengths. But any gas heated enough to emit radiation will also absorb radiation; radiation from the (hottest) interior of the arc will be partly absorbed by the (slightly cooler) outer part of the arc, making the temperature more uniform inside the arc. To include effects like this, we must also keep track of the spectral distribution of

the radiation.

2.3.1 Net volumetric radiation density

Our radiation model then must start with the fundamental *net volumetric radiation density*, which is the net energy emitted per unit volume and time:

$$S_{rad} = \int_{4\pi}\int_{0}^{\infty}\left(I_{\nu}^{Bb}(x)k_{\nu}(x) - k_{\nu}(x)\int_{0}^{x} I_{\nu}^{Bb}(\xi)k_{\nu}(\xi)e^{-\int_{\xi}^{x} k_{\xi}(\eta)d\eta}d\xi\right)d\nu d\omega \quad (2.1)$$

Here, k_ν is the *spectral absorption coefficient* and I_ν^{Bb} is the Planck function for a black body:

$$I_{\nu}^{Bb} = \frac{8\pi h}{c^3}\frac{\nu^3}{e^{h\nu/k_BT}-1} \quad (2.2)$$

The integration for S_{rad} is over all frequencies ν, all directions ω and over all sources ξ on the ray from the domain boundary (ξ=0) to the point x under consideration.

2.3.2 Walls and particles

The water cooled reactor walls are assumed to be cold compared to the arc. Because the arc is thin compared to the reactor, reflection from the walls can be neglected. Also, the condensation of carbon on the walls makes the reflectivity low (and diffuse) in any case, so the reactor walls are considered as black surfaces. The only places in the reactor where the black-body assumption could be a problem is on the inside of the anode, where the arc is widest, geometry is narrowest and the deposited carbon may form a silvery, reflective structure.

A whole new level of radiation modeling is needed if one wants to take into account carbon particles (dust) in the reactor. A dusty plasma could be modeled as partly transparent, but as the temperature increases and the dust evaporates, the opacity changes. In this work we have focused only on pure gas-phase plasmas with uniform composition.

2.3.3 Advanced model: IMPC method

Figure (2.8) illustrates the concepts for the IMPC and for Lowke's simpler method described below.

The state-of-the-art radiation model for thermal plasmas and electric arcs is the *Integral Method of Partial Characteristics* (IMPC) developed by V.G.Sevastyanenko [50]. This was determined to be too computationally expensive for use in the 3D

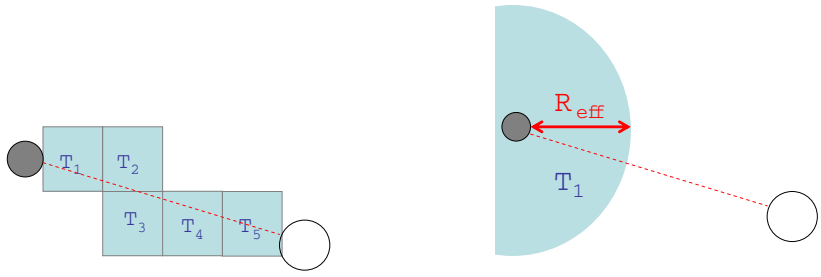

Figure 2.8: Concept of IMPC versus Lowke's method. In IMPC (left), absorption is calculated in every cell along the path from the source (dark) to the sink (white). In Lowke's method, absorption is calculated for a sphere of a given radius R_{eff}

models, but an overview is still given here as it is closely related to the simpler model that was used instead (and the computed radiation data for that model is taken directly from the IMPC model data).

Starting with the integral expression (2.1) for the net volumetric radiation density, we can manipulate it and get

$$S_{rad} = \int_{4\pi} \left(Som - \int_0^x \Delta Sim \, d\xi \right) d\omega \tag{2.3}$$

where the "partial characteristics" are

$$Som(T_x, T_0, x) = \int_0^\infty I_\nu^{Bb}(x) k_\nu(x) e^{-\int_0^x k_\nu(\eta) d\eta} d\nu \tag{2.4}$$

and

$$\Delta Sim(T_\xi, T_x, x-\xi) = \int_0^\infty I_\nu^{Bb}(\xi) - I_\nu^{Bb}(x) k_\nu(\xi) k_\nu(x) e^{-\int_\xi^x k_\nu(\eta) d\eta} d\nu \tag{2.5}$$

Now the whole point is that we can tabulate the Som and ΔSim prior to solving the transport equations. The partial characteristics will, in the low-current case (with no large pressure gradients), depend only on source temperature (T_ξ in ΔSim, T_x in Som), sink temperature (T_x in ΔSim, T_0 in Som) and the distance $x - \xi$between source and sink. For the plasma mixtures of interest in this work, these partial characteristics were computed by a code[49] written by V.G.Sevastyanenko for this

work. Using the tabulated values, one can then calculate the radiative heat transport between all pairs of cells in the domain, taking into account reabsorption within the plasma.

However, in 3D cases this method becomes extremely expensive, as it scales with the square of the number of cells. Assuming a homogenous grid, this means that with twice the linear grid resolution, we need 64 times the number of calculations for radiation. For a grid with a million cells, we need 10^{12} operations! Even if we design a clever scheme where radiation is only calculated in the cells where the gas is hot enough to actually emit radiation, the problem scales just as horribly. In order to get reasonable computation times[1] on a computer from 2005, we need to use a simpler model.

2.3.4 Simplified model: Lowke's method

Lowke [39] proposed a simpler approach: we model all radiation as being emitted in the center of an isothermal sphere with a characteristic *effective radiation radius* R_{eff}. Radiation can then be reabsorbed within this sphere, but only there. In essence, we imagine that radiation emitted in the arc has to pass through a certain distance of (not optically thin) plasma before escaping to the walls. By assuming that the sphere is isothermal, and by assigning it a radius, we remove two of the three variables from the IMPC equations, giving us a radiation term that depends only on the temperature of the cell considered.

This model obviously has some weaknesses, especially when considering that although the arc must be given a characteristic radiation radius, but it is in no way a spherical symmetric problem even for the simple stationary arcs, much less for a complicated transient arc. Also, a real arc can have areas in the outer part where the absorption of radiation from the inner parts is higher than the emitted radiation, effectively giving a negative radiation loss. In arcs with much carbon vapor, this effect could be important, but this cannot be modeled with Lowke's model.

On the other hand, we get only a simple tabulated constant energy source term in each cell, making this a 'free' calculation since the Fluent energy equation solver takes into account user-defined source terms.

So what is the source term? By assuming the spectral absorption k_ν and Planck function I_ν^{Bb} to be constant, and integrating from $r = 0$ to R_{eff} over all angles, we

[1] The IMPC method was used successfully on a computer from 1999, but computation times were much longer than 'reasonable'. Assuming a 100x100 grid in 2D versus a 100x100x100 grid in 3D, the radiation problem is 10 000 times larger in 3D.

get

$$S_{rad} = \int_{4\pi}\int_0^\infty \left(I_\nu^{Bb} k_\nu - k_n u I_\nu^{Bb} \int_0^{R_{eff}} e^{-k_\nu (x-\xi)} d\xi \right) d\gamma d\omega$$
$$= 4\pi \int_0^\infty I_\nu^{Bb} k_\nu e^{-R_{eff} k_\nu} d\nu = 4\pi Som(T, T, R_{eff}) \quad (2.6)$$

Thus the radiation data for Lowke's method can easily be calculated from the same code as for the IMPC model. In this work, a characteristic diameter of 0.89 cm was used for the arcs, corresponding to a parameter $y = 10^x = -0.05$ This seems very reasonable for stationary arcs, but results for rotating arcs show that the arc is severely deformed from the drag it experiences. This gives a longer characteristic length in one direction and shorter in the other, making this radiation model less than ideal. Choosing a smaller characteristic reabsorption length will give less absorption and hence higher radiation loss and vice versa.

2.3.5 Computed radiative energy loss

See figure 2.9 for comparison between the emitted radiation densities for different plasma gases and figure 2.20 for investigation of He-C mixtures.

2.4 The LTE assumption

2.4.1 The physics

When making computations on plasma, it is by far the easiest to treat the plasma as fluid with composition and properties depending only on temperature (and pressure). This will be the case if all the species in the plasma share the same temperature. However, reality is as usual more complicated.

Because the electrons are so much smaller than the other particles, they have much longer mean free paths between collisions, and momentum is averaged out a little bit slower than for the heavy particles - the atoms and ions. For steady conditions, we quickly get *local thermodynamic equilibrium* (LTE). But if the temperature gradient is very steep, then hot (fast) electrons may get far into a colder zone before colliding and being slowed down, effectively giving a boundary zone with two temperatures; a high one for the electrons and a lower one for the heavy particles. This deviation from LTE is much more pronounced in near-vacuum systems, where there simply is less to collide with. However, in high-temperature electric arcs, the temperature gradients are very large in the arc fringes and close to the electrodes, so we must consider it here too.

The core of the matter is that *the plasma temperature* given by our energy equation is essentially the heavy particle temperature, but the electrical conductivity depends

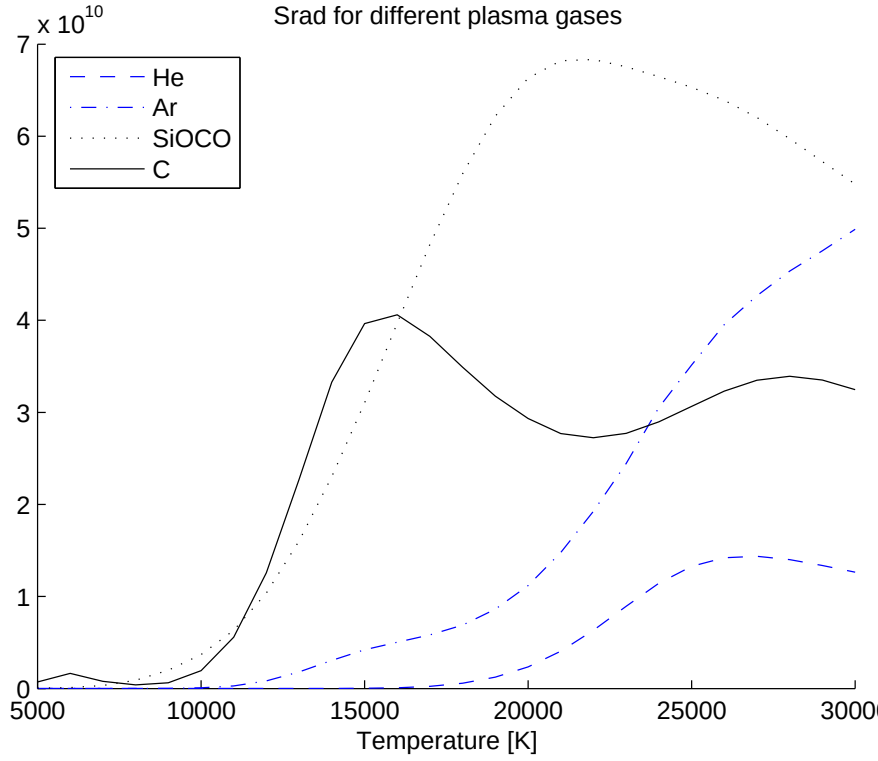

Figure 2.9: Emitted radiation densities [W/m^3] for different plasma gases.

mainly on the electron temperature. Thus, in the important non-equilibrium zones near the electrodes, electrical conductivity is in reality higher than in a equilibrium zone with the same temperature.

The practical implication is that the computed equilibrium plasma temperature near the cooled electrodes is too low, effectively acting as an insulating sheath. On the cathode, the boundary conditions impose a given arc current, resulting in too much heating just below the cathode spot. On the anode, the insulating sheath act as a barrier for low current densities and can lead to solutions where the current constricts near the anode to 'punch' through the barrier. Notice that since helium has much lower conductivity at temperatures near the walls, the non-LTE effects will be larger for helium than for argon.

There are also non-LTE zones in the outer area of the arc. These we do not consider very important, as the effect of these is to make the current distribution at the arc edge a little less steep. It is the authors belief that numerical effects contribute too

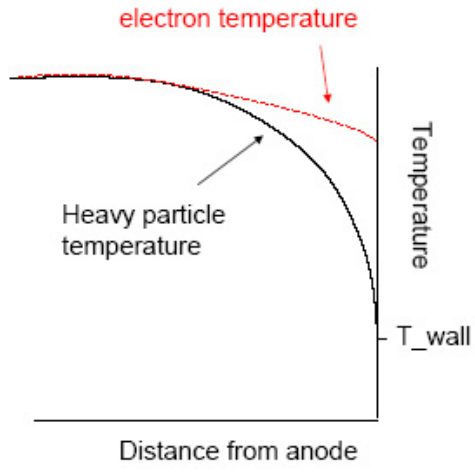

Figure 2.10: Illustration of heavy particle temperature and electron temperature in a non-LTE zone near a cooled anode

much to this anyway. Also, radiated heat depends on electron temperature, but since the radiation model used already gives a too high temperature in the outer zones, fixing this error may actually make the end result worse. If using a more advanced radiation model (such as the IMPC model), the conclusion may be reversed though, as a hotter arc fringe absorb more of the radiation from the arc core.

2.4.2 Numerical solutions

The paradox with the LTE problem is that the smaller cells we use, the larger the temperature gradient in the cell closest to the wall, and the larger the LTE problem becomes. For a cell larger than the temperature layer, most of the problem will mostly be averaged away. This suggests the crudest way of dealing with the non-LTE problem: simply have big cells. Naturally, a too coarse grid is not desirable for any simulation, but if a coarse grid is used we do not necessarily need to deal with the non-LTE boundary.

For 2D cases we can afford a fine grid as well as some extra iterations to deal with the non-LTE problem. The problem is that with our one-temperature model, we cannot know how the electron temperature behaves near the electrodes. From literature we can find some typical results[51], indicating that the non-LTE layer near the electrodes typically is a few mm thick, and that the degree of non-LTE increases nearer the wall. From this, we must try to construct an *artificial* electron temperature distribution in the layer.

2.5 Argon vs Helium

The modeling in this work is done on arcs in almost exclusively pure argon or helium atmospheres. In the real PPM reactor, argon was used for function testing and preheating, while helium is used for the actual production of nanotubes. The initial reason for choosing helium was to get a higher voltage and thus more power in the arc without needing an even bigger current supply. However, throughout the simulations, some fundamental differences in arc behaviour were discovered. Since argon is the most familiar plasma gas for many readers, many simulations were done first in Ar, and then in He for comparison.

2.5.1 Notable material differences

For all the calculated properties, helium stands out from the normal. The most important material difference for arc purposes is the higher ionization energy of He, giving a lower conductivity for temperatures up to about 25000 K. Due to the small particle cross section of He, viscosity is significantly lower than for Ar, and heat conduction is higher. For high temperatures, the difference in heat conduction is exaggerated while Ar viscosity drops. Molar heat capacity is similar due to both being monoatomic, so heat capacity is proportional to mass density for low temperatures. For high temperatures, He has a much higher specific enthalpy and heat capacity.

Finally, the radiation spectrum is different, with the He dominated by UV lines versus Ar having more in the visible spectrum. This leads to the differences in radiative heat transfer as computed above

2.5.2 Consequences of the material differences

Colour of the radiation

Everyone can see the difference between an arc burning in helium and one burning in argon: the helium arc glows with a violet light while the argon arc burns bright white, as shown on figure (2.21) at the end of the chapter. Actually, a helium arc typically emits a lot more radiation than an argon one, but mostly in the invisible UV part of the spectrum. Identifying the plasma gas from looking at modeling results requires a more trained eye, but there are some vital differences.

Velocity

The most obvious difference between the systems is the velocity. The Lorentz force acting on the charged particles depends only on the charge, so the acceleration is

an order of magnitude higher for the light helium atoms. Combined with the low viscosity, this gives significantly higher velocities everywhere in the reactor. Also, any transient phenomena tend to happen on a shorter timescale in He arcs.

Maximum temperature

The second difference is that of maximum temperature. Helium having the lower electrical conductivity gives more power and higher temperatures compared to argon arcs with similar currents. Defining the '*radiation equilibrium temperature*' as the temperature where radiation loss equals the resistive heating, we find that it is higher for a He-arc than for a Ar-arc with the same current density. Since the hottest part of the arc must also have a heat loss due to thermal conduction and convection, this radiation equilibrium temperature limits the maximum temperature in an arc. Typically, the hottest point is below the cathode spot, and the current density here will typically be of magnitude 10^7 A/m^2 regardless of plasma gas. Inserting the computed conductivities and radiative loss for a current density of 10^7 A/m^2, we get radiation equilibrium temperatures of about 19500 K for Ar vs 23500 K for He. Inserting a current density of 10^6 A/m^2, the equilibrium temperatures change to about 11000 K for Ar and 17000 K for He. Naturally, convective and conductive heat transport is also important in the arc plasma, but the 'radiation equilibrium temperature' gives a theoretical upper limit. Figures 2.11 and 2.12 shows computed temperature-current density equilibriums for different plasma gases and He-C systems, respectively.

Arc constriction at the anode

A third and very interesting difference between Ar and He is the behaviour near the cold anode. Even when taking into account the non-LTE problems in this zone, the He arc tends to constrict just before the anode, while the Ar arc tends to be more diffuse, as shown in figure 2.5.2 What happens is that hot gas jet of the arc hits the anode and is deflected outwards, giving a layer of 'medium temperature' along the anode surface. In this context 'medium temperature' means cooler than the plasma inside the arc itself, but hotter than the gas outside the arc. The reason for the difference in behaviour is that in this temperature range, Ar still conducts electricity while He does not. Thus, in Ar the current spreads out in the plume, while in He the current stays in the hot core of the arc which constricts as the whole arc gets colder near the anode. The effect of this is that in the He arc, the constriction gives a braking Lorentz force (a small anode jet) that tries to kick the plume away from the anode. The Ar arc by comparison has an accelerating Lorentz force for the whole arc length that keeps the plume stuck to the anode wall.

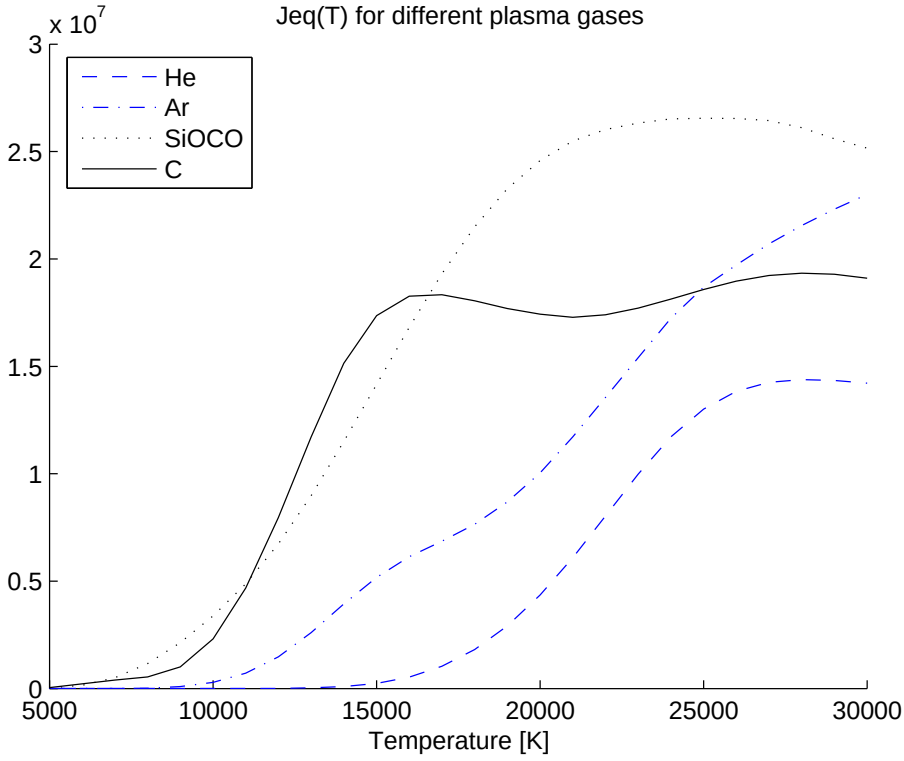

Figure 2.11: Temperature/ current density equilibrium for different plasma gases.

Temperature profile and Peclét number

The forth point worth mentioning is the thing that does *not* make a difference! One might assume that with velocities an order of magnitude apart, the convective heat transport and thus the temperature profile should be distinctly different. Similarly, the difference in heat conductivity should be visible on the temperature plots. This is not the case. The parameter that governs the shape of the temperature profile is the *Peclét number*, Pe, which is the ratio of convective to conductive heat transport. The definition of Pe is

$$Pe = RePr = l_0 v_0 \rho \hat{C}_p / k \tag{2.7}$$

The characteristic length scale is the width of the arc, which is nearly identical for He and Ar. The characteristic velocity is the maximum velocity, which depends on the current as well as other parameters. Roughly, the maximum velocity in helium is about a factor 10 higher than in Ar. The rest of the parameters in the Peclét formula are given in our list of transport coefficients. A plot of $Pe/l_0 v_0$ for He and Ar gives a ratio varying between 0.05 and 0.2, assuming the ratio of $l_0 v_0(He)/l_0 v_0(Ar)$ to be

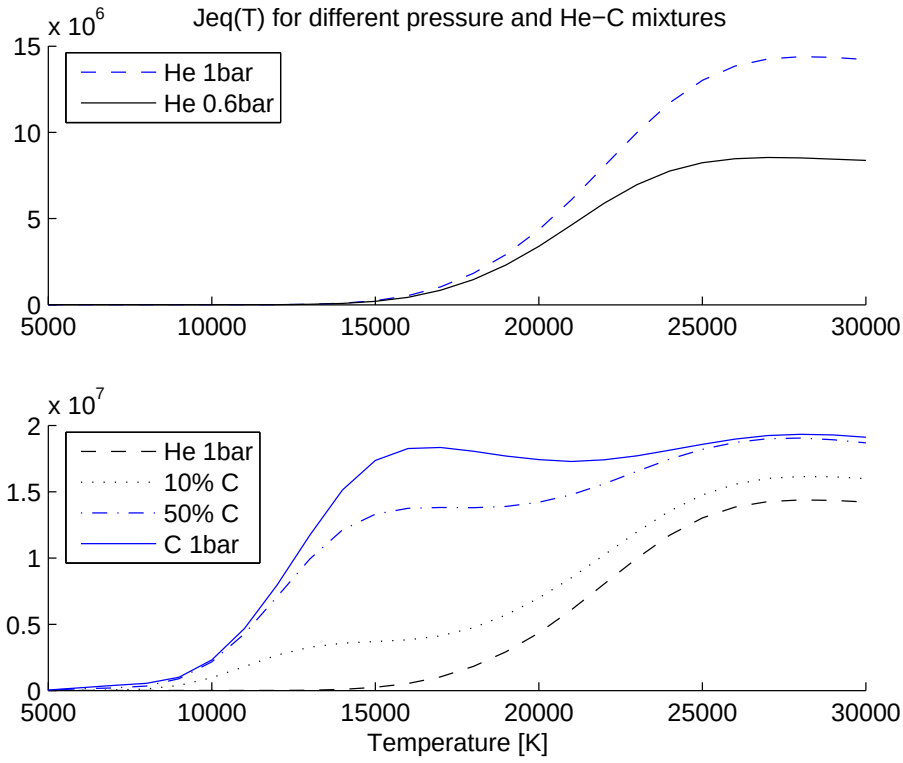

Figure 2.12: Temperature/ current density equilibrium for different pressures and He-C mixtures

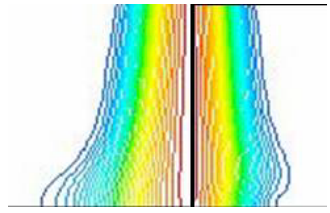

Figure 2.13: Typical current behaviour near a cold anode. Left: argon (expands near the anode), right: helium (constricts near the anode)

near 10, this gives a ratio in Peclét numbers of $0.5-2$, telling us that the temperature profiles indeed must be expected to resemble each other.

2.6 He-C mixtures

Most of the simulations and tests in this work have been done with pure Ar or pure He as plasma gas. However, in the real reactor there is a significant amount of carbon vapor -the building material for the nanotubes. The simplest way to start investigating this is by assuming given homogenous concentrations of carbon in the helium, and comparing these results to the pure He cases. The reality is of course that carbon will evaporate and recondensate at different places, and that the carbon concentration will be nonuniform[2]. But the assumption of a homogeneous concentration is "for free" in the sense that once we have calculated the material properties for the mixed plasma gas, the models need no further modifications.

We have no way of measuring the actual carbon concentration in our experiments. Near the electrode surfaces it may be very high. In the top of the arc, above the injection lances, it may be very low. In order to get a rough overview, transport properties were computed for 'low' (1:10), 'high' (1:1) and 'extremely high' (1:0) carbon-helium ratios.

The reactor in the PPM project operates at 0.6 bar, and most cases with helium are simulated for 0.6 bar. However, an investigation of how reactor pressure affects the plasma properties is appropriate. Thermodynamic and transport data were therefore computed for pure He systems at pressures of 1 bar, 0.6 bar and 0.3 bar for comparison, as shown in the various figures in this chapter.

2.6.1 Computed properties for He-C mixtures and He at different pressures

See figures (2.14 - 2.20) for computed properties.

2.6.2 Effects of carbon vapor

Obviously, pure carbon vapour is a very different plasma gas from pure helium. Mixtures end up somewhere between their 'parent gases' as there are no reactions between He and C.

The first striking result for the mixtures is in the electrical conductivity. Figure (2.15) shows that *even a small amount of carbon vapor is enough to dramatically increase the conductivity at low temperatures.* This perhaps removes one of the advantages of using He in the first place: the high voltage at a given current. When

[2] A more rigorous approach would be to solve the *mass transport (diffusion) equations* for carbon in helium, and use the calculated equilibrium vapor pressures as our boundary conditions (along with mass transfer coefficients for surfaces with evaporation or condensation).

injecting carbon, the arc may be wider and current density and thus temperature decreases. Also, the risk of the arc short-circuiting becomes much higher if there is carbon vapor near surfaces.

The second vital difference is in the emitted radiation shown in figure (2.20), which is much higher for carbon than for helium. The effect of this is that in mixtures with high carbon concentrations the arc will generally be much colder as we move away from the cathode. Computed 'radiation equilibrium temperatures' for a current density of 10^7 A/m^2 are 23500 K, 22000 K, 13000 K and 12500 K in order of increasing amount of carbon. For 10^6 A/m^2 the values are 17000 K, 10000 K, 9000 K and 9000 K, respectively. The large influence of carbon vapor is evident when we compare for a current density of 10^5 A/m^2 and get the values 14000 K, 8000 K, 5500 K and 5500 K. By cross-checking with the electric conductivity tables, we see that in the 50-50 and pure carbon mixtures, the conductivity at this temperature is so low that the arc may be close to extinction.

Carbon vapor has a generally much higher density and lower viscosity. Carbon enthalpy is higher in the interesting temperature area (below about 20000 K), and the electrical conductivity is higher for carbon at all relevant temperatures, but especially so at low temperatures where helium is practically non-conductive. Finally, the heat conductivity is higher for carbon at temperatures up to about 12000 K, while helium conducts heat much better at high temperatures. From this we would expect an arc in carbon vapor to be much more diffuse than a helium arc, as conductivity is higher while lower velocities and higher heat conduction combine to give a much lower Péclet number. In reality, the high radiation loss dominates the heat transport, and the arc actually gets thinner.

2.6.3 Effects of different pressure

The most obvious effect of lowering the pressure is that the density decreases. Apart from this, changes in thermodynamic and transport properties are negligible. However, when computing radiation data, pressure makes a significant difference. The temperature dependence of the emitted radiation is similar, but the total radiation loss is much smaller for the less dense plasma gases: computed losses for pure He at 1 bar were a factor 1.5-2 higher than at 0.6 bar.

The effect of this is that an arc at lower pressure will have less radiation loss, meaning less total power. On the other hand, a low pressure arc will have a higher maximum temperature if the current density is similar; computing "radiation equilibrium temperatures" for a current density of 10^6 A/m^2 gives about 17500 K for 0.6 bar vs 17000 K for 1 bar. For a current density of 10^7 A/m^2, we get about 23000 K for 1 bar,

while the radiation from the 0.6 bar arc is not sufficient in itself to counterbalance the resistive heating!

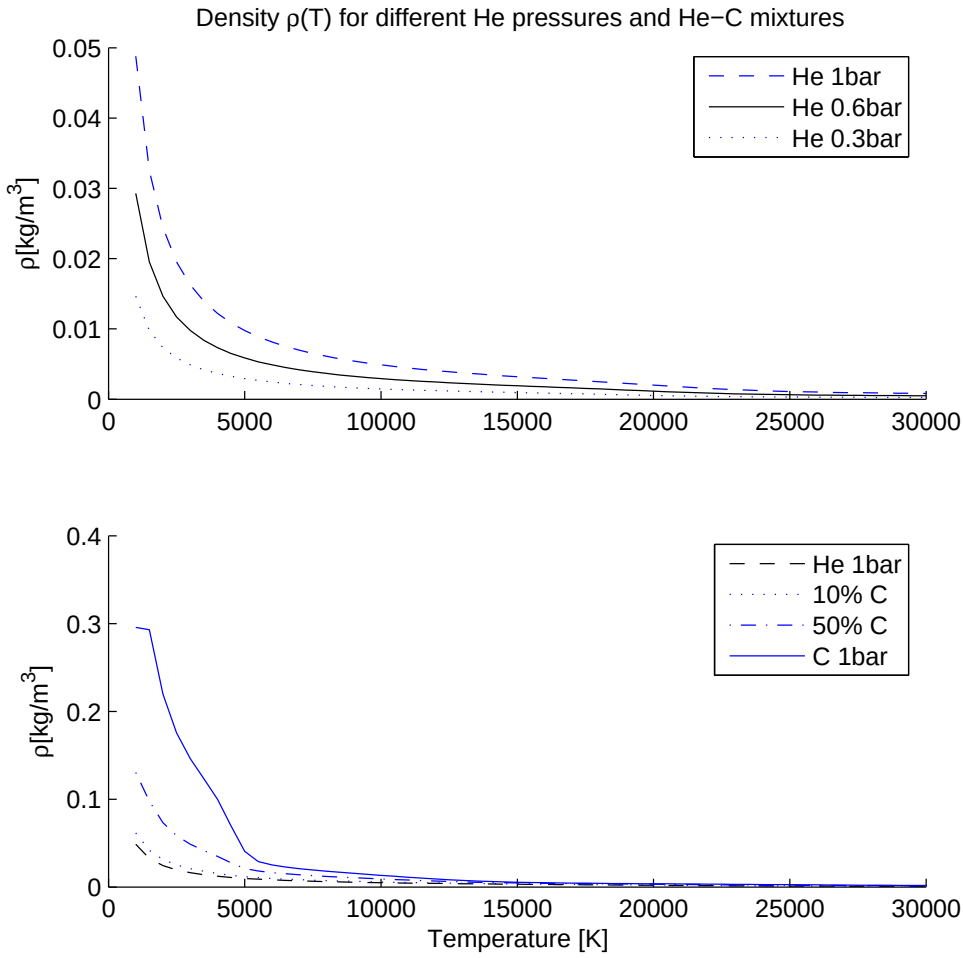

Figure 2.14: Density [kg/m^3] as function of temperature for different pressures and He-C mixtures

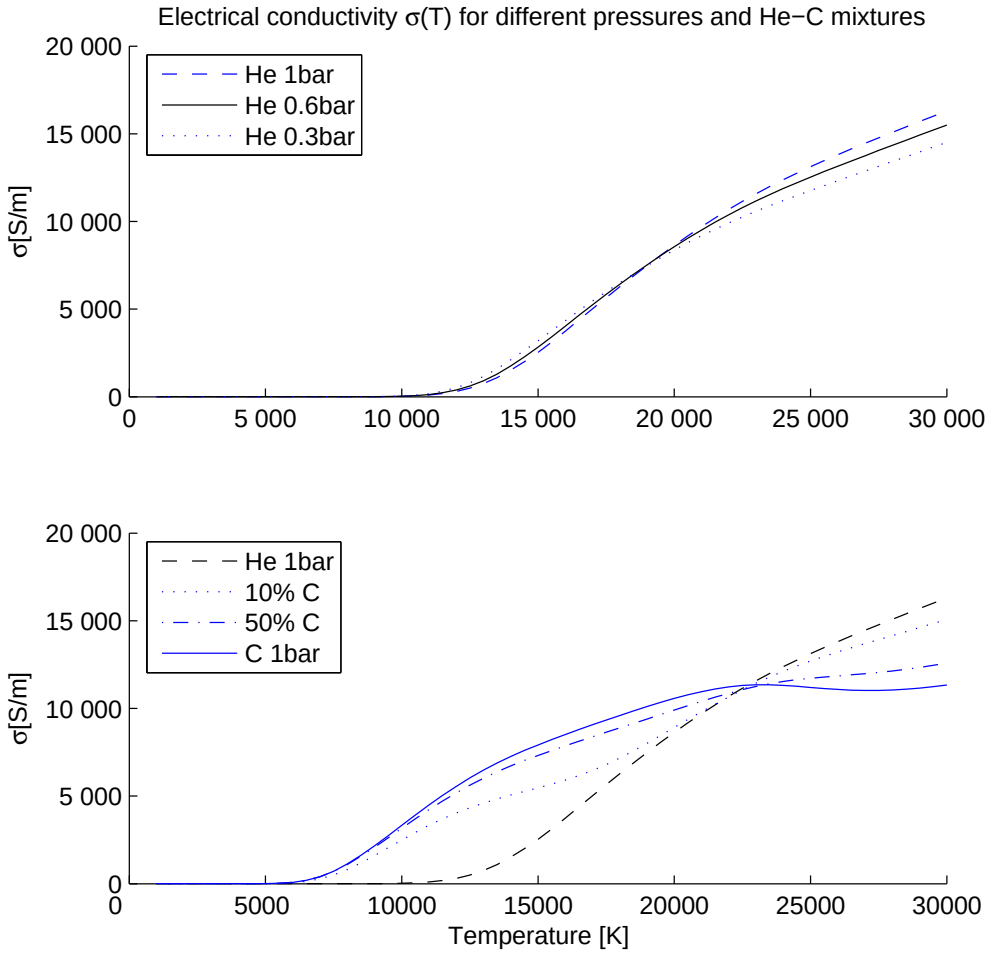

Figure 2.15: Electrical conductivity [S/m] as function of temperature for different pressures and He-C mixtures

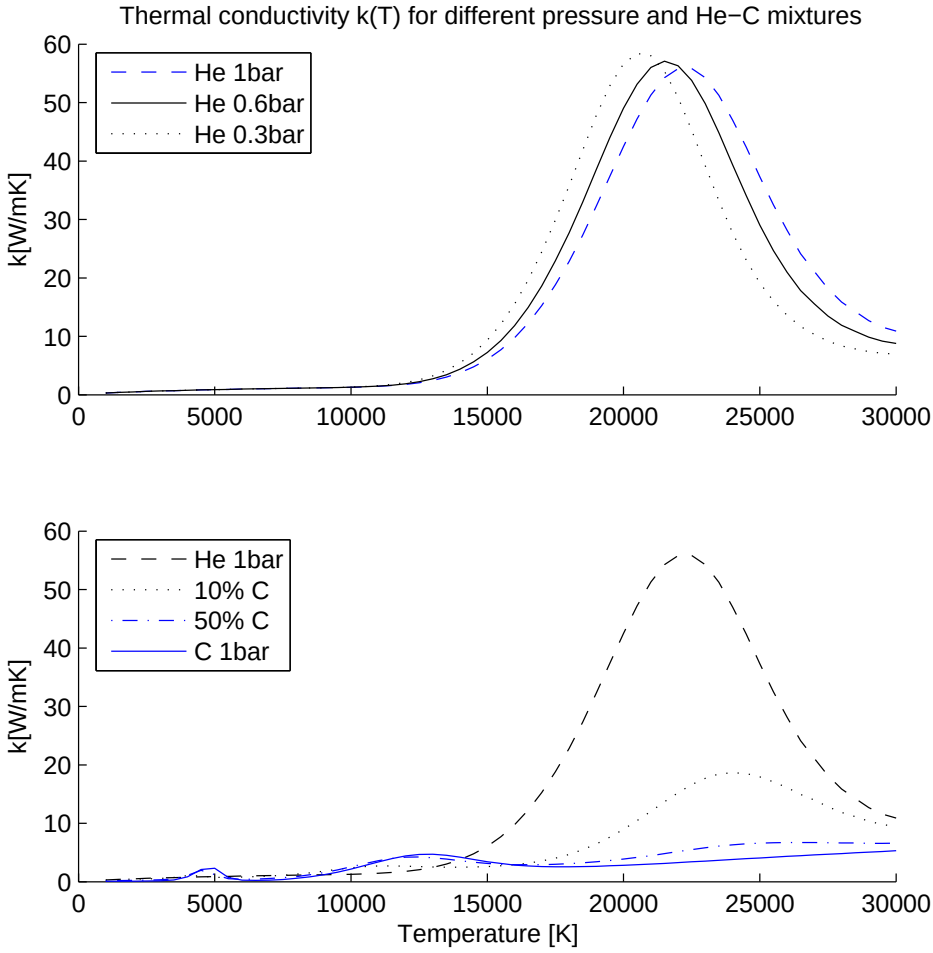

Figure 2.16: Thermal conductivity [W/m K] as function of temperature for different pressures and He-C mixtures

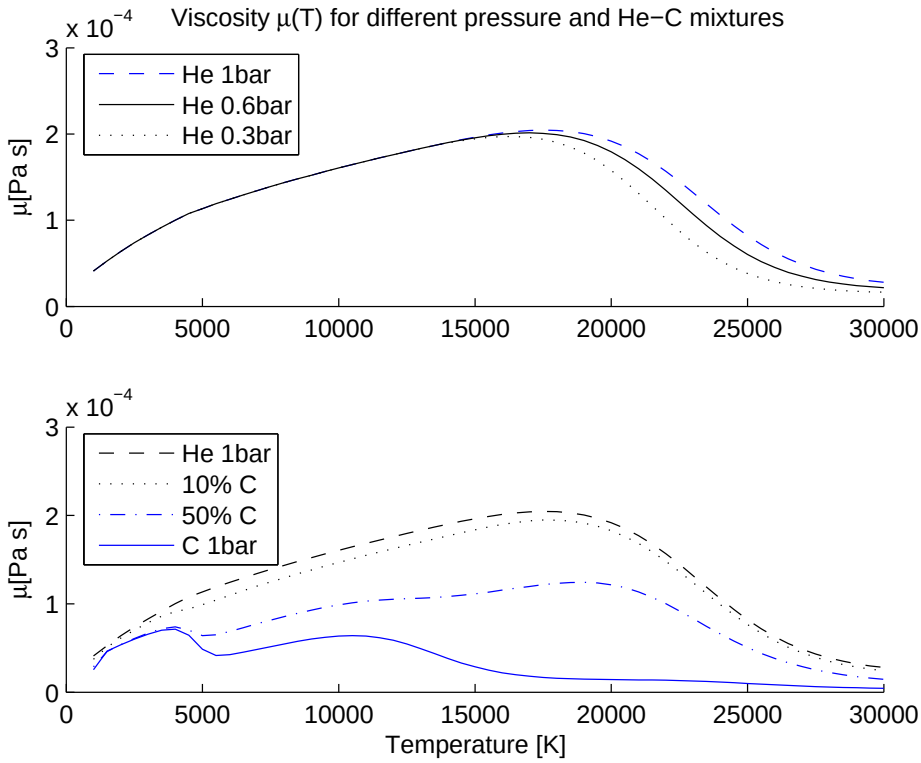

Figure 2.17: Viscosity [Pa s] as function of temperature for different pressures and He-C mixtures

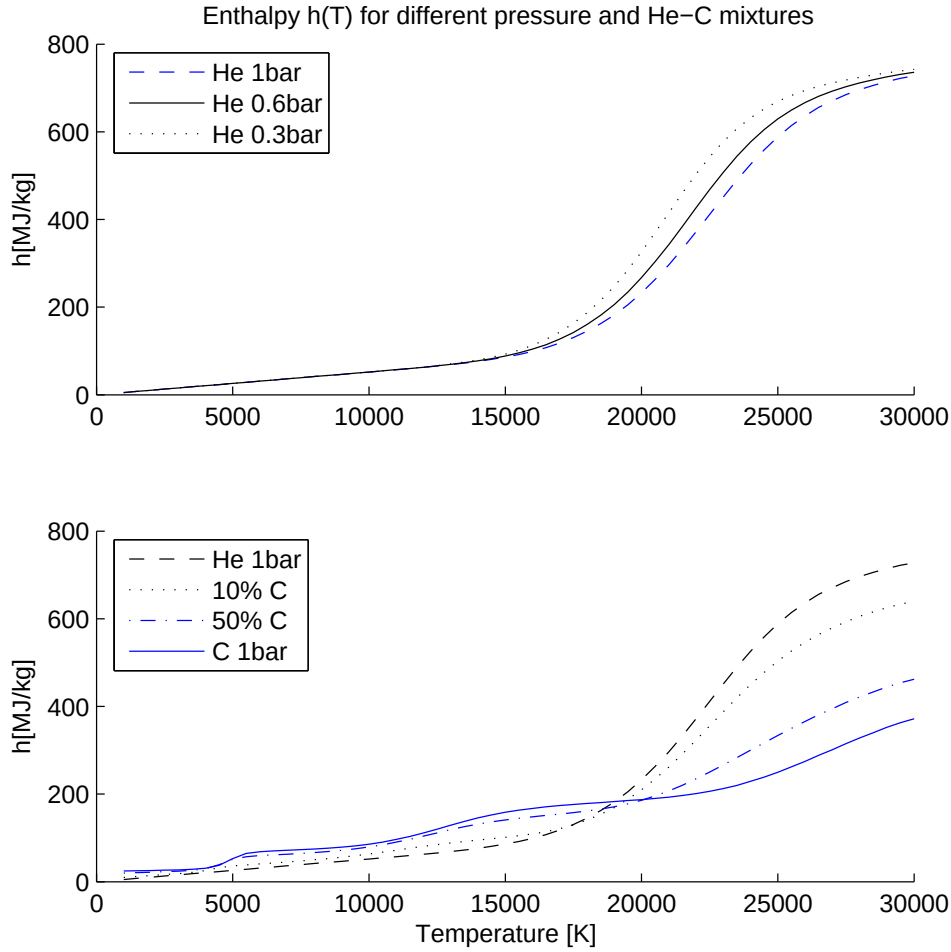

Figure 2.18: Specific enthalpy [J/kg] as function of temperature for different pressures and He-C mixtures

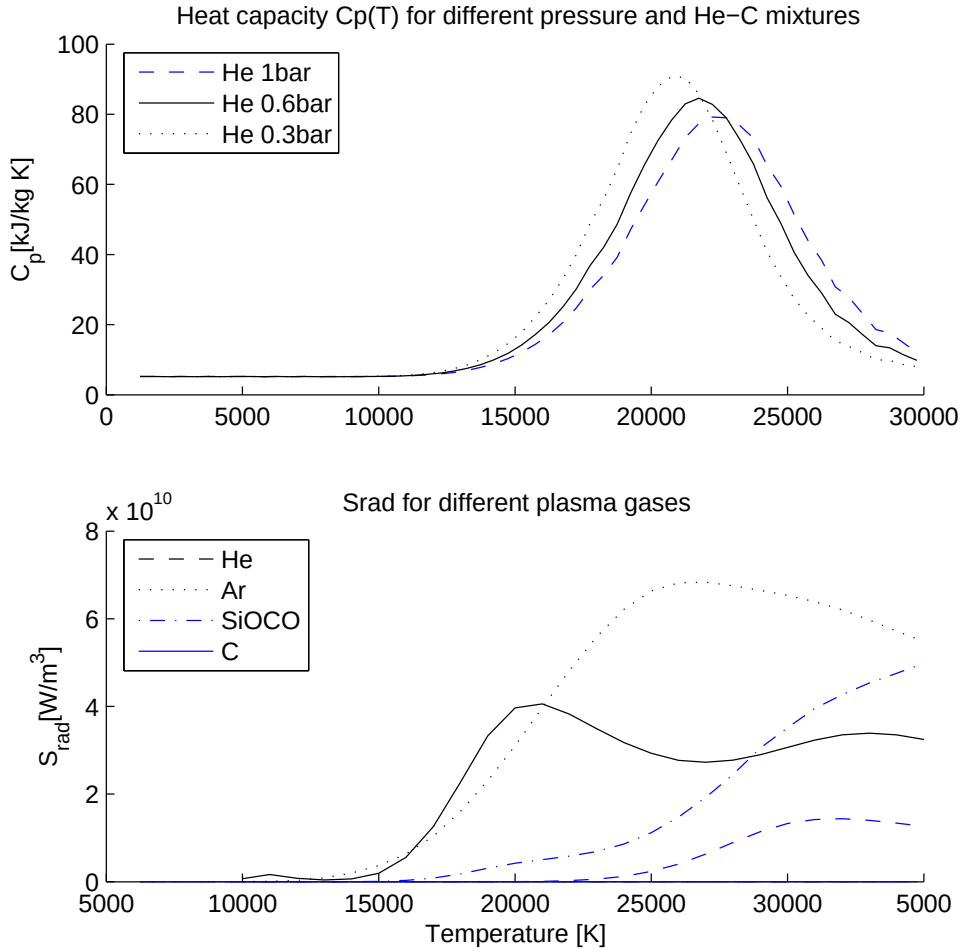

Figure 2.19: Specific heat capacity [J/kg K] as function of temperature for different pressures and He-C mixtures

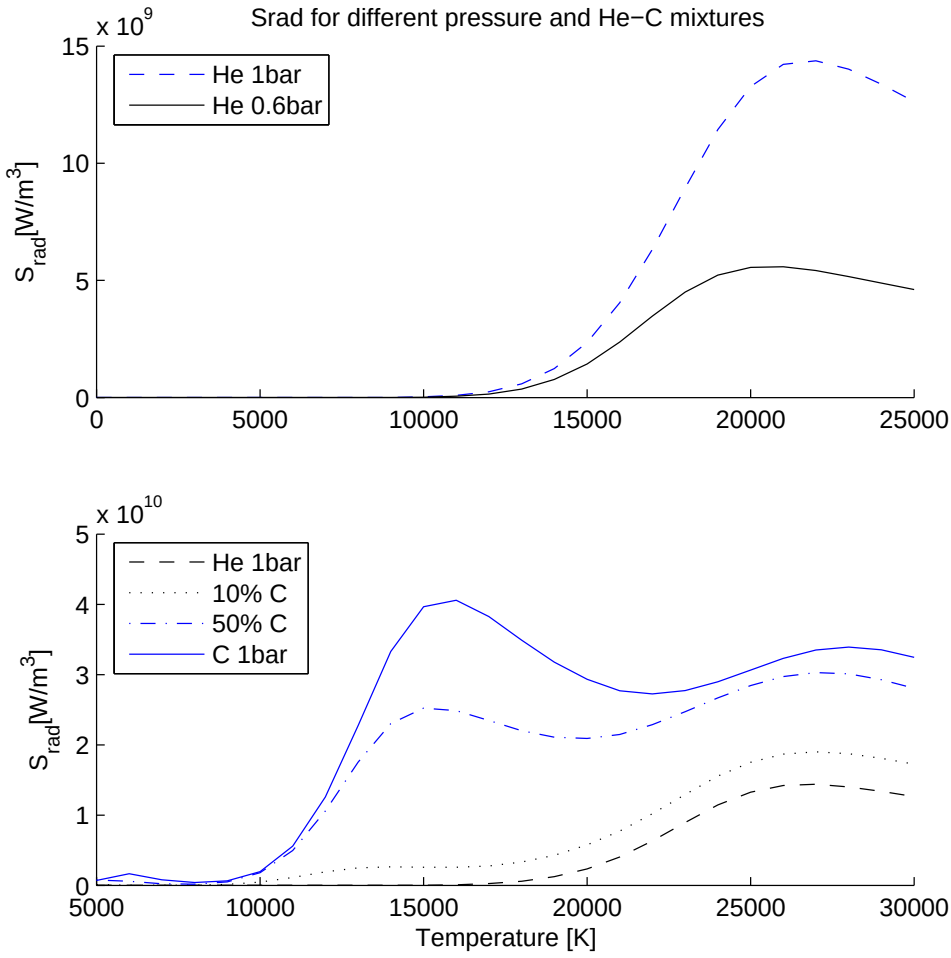

Figure 2.20: Emitted radiation densities [W/m^3] as function of temperature for different pressures and He-C mixtures. The effective radiation radius (Lowke's method) is $R_{eff} = 0.89$ cm. See appendix B for the effect of different R_{eff}.

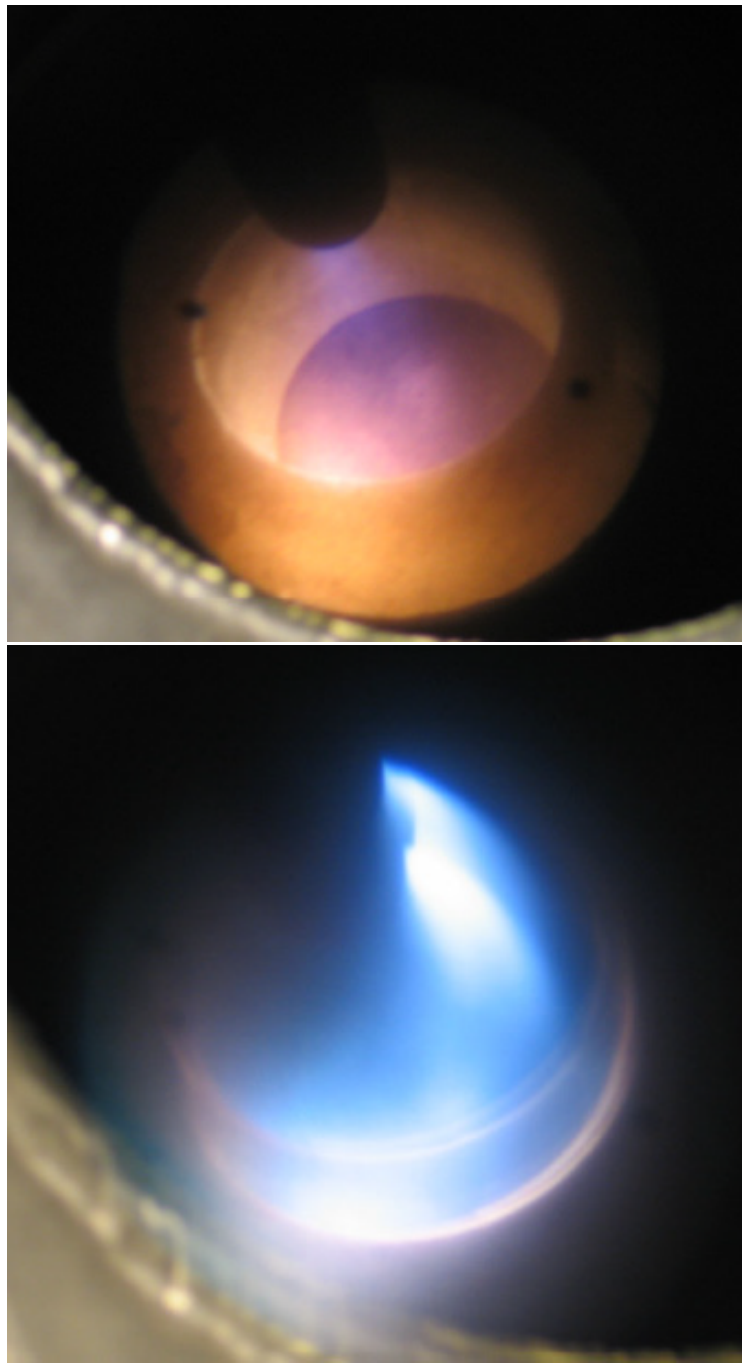

Figure 2.21: He arcs burn with a violet light, while Ar gives white light.

Chapter 3

The Magneto-Fluid Dynamic B-equation (MFD-B) model

3.1 Introduction and background

The MFD B field model was developed and implemented in Fluent 2.97 by Dr. Hilde Løken Larsen [40], and has proved very useful for simulations of high-current axisymmetric AC arcs. The axisymmetric MFD model had the advantages of having only one electromagnetic transport equation, with boundary conditions that are exact and easy to find. The other transport equations (1.4, **??**) get source terms as described in section 1.7.

In this work, we want to generalize the MFD-B model to 3D arcs and assess its ability and efficiency for solving different classes of problems. Also, the 2D model must also be reformulated to fit the Fluent UDF interface.

3.2 The $\vec{B}$-transport equation

3.2.1 Derivation from Maxwell's equations

Since the arc is an electromagnetic phenomenon, Maxwell's equations must apply:

$$\nabla \cdot \vec{D} = \rho_e \tag{3.1}$$

$$\nabla \cdot \vec{B} = 0 \tag{3.2}$$

$$\nabla \times \vec{E} = -\frac{\partial}{\partial t}\vec{B} \tag{3.3}$$

$$\nabla \times \vec{B} = \mu_0(\vec{j} + \frac{\partial}{\partial t}\vec{D}) \tag{3.4}$$

in addition, we need the constitutional relation

$$\vec{D} = \epsilon_0 \vec{E} \tag{3.5}$$

and the generalized Ohm's law:

$$\vec{j} = \sigma(\vec{E} + \vec{v} \times \vec{B}) + \frac{\vec{j} \times \vec{B}}{en_e} + \frac{\nabla p_e}{en_e}$$

where the second and third terms are due to Hall effect and electron diffusion, respectively.

The arc plasma is electrically neutral with $\rho_e = 0$ except in the extremely thin space charge zones around the cathode and anode. In Maxwell's equations, the displacement current $\frac{\partial \vec{D}}{\partial t}$ can be safely neglected in low-frequency AC arcs and slow moving (magnetically rotated or unstable) DC arcs. Also, for all cases we investigate with the MFD-B model, the Hall effect and electron diffusion terms are negligible[1], reducing the Ohm's law to just

$$\vec{j} = \sigma(\vec{E} + \vec{v} \times \vec{B}) \tag{3.6}$$

The assumption of negligible electron diffusion is safe to make in the bulk of the arc, but if we want to investigate behaviour very close to the cathode or anode this should be included (along with non-LTE effects). From equations (3.1-3.4) we obtain a transport equation for the magnetic induction $\vec{B}$:

$$\frac{\partial}{\partial t}\vec{B} + \nabla \times \left[\Gamma_m(\nabla \times \vec{B})\right] = \nabla \times (\vec{v} \times \vec{B}) \tag{3.7}$$

where $\Gamma_m = 1/\mu_0\sigma$ is the *magnetic diffusivity*.

This equation will be referred to as the *MFD-B equation* or B transport equation.

3.2.2 Fluent UDS compatibility

Since we do not have the opportunity to make changes in the Fluent source code, the MHD-B equation must be formulated so as to fit to the form of a general transport equation. The Fluent UDS-solver assumes the equations to be on the general form

$$\frac{\partial}{\partial t}(A\phi_i) + \nabla \cdot (\vec{j}\phi_i - \Gamma_i \nabla \phi_i) = S_i$$

[1] this was discussed in [40].

where A and $\vec{j}$ are user-defined "flux functions" for unsteady and convective flux, and S is a source term.

By letting $A = 1, \vec{j} = \vec{v}, \Gamma = \Gamma_m$ and $\phi = B_x$, we get

$$\frac{\partial}{\partial t}(B_x) + \nabla \cdot (\vec{v}B_x - \Gamma_m \nabla B_x) = S_x \tag{3.8}$$

Now the point is to find S on the most computationally efficient form.

Expanding this UDS equation, we get

$$\underbrace{\frac{\partial}{\partial t}(B_x)}_{(0)} + \underbrace{(\vec{v} \cdot \nabla)B_x}_{(1)} + \underbrace{(\nabla \cdot \vec{v})B_x}_{(2)} - \underbrace{\Gamma_m \nabla^2 B_x}_{(3)} - \underbrace{\nabla B_x \cdot \nabla \Gamma_m}_{(4)} = S_x \tag{3.9}$$

Similarly expanding the MFD-B equation, we get

$$\underbrace{\frac{\partial}{\partial t}\vec{B}}_{(0)} + \underbrace{(\vec{v} \cdot \nabla)\vec{B}}_{(1)} + \underbrace{(\nabla \cdot \vec{v})\vec{B}}_{(2)} - \underbrace{\Gamma_m \nabla^2 \vec{B}}_{(3)} - (\nabla \times \vec{B}) \times \nabla \Gamma_m = (\vec{B} \cdot \nabla)\vec{v} \tag{3.10}$$

If we consider the x-component of the MFD-B equation, we see that the terms (1), (2), (3) are the same. We must then have

$$\begin{aligned}\Big[(\nabla \times \vec{B}) \times \nabla \Gamma_m\Big]_x &= (\nabla \times \vec{B})_y \frac{\partial \Gamma_m}{\partial z} - (\nabla \times \vec{B})_z \frac{\partial \Gamma_m}{\partial y} \\ &= (\tfrac{\partial B_x}{\partial z} - \tfrac{\partial B_z}{\partial x})\tfrac{\partial \Gamma_m}{\partial z} + (\tfrac{\partial B_x}{\partial y} - \tfrac{\partial B_y}{\partial x})\tfrac{\partial \Gamma_m}{\partial y} + (\tfrac{\partial B_x}{\partial x} - \tfrac{\partial B_x}{\partial x})\tfrac{\partial \Gamma_m}{\partial x}\end{aligned}$$

where the last term is just a zero in disguise. Recombining, we get

$$\Big[(\nabla \times \vec{B}) \times \nabla \Gamma_m\Big]_x = \underbrace{\nabla B_x \cdot \nabla \Gamma_m}_{(4)} - \frac{\partial}{\partial x}\vec{B} \cdot \nabla \Gamma_m \tag{3.11}$$

we now have (4) accounted for, and S must then be whatever is left. The B_x equation now looks like:

$$(0) + (1) + (2) + (3) + (4) = (\vec{B} \cdot \nabla)v_x - \frac{\partial}{\partial x}\vec{B} \cdot \nabla \Gamma_m$$

in other words:

$$S_x = (\vec{B} \cdot \nabla)v_x - \frac{\partial}{\partial x}\vec{B} \cdot \nabla \Gamma_m \tag{3.12}$$

and similar for S_y, S_z

The source term for each $\vec{B}$ component depends then on the other components, and the three component MFD-B equations are coupled.

Note that we assume neither incompressibility nor a constant diffusivity. There is a commercially available 'MHD package' [23] for Fluent 6, but it uses equations that assume constant Γ_m and is therefore not useful for arc discharges.

3.2.3 2D axisymmetric equation

For axisymmetric cases, there is only one $\vec{B}$ component, and the MFD-B equation becomes relatively friendly:

$$\frac{\partial B_\theta}{\partial t} + \frac{\partial}{\partial r}(v_r B\theta) + \frac{\partial}{\partial z}(v_z B_\theta) = \frac{\partial}{\partial r}\left(\frac{\Gamma_m}{r}\frac{\partial}{\partial r}(rB_\theta)\right) + \frac{\partial}{\partial z}\left(\Gamma_m \frac{\partial B_\theta}{\partial z}\right) \tag{3.13}$$

Similarly, the Fluent UDS equation gets its axisymmetric form. Doing calculations similar to above, it is relatively easy to show that

$$S_\theta = (\frac{\partial \Gamma_m}{\partial r} - \frac{\Gamma_m}{r})\frac{B_\theta}{r} + \frac{v_r}{r}B_\theta \tag{3.14}$$

3.2.4 Application of B_θ to the flow equations

The effect of the arc on the flow is modeled through source terms in the normal flow equations.

Momentum equations contain a source term for the Lorentz force contribution $\vec{j}\times\vec{B}$. In 2D axisymmetry this means

$$F_r = -j_z B_\theta \tag{3.15}$$

$$F_z = j_r B_\theta \tag{3.16}$$

Energy equation: in addition to resistive heating ($Q_{res} = j^2/\sigma$), we must also implement a radiation model. Additionally, there will be heat transport due to the conduction electrons. The total energy source term must be

$$S_{energy} = \frac{j_r^2 + j_z^2}{\sigma} + \frac{5k_B}{2e}\left(j_r\frac{\partial T}{\partial r} + j_z\frac{\partial T}{\partial z}\right) + S_{rad} \tag{3.17}$$

where in all these equations

$$j_z = \frac{1}{\mu_0}\frac{1}{r}\frac{\partial(rB_\theta)}{\partial r} \tag{3.18}$$

$$j_r = -\frac{1}{\mu_0}\frac{\partial B_\theta}{\partial z} \tag{3.19}$$

3.2.5 Low magnetic Reynolds number

When considering the $\vec{B}$ transport equation as analog to heat and momentum transport equations, we get an analog for the Reynolds' number. This *magnetic Reynolds' number,* Re_m, is the ratio of convective vs. conductive transport of B and is given by

$$Re_m = vl/\Gamma_m = vl\mu_0\sigma \tag{3.20}$$

where v and l are characteristic velocity and length scale for the arc system; the obvious choices are $v_{z,max}$ and cathode spot radius R_c.

For a typical lab scale arc $\sigma \approx 10^3$ S/m, $l \approx 10^{-2}$ m and $v_{z,max} < 10^3$ m/s
giving $Re_m \approx 0.01$

The effect of low Re_m is that we have very little current $\sigma(\vec{v} \times \vec{B})$ induced by flow across magnetic field lines. We can then assume Ohm's law to be on the simplest form

$$\vec{j} = \sigma\vec{E} \tag{3.21}$$

All velocity-terms disappear from the MHD equation, and the source term becomes

$$S_\theta = (\frac{\partial\Gamma_m}{\partial r} - \frac{\Gamma_m}{r})\frac{B_\theta}{r} \tag{3.22}$$

or, in the general case

$$S_x = -\frac{\partial}{\partial x}\vec{B} \cdot \nabla\Gamma_m \tag{3.23}$$

3.2.6 Computational issues

There is one problem with the MFD-B equation yet: the source term contains a gamma gradient. This is unfortunate for two reasons:

Primarily, because gamma is an extremely steep[2] function of temperature and the temperature gradient is extremely steep, the gradient will be very large. If the cell

[2]electrical conductivity of 1 bar He increases by four orders of magnitude from 6000 K to 10000 K, which is typically only a few mm.

resolution is not fine enough, this will give rounding errors.

Secondly, to make it worse, conductivity must be implemented as a piecewise linear function. The temperature dependency of gamma (which is inverse conductivity) will therefore also contain rounding errors.

The core of the matter is that the source term is proportional to $(\frac{\partial \Gamma_m}{\partial r} - \frac{\Gamma_m}{r})$ and both parts have rounding errors. Because of the minus sign, this can give a huge relative error on the total. In the interior of the arc, the gamma is much larger than the gradient and the total relative error of the source term is similar to the relative error of the gamma. But in the outer area of the arc, the gradient is of same order of magnitude as the gamma, and the error of the computed magnetic field may be substantial.

Earlier works with the MFD-B model

In the works of H.L.Larsen[40] and G.A.Sævarsdottir[51], the code was implemented directly into the Fluent 2.97 source code. Therefore it was possible to discretize the equations differently to avoid this problem.

3.3 The axisymmetric MFD-β equations

3.3.1 β field equation

In order to get a source term that is more suited for the Fluent 6 solver, we can scale the variables in the MFD-B equation. The source of our trouble is the term

$$\frac{\partial}{\partial r}\left(\frac{\Gamma_m}{r}\frac{\partial}{\partial r}(rB_\theta)\right) \tag{3.24}$$

but this term can be simplified by *solving the equation with respect to*

$$\beta = rB_\theta \tag{3.25}$$

This variable change is also very practical when considering the magnet field outside the arc (which is why it was investigated), as instead of $B_\theta = C/r$ we get $\beta = C$ which should give no 'ghost currents' due to rounding errors in the magnetic field.

Reformulating the axisymmetric MFD-B equation (3.13), we get

$$\frac{1}{r}\frac{\partial}{\partial t}(\beta) + \frac{\partial}{\partial r}\left(\frac{1}{r}v_r\beta\right) + \frac{1}{r}\frac{\partial}{\partial z}\left(v_z\beta\right) = \frac{\partial}{\partial r}\left[\frac{1}{r}\Gamma_m\frac{\partial}{\partial r}(\beta)\right] + \frac{1}{r}\frac{\partial}{\partial z}\left[\Gamma_m\frac{\partial}{\partial z}\beta\right]$$

$$\Leftrightarrow \frac{\partial \beta}{\partial t} + \frac{\partial}{\partial r}\left(v_r\beta\right) + \frac{\partial}{\partial z}\left(v_z\beta\right) = \frac{\partial}{\partial r}\left[\Gamma_m\frac{\partial \beta}{\partial r}\right] + \frac{\partial}{\partial z}\left[\Gamma_m\frac{\partial \beta}{\partial z}\right] + \frac{v_r\phi}{r} - \frac{\Gamma_m}{r}\frac{\partial \beta}{\partial r}$$

$$\Leftrightarrow \frac{\partial \beta}{\partial t} + \frac{\partial}{\partial r}\left[v_r\beta - \Gamma_m \frac{\partial \beta}{\partial r}\right] + \frac{\partial}{\partial z}\left[v_z\beta - \Gamma_m \frac{\partial \beta}{\partial z}\right] = \frac{v_r\beta}{r} - \frac{\Gamma_m}{r}\frac{\partial \beta}{\partial r} \tag{3.26}$$

Which is the axisymmetric Fluent UDS equation for β with the source term

$$S = \frac{2}{r}\left[v_r\beta - \Gamma_m \frac{\partial \beta}{\partial r})\right] \tag{3.27}$$

The great news here is that the source term does not have a gamma gradient any more. Also, the behaviour of the solution near all edges should be simpler, and all gradients be much smaller. Basically, we get a better solution in shorter time with less effort!

Unfortunately, it only works in axisymmetric cases.

3.3.2 Application of β to the flow equations

All variables derived from B_θ must now be derived from β:

$$j_z = \frac{1}{\mu_0}\frac{1}{r}\frac{\partial \beta}{\partial r} \tag{3.28}$$

$$j_r = -\frac{1}{\mu_0}\frac{1}{r}\frac{\partial \beta}{\partial z} \tag{3.29}$$

$$F_z = \frac{1}{r} j_r \beta = -\frac{1}{2\mu_0}\frac{1}{r^2}\frac{\partial \beta^2}{\partial z} \tag{3.30}$$

$$F_r = -\frac{1}{r} j_z \beta = -\frac{1}{2\mu_0}\frac{1}{r^2}\frac{\partial \beta^2}{\partial r} \tag{3.31}$$

$$\frac{j_z^2}{\sigma} = \frac{1}{\mu_0}\Gamma_m \left[\frac{1}{r}\frac{\partial \beta}{\partial r}\right]^2 \tag{3.32}$$

$$\frac{j_r^2}{\sigma} = \frac{1}{\mu_0}\Gamma_m \left[\frac{1}{r}\frac{\partial \beta}{\partial z}\right]^2 \tag{3.33}$$

The β formulation indeed seems more natural than computing B_θ!

3.3.3 The physical interpretation of β

Indeed the β variable substitution was motivated by purely mathematical reasons, but the variable β also has a physical interpretation:

Consider that we want to see where the current goes in our arc. Not just current densities, but the fraction of total current flowing inside a certain radius. This is obtained by integration of j_z

$$\frac{I(r)}{I_{tot}} = \frac{1}{I_{tot}} \int j_z(r) 2\pi r Dr = \frac{2\pi}{\mu_0} \frac{\beta r}{I_{tot}} = \frac{\beta(r)}{\beta_\infty} \tag{3.34}$$

where β_∞ is the constant value of β outside the current carrying arc.

This implies that equal β value means equal fraction of the total current running inside. Tightly packed β-lines means high current density, spreading β-lines means the arc gets more diffuse. Closed β-lines means there is a closed circuit inside the system (due to either induction or error). The conclusion must be that β is a very 'real' physical parameter.

3.4 Boundary conditions for axisymmetric cases

3.4.1 Boundary conditions for $\vec{B}$ and β

Boundary conditions for temperature and flow are trivial in the sense that they depend only on the case and are not influenced by our choice of model. However, we need boundary conditions for the user-defined equations, i.e. the MFD equation.

The boundary condition we want to apply are for the current. Namely: given current distribution in the cathode spot, no current through the walls or the cathode surface outside the spot, and no tangential currents on the anode since the anode is a much better conductor than the plasma. See figure 3.4.1 for a simple illustration.

For the "pure $\vec{B}$ equation" this corresponds to a given B_θ profile on the cathode, a given B_θ value on the walls, and a zero normal derivative on the anode where $j_r = 0$. The B_θ profile is obtained from the current profile by

$$B_\theta(r) = \frac{\mu_0}{r} \int_0^r j_z r Dr \tag{3.35}$$

Outside the cathode spot and outside the arc including the outer walls, this is simply

$$B_\theta = \frac{\mu_0 I_{tot}}{2\pi r} \tag{3.36}$$

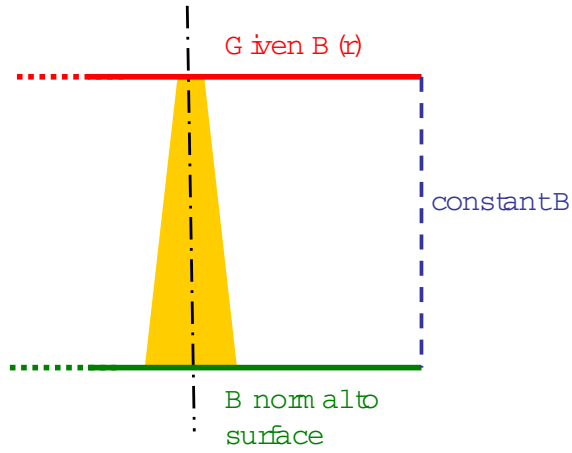

Figure 3.1: Illustration of a simple arc with boundary conditions. Cathode at the top, anode at the bottom.

Inside the cathode spot, the B_θ profile becomes linear for a homogenous current density, and 'S-shaped' for a parabolic current density distribution.

For the "β-equation", the boundaries are analog: given values at walls and cathode, zero normal derivative on the anode. The β profile is given from the assumed current distribution

$$\beta(r) = \mu_0 \int_0^r j_z r Dr \tag{3.37}$$

or, outside the arc:

$$\beta = \frac{\mu_0 I_{tot}}{2\pi} \tag{3.38}$$

Inside the cathode spot, i.e. $r < R_c$, a homogenous current distribution gives a parabolic β profile, while a parabolic current distribution again gives a "S-shape" β with zero derivative both at $r = 0$ and $r = R_C$

3.4.2 Non-LTE and the electrodes

In the MFD-B and MFD-β models, local thermodynamic equilibrium (LTE) is assumed in the whole domain.

The simplest way to emulate the effects of non-LTE zones near the electrodes is to prescribe a different conductivity in a thin area next to the surface. This new conductivity function should partly depend on the cell resolution, but a simple alternative is to let the conductivity in this small region be independent of axial position, effectively saying conductivity in a cell here is equal to the conductivity in cell just above or below it, as illustrated in figure (3.2 left). More advanced approaches would be to estimate a gradient for the electron temperature based on the gradient for the calculated plasma temperature, as illustrated in figure (3.2 right).

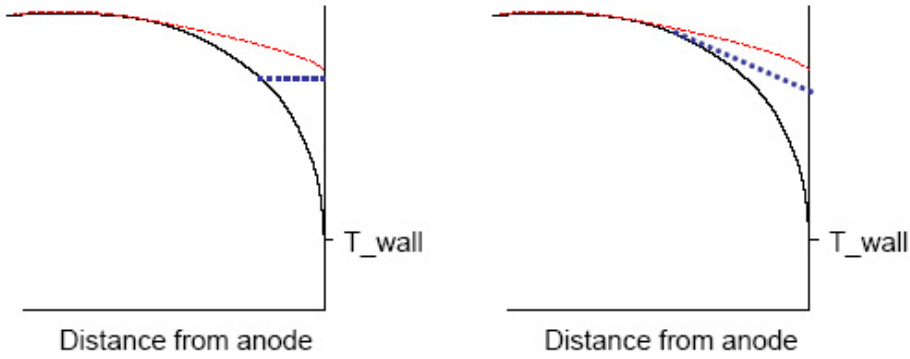

Figure 3.2: Illustrations of different simple non-LTE models. Left: setting the electron temperature equal to the plasma temperature one or more cells away from the anode. Right: estimating an electron temperature gradient based on the plasma temperature gradient.

A slightly different approach to the problem is to include part of the anode in the domain. Instead of prescribing the temperature at the anode surface, the temperature is given at some distance into the anode. This means that the material near the anode spot will be heated, and the temperature step and thus the gradient will be smaller.

Simple tests with both these approaches (separately and together) reveals the following: Without any non-LTE emulation, the arc has a tendency to 'punch holes' in

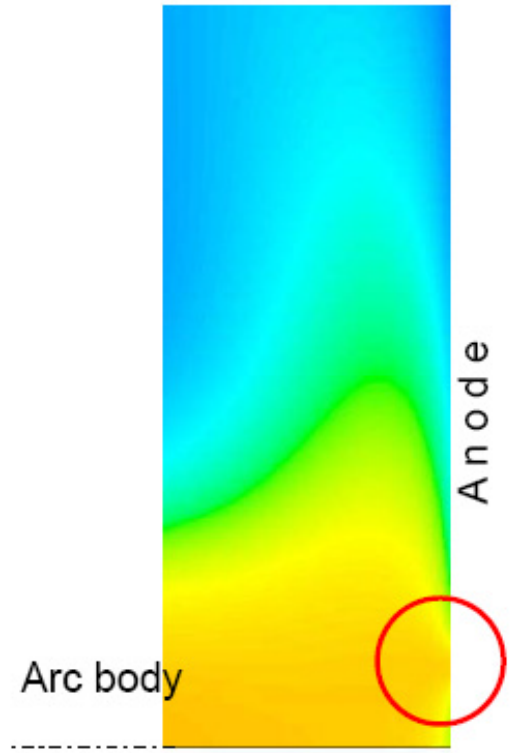

Figure 3.3: Section of a temperature plot showing how the current 'punches' through the anode barrier that forms when non-LTE effects is not taken into account. See also figure (6.17)

the low-conduction barrier near the anode, giving arc constriction that influences the direction of the arc plume. With a modified conductivity in the boundary layer, the arc seems to be more homogenous and stable towards the anode. The total voltage also drops for the arc, as do temperatures near the anode surface (due to less resistive heating).

For the cathode, the assumption of non-LTE again gives a too low conductivity and thus too much heating in the first mm or so of the arc. But since the current distribution at the cathode spot is given by boundary conditions, this should not significantly influence the direction of the forces or the shape of the arc.

3.5 The MFD model in full 3D

3.5.1 The 3D MFD equations

As derived above, the MFD-B equation in 3D fits the general transport equation form

$$\frac{\partial}{\partial t}(B_x) + \nabla \cdot (\vec{v}B_x - \Gamma_m \nabla B_x) = S_x$$

with source term

$$S_x = (\vec{B} \cdot \nabla)v_x - \frac{\partial}{\partial x}\vec{B} \cdot \nabla\Gamma_m \tag{3.39}$$

For low magnetic Reynolds numbers (lab scale arc), this reduces to

$$S_x = -\frac{\partial}{\partial x}\vec{B} \cdot \nabla\Gamma_m \tag{3.40}$$

In addition to the three $\vec{B}$ component equations, the flow equations get their source terms

$$j_x = \frac{1}{\mu_0}\left(\frac{\partial B_z}{\partial y} - \frac{\partial B_y}{\partial z}\right) \tag{3.41}$$

$$F_x = j_y B_z - j_z B_y \tag{3.42}$$
$$= \frac{1}{\mu_0}\left(B_y\frac{\partial B_x}{\partial y} + B_z\frac{\partial B_x}{\partial z} - B_z\frac{\partial B_z}{\partial x} - B_y\frac{\partial B_y}{\partial x}\right)$$

$$\dot{q}_{res} = \frac{j_x^2 + j_y^2 + j_z^2}{\sigma} \tag{3.43}$$

and similar by substitution for the other components.

3.5.2 Why things go wrong

As is seen from the above equations, the whole model in 3D depends heavily on the $\vec{B}$ gradient being accurate. But the gamma gradient in the MFD equation source term gives considerable rounding errors for large temperature gradients. Thus, the MFD-B model is risky to use for non-symmetric arcs.

The problem caused by the gamma gradient is basically the same as for the unscaled axisymmetric equations, but 3D makes it worse: When the temperature gradient ('edge of the arc') does not follow the grid, we get additional numerical diffusion.

Also, if the cell resolution is too low, the total $\vec{B}$ field may get 'spikes' at the maximum values where the derivative changes sign. All these factors add numerical error to the source term for the $\vec{B}$ equation.

Extensive testing show a tendency for errors to inflate as a too high gradient in one place is compensated by a too low gradient nearby, effectively giving a too high current plus a current in the opposite direction. Consequently, the square of the current, which determines ohmic heating, is too high and the temperature field becomes diffuse leading to a numerically more stable but physically wrong picture. Another tendency is that of a 'creeping current' along the outer wall (in either direction) to make the total current match the boundary condition.

Is it possible to reformulate (scale) the 3D equations like we could for the 2D case? Only to a certain degree, and with little practical use: By rewriting the 3D MHD-B equations to cylinder coordinates (including all tangential components), and scaling the B_θ and B_r equations, we can get source terms for these that contain a large and a small term rather than a subtraction of two of similar magnitude (assuming that the solution is near-symmetric). However, Fluent does not support 3D cylinder coordinates, and it would in any case be unsuited for systems far from cylinder symmetry.

3.5.3 Boundary conditions

Boundary conditions for the 3D MFD model are also problematic. For symmetric cases, or cases very near symmetric, we can use boundary values similar to in the 2D case. But problems start even in a relatively simple case like a constantly displaced arc (symmetric, but around a axis displaced from the reactor symmetry axis): In order to give correct $\vec{B}$ values on the walls for a non-symmetric arc, we must calculate them from the solution! The only other option is to assume that our walls are so far away from the arc that the magnetic field vanishes: letting $\vec{B}$ or its derivative go to zero. Choosing

$$\frac{\partial \vec{B}}{\partial r} = 0 \tag{3.44}$$

is the better option, as it does not force the field to be symmetric. Technically, if the walls are a little too close to the arc, it is possible to give the non-zero derivative corresponding to zero current at that distance.

These boundary conditions will allow an otherwise symmetric arc to have some instabilities or deformations, but they are not suitable for highly non-symmetric cases like rotating arcs or 'sideways' burning non-transferred arcs in plasma torches.

Chapter 4

The Vector Potential (MFD-VP) model

4.1 Motivation and background

The main goal of this work was to find a model that could simulate a rotating arc. The Source Domain model described later can perhaps be used for quick estimates *if* we know how fast the arc rotates and how it is deformed. The MHD-B and MFD-β models become unsuited for the Fluent solver in 3D. We need another type of MFD model.

Vector potential type models have a history of success. The basic idea is that instead of dealing with the $\vec{E}$ and $\vec{B}$ fields, we can use the less intuitive but mathematically just as good $\vec{A}$ and Φ fields. The electromagnetic equations then change form, but have the same solutions. The pitfall for this type of model is the boundary conditions for the vector potential: it is not very intuitive what different boundary conditions mean physically, and the $\vec{A}$ field is freely scalable, potentially making it meaningless to give a set boundary value.

4.2 Governing equations

Momentum and heat transport governed by equations 1.4 and **??** respectively. But we need equations for the electromagnetics involved.

As always, it is safe to start with Maxwell's equations:

$$\nabla \cdot \vec{D} = \rho_e$$

$$\nabla \cdot \vec{B} = 0$$

$$\nabla \times \vec{E} = -\frac{\partial}{\partial t}\vec{B}$$

$$\nabla \times \vec{B} = \mu_0(\vec{j} + \frac{\partial}{\partial t}\vec{D})$$

where $\vec{D} = \epsilon_0 \vec{E}$

One can rewrite the equations in terms of a magnetic *vector potential* $\vec{A}$ and a electric *scalar potential* Φ, defined by

$$\vec{B} = \nabla \times \vec{A} \tag{4.1}$$

which gives

$$\nabla \times \vec{E} = -\frac{\partial}{\partial t}(\nabla \times \vec{A}) = \nabla \times \frac{\partial}{\partial t}\vec{A}$$

$$\Leftrightarrow \nabla \times (\vec{E} + \frac{\partial}{\partial t}\vec{A}) = 0$$

since the curl of a gradient is zero, we define our scalar potential by

$$-\nabla\Phi = \vec{E} + \frac{\partial}{\partial t}\vec{A} \tag{4.2}$$

In order to find the most efficient equation set for our model, we want to simplify as much as we can. The first assumption is that we can neglect the displacement current so that

$$\nabla \times \vec{B} = \mu_0 \vec{j} \tag{4.3}$$

This gives a vector potential equation

$$\nabla \times (\nabla \times \vec{A}) = \mu_0 \vec{j}$$

Because the vector potential is defined *only* through the curl, the field can be freely scaled to suit our needs. Our need now is to simplify the left hand side

$$\nabla \times (\nabla \times \vec{A}) = -\nabla^2 \vec{A} + \nabla(\nabla \cdot \vec{A})$$

Choosing Coulomb gauge scaling so that $\nabla \cdot \vec{A} = 0$ we get a field equation for the vector potential that is very well suited for numerical solutions

$$\boldsymbol{\nabla^2 \tilde{\mathbf{A}} = -\mu_0 \tilde{\mathbf{j}}} \tag{4.4}$$

To obtain a similar equation for the electric scalar potential, we use the fact that electric current must be conserved. From Maxwell's equations we can find

$$\nabla \cdot \vec{j} = -\frac{\partial \rho_e}{\partial t}$$

Since the plasma is quasi-neutral by definition, we assume the charge density to be zero everywhere so that $\nabla \cdot \vec{j} = 0$. Also, since the plasma is a conductive media, we want to include Ohm's law in the equation. The simplest form of Ohm's law is

$$\vec{j} = \sigma \vec{E} = -\sigma(\nabla \Phi + \frac{\partial \vec{A}}{\partial t}) \tag{4.5}$$

where induced electric field, Hall effect and electron diffusion are ignored[40]. This gives

$$\nabla \cdot (\sigma \nabla \Phi) = 0 - \nabla \cdot (\sigma \frac{\partial \vec{A}}{\partial t}) \tag{4.6}$$

which essentially means that the current is divergence free and electrical charge is conserved in the system.

This equation would be exactly what we want if we can neglect the last term. For a stable and stationary arc $\frac{\partial \vec{A}}{\partial t} = 0$ and the term disappears. For the general, transient case, rearranging a little gives

$$\nabla \cdot (\sigma \frac{\partial \vec{A}}{\partial t}) = \frac{\partial \vec{A}}{\partial t} \cdot \nabla \sigma \tag{4.7}$$

Claiming that this term vanishes is not trivial. However, for an axisymmetric AC arc, $\vec{A}$ and thus its time derivative is almost exclusively in z-direction, while $\nabla \sigma$ is mainly in r-direction, giving a very small product of the two. For an unstable arc with sharp bends, this assumption may be a weak point in the model. Yet we must make it in order to get the equations on a form well suited for the Fluent solver. The scalar potential then becomes just

$$\nabla \cdot (\sigma \nabla \mathbf{\Phi}) = \mathbf{0} \tag{4.8}$$

This equation, together with the $\vec{A}$ field equation (4.4) forms the equation set for the electromagnetic part of the VP model.

For a very high current arc, Ohm's law must also include the induction term:

$$\vec{J} = \sigma(-\nabla \Phi + \vec{v} \times \vec{B})$$

and the Φ equation becomes the numerically much uglier equation

$$\nabla \cdot (\sigma \nabla \Phi) = -\nabla \cdot (\sigma \vec{v} \times \vec{B}) \tag{4.9}$$

4.2.1 Displacement current and free charges

We have made two assumptions without any argument: zero displacement current and zero charge density.

Zero free charge density is assumed when the plasma is quasi-neutral. However, in a very thin layer near the cathodes, there is a charge density because of the cathode voltage drop. One may argue that a very thin space-charge sheath also can exist around the edge of the arc in order to conserve the normal component of $\vec{E}$ across the large step in conductivity. However, these effects are on much smaller length scales than our cell resolution; on all resolved length scales we can assume quasi-neutrality.

If we include the displacement current, the equation for $\vec{A}$ gets extra terms:

$$\nabla^2 \vec{A} - \frac{1}{c^2}(\frac{\partial^2 \vec{A}}{\partial t^2} - \frac{\partial}{\partial t}\nabla\Phi) = \mu_0 \vec{j}$$

A order of magnitude analysis for the first of these terms gives

$$\frac{1}{c^2}\frac{\partial^2 \vec{A}}{\partial t^2} << \nabla^2 \vec{A}$$

Formally replacing $\frac{\partial}{\partial t}$ with ω and introducing a characteristic length l of 10 cm we get

$$\frac{1}{c^2}\omega^2 \vec{A} << \frac{\vec{A}}{l^2}$$

$$\omega^2 \vec{A} << \frac{c^2}{l^2}$$

$$f << \frac{1}{2\pi}\frac{c}{l} \approx 5 \cdot 10^8 \,\mathrm{Hz}$$

It is a safe assumption that any rotation or oscillation frequency in our reactor will never approach this frequency! Physically, this means that the time the current needs to flow through the system (at lightspeed) is much shorter than the timescale if the changes in the system.

For the second term we do a similar analysis with a characteristic $\sigma \approx 10^3$ S/m:

$$\frac{1}{c^2}\frac{\partial}{\partial t}\nabla\Phi << \mu_0 \vec{j}$$

$$\epsilon_0 \omega \nabla\Phi << \sigma \nabla\Phi$$

$$\omega << \frac{\sigma}{\epsilon_0}$$

$$f << \frac{1}{2\pi}\frac{\sigma}{\epsilon_0} \approx 2 \cdot 10^{13} \,\mathrm{Hz}$$

Again, a safe assumption!

4.3 Simplified equation set

For stationary and slowly varying cases, we then get the simple equation set

$$\nabla \cdot (\sigma \nabla \Phi) = 0 \tag{4.10}$$

$$\vec{j} = -\sigma \nabla \Phi \tag{4.11}$$

$$\nabla^2 \vec{A} = -\mu_0 \vec{j} \tag{4.12}$$

$$\vec{B} = \nabla \times \vec{A} \tag{4.13}$$

In addition, the normal momentum (1.4) and momentum (**??**) equations apply, with source terms for Lorentz forces, Ohmic heating, radiation and energy transport due to conduction electrons.

Note that unlike the MFD-B model, the simplified electromagnetic equations in the MFD-VP model are *not directly intercoupled*. The scalar potential depends *only* on the temperature field, the current only on scalar potential (and temperature), the vector potential only on the current and the magnetic field only on the vector potential. For this reason, the set is well suited for the unsteady solver: for a given temperature field at a given instant of time, all variables can be calculated (still assuming that variables are changing slowly enough for the second derivatives to be neglected).

4.4 Boundary conditions for $\vec{A}$ and Φ

One of the problems with non-symmetric current distributions is to find good boundary conditions. For the VP model, the following boundary conditions were used:

Anode: the current has to be normal to the anode surface. Since the magnetic vector potential generally has the same direction as the current, this corresponds to

$$\frac{\partial}{\partial z}\vec{A} = 0$$

Further, the anode must be an equipotential surface with $\Phi = 0$ on the whole conducting surface

Walls and cathodic electrode outside the cathode spot: no current through the surface gives

$$\frac{\partial}{\partial x}_n \Phi = 0$$

but vector potential BCs are not trivial: the $\vec{B}$ field decays toward zero far from the arc, but the $\vec{A}$ field does not necessarily do that. Analytic solution of the $\vec{A}$ field for a long straight wire show that $\vec{A}$ goes toward a constant limit (depending on current and wire length). But because the $\vec{A}$ values never are used directly in any computations (only $\nabla \times \vec{A}$), it can be scaled freely, for example so that the limit value is zero. Thus we have two choices at the walls: either we can approximate by letting

$$\vec{A} = 0$$

or we can approximate by letting

$$\frac{\partial \vec{A}}{\partial x_n} = 0$$

Testing for symmetrical arcs show that the two choices give very similar results (see figures 6.12-6.16). However, for non-symmetrical cases the zero derivative seems a safer choice, just like $\frac{\partial \vec{B}}{\partial x_n} = 0$ is a better choice than $\vec{B} = 0$ for non-symmetric cases.

For the cathode outside the cathode spot, neither of these choices are particularly satisfying, but there are not many better alternatives. In the axi-symmetric case, $\vec{A}$ and $\vec{B}$ are known at the cathode surface. But if the arc curves these results are no longer true. Thus some kind of assumption must be made.

Cathode spot: current normal to the surface with a given distribution:

$$\frac{\partial \Phi}{\partial x_n} = j_c(x, y)$$

For symmetrical cases, the proposed set of boundary conditions give very good results compared to experiments. For non-symmetrical cases, the boundary conditions give qualitatively correct results, but there are no other models to validate against. The 'correct' way to solve the problem would be to compute the whole $\vec{A}$ field directly from the current distribution by means of integration (using Biot-Savart's law). This is a very large computation, as we in each cell that we want the magnetic field have to consider the contribution from every cell in the system with current passing through it. Some simple tests have been made to compare the magnetic field from a 'bent' wire to our 3D boundary conditions, with promising results. However, because of the size of the problem it was considered impractical to include this in the present models.

4.4.1 Errors in the magnetic field outside the arc

As shown by figure (6.16), the product $\beta = r\vec{B}$ is not uniform outside the arc in the VP model simulations for either choice of boundary condition. This indicates that the computed magnetic field decays too fast.

However, it *does not matter if we get some error* in the magnetic field as long as the error is outside the current bearing arc. This is because in the VP model (unlike the MHD-B and -β) the magnetic field itself does not enter into our equations, but only the product $\vec{j} \times \vec{B}$. Consequently, wherever the current is negligibly small, any error in the computed magnetic field do not have any consequences for the temperature and gas flow in the reactor. This is one of the hidden strengths of the VP model, as fluctuations in the electromagnetic fields before they have converged do not give rise to large instabilities. It also means that the difference between the two choices for vector potential boundary condition becomes smaller.

4.5 Modeling arcs in external magnetic fields

In order to model arcs influenced by external magnetic forces, we must include the external contribution to the total magnetic field. The idea used in this work is that because of the superposition principle, the constant external field contribution $\vec{B}_{ext}$ can be separated from the total field. Being curl-free, $\vec{B}_{ext}$ vanishes from the $\vec{B}$ field equation. The $\vec{A}$ field equation must then be solved for the modified $\vec{B}_0$ field *which has the same boundary conditions as a free-burning arc.* This is shown in more detail in section 7.2

Thus, the $\vec{A}$ equation solution gives the $\vec{B}_0$ field, and the external contribution is just a position- and/or time-dependent constant to be added. Because all the equations are coupled, the solution is the same as if solving the total field directly, as long as the boundary conditions represent the same physics.

Chapter 5

Source-Domain (SD) Model

5.1 Motivation and background

When dealing with a real and operating reactor, beautiful modeling results have little value if they arrive months too late. Often all we want is a qualitative verification of whether a proposed change in geometry or operating parameters will change the results in the right direction. When any unneccesary time spent means a costly delay, we want a method that is as fast and simple as possible, even at the expense of accuracy. Other times, the actual reactor design is too complicated to model reliably by *any* method within the time frame of the project.

This is where the SD model comes in. It is designed to be fast to implement and even faster to use. The results were originally intended to be treated qualitatively only, but we will see that for certain types of cases and with smart assumptions this fast-and-simple model can reproduce the results of the other methods quite well.

5.1.1 How simple can it get?

All the arc models in this work follow the same pseudo-structure:

• By some means compute current density and magnetic field from temperature and boundary conditions
• Solve the flow and temperature equations with source terms for Lorentz forces, resistive heating and radiation.

The difference between different models in this work is how to do the first part: how the reactor conditions affect the arc. The second part, how the arc affects the reactor conditions, is the same for all the models.

The simplest model possible is then one where *only* the second part is considered.

No extra transport equations are introduced, only source terms for energy and momentum that are given *a priori*. We can think of this almost as pasting a previously computed arc into our domain: the arc itself is then fixed, but we compute how it affects the rest of the domain. The strength of the SD model is then that this last computation will be very quick, and thus saves a lot of time when comparing several possible geometries.

In the PPM project work, different variations of the SD model were used, as described below.

5.2 Assumptions and source terms

Obviously, since we are not calculating the current distribution, we must make assumptions. Basically, we must either assume a solution for the current distribution and calculate our source terms from this, or else we must assume values for the source terms directly.

5.2.1 Variant I: prescribed power source

This variant, illustrated in figure (5.1), is based on two assumptions: one for the total power in the arc, and one for the 'typical' current or current distribution in the arc. The power and momentum sources are in other words assumed independent of each other, and are numerically decoupled. This appears to be bad physics at first glance, but the extra independent variable also makes the model more adaptable.

In the PPM project, the relevant arc was assumed to be rotating fast enough that it could hopefully be modeled as a smeared-out cone. A quickly apparent problem with this thought was that an arc shaped like a hollow cone would have a much higher resistivity (and thus total power) than a rod-shaped one. Assuming a realistic total power (based on similar previous experiments) distributed within the arc seems to be the better choice in this case.

For the momentum source, there is also a choice; One option is to use a time-averaged or 'typical' current density, compute the magnetic field from that and use the resulting computed force. Another option is to somehow estimate or compute the time-averaged magnetic field or time-averaged force. This approach is based on an implicit assumption that the arc isn't really a hollow cone at every instant, but rather rotates fast compared to the gas velocities through the arc zone. For this variant of the SD model, any of these options are possible.

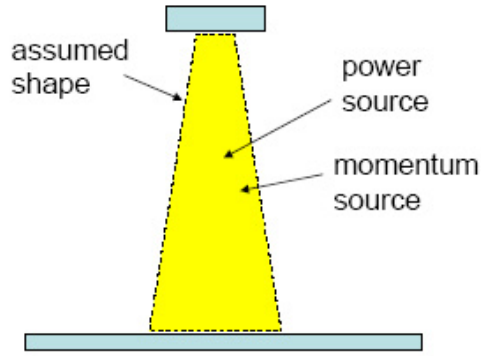

Figure 5.1: Illustration of the SD-I model. The arc domain has a given power distribution and a given force distribution

Preliminary conclusion: this variant can be adapted to exotic cases, but must be carefully used.

5.2.2 Variant II: prescribed current distribution in the arc zone

The SD-II variant, illustrated in figure (5.2) and used in f.ex.[1][30][32] but also in newer work like [43][59], is in its way both simpler and more advanced than the one above. Basically, only the current distribution needs to be assumed, and the magnetic field is calculated from the current. The momentum source then only depends on the assumed current distribution, and the heating source depends on the current and the temperature field.

The advantage is then that the forces and the heating power will be consistent with each other. Another possible advantage is the ability to estimate the voltage drop for a given arc shape. The limitation of this SD model variant is for dynamic cases (such as described above) where one can only assume 'typical' or average current distributions.

Of course, we must be able to make a good assumption for the shape and current distribution of our arc. The distribution can in some cases be found experimentally, from high-speed camera footage and measurements. Another option is to import a computed distribution from another model. Also, the shape and current distribution for simple arcs can be found in literature or even computed analytically as in [47].

Preliminary conclusion: this variant is good for stationary arcs where the current distribution is more certain.

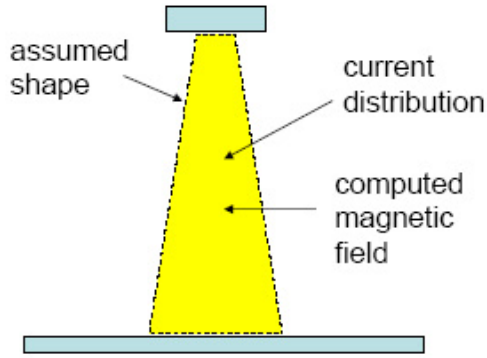

Figure 5.2: Illustration of the SD-II. The arc domain has a given current distribution that gives a magnet field. Power is calculated from $\vec{j}^2/\sigma(T)$ and force from $\vec{j} \times \vec{B}$

5.3 How reliable are the SD results?

One basic law in numerical simulations is commonly phrased as "garbage in = garbage out". Results from the SD model cannot be correct if we make very wrong assumptions. However, it is of prime importance to investigate how sensitive the results are to variations in the assumed distributions. Also we must compare the SD results for 'good assumptions' to results from other models. Yet it must be possible to find 'good assumptions' without knowing the solution first, or the whole purpose of the SD model is forfeit.

In a previous work [59] we compared the SD model with a 2D MFD-β model for a simple straight free-burning arc. The basic assumptions were straight conical or parabola-shaped arcs, and a homogenous or parabolic 'reasonably high' current density across the arc section. The results were reassuring in that even for the 'poor guesses', all qualitative features of the solution were correct. The general trends were that the temperature and velocity fields outside the arc matched very closely, like in figure (5.3), but that the computed arc voltage from the SD model was 5-30 percent too high for the otherwise best matches (the higher total power is balanced by increased radiation loss, allowing a matching temperature field).

Another very interesting result from this test was that Ar arcs were best modeled by a straight cone, while He arcs matched the parabolic shape better. This is associated with the arc behaviour near the anode that was discussed in chapter 2.5.2.

Preliminary conclusion: For simple arcs, the computed temperature and flow out-

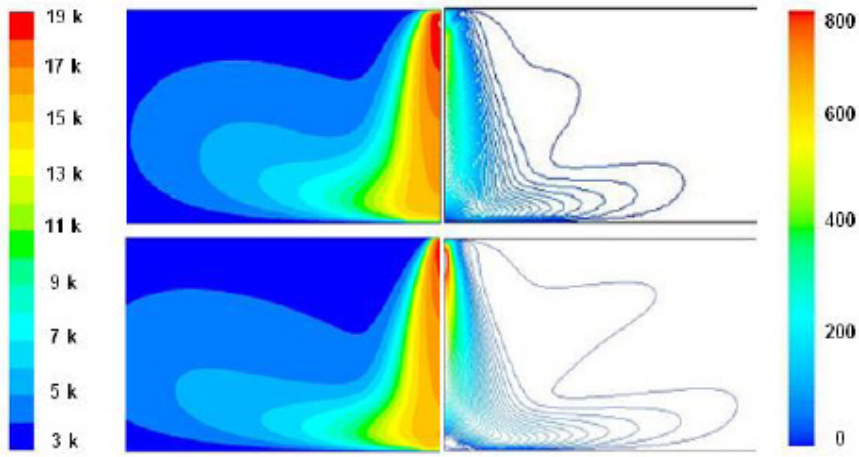

Figure 5.3: Comparison between SD-B (top) and MFD-beta (bottom) models. Temperature and velocity. Very good match considering the simplicity of the SD model.

side the arc can be reasonably well modeled by quite simple assumptions. Computed values for total power and voltage must be treated with some caution.

5.4 Particle flow and recirculation with the SD model

Given the simple and robust structure of the SD model, it is easy to add new features to the simulations. Of particular interest in the PPM project was the addition of particle dynamics via the DPM (Discrete Particle Model) package in the Fluent environment. This enabled us to investigate streamlines and recirculation patterns of injected particles rather than just the gas flow, and was used to optimize the placement of injection lances in the PPM-reactor. This work was mostly performed by Dr. B.Ravary[58] and is not central in this thesis, but serves as a good example of the practical usefulness of the SD model. Some results for particle paths in the SD model are included in Appendix E.

Chapter 6

Results: Free-burning arcs

The standard cases form the skeleton of this work. All model improvements were tested and compared on reference cases: 10 cm 1 kA axisymmetric arcs in 1 bar Ar and 0.6 bar He atmospheres, both with parabolic current distribution over a 5 mm radius cathode spot (average current density $4/\pi \cdot 10^7 \approx 1.27 \cdot 10^7 \mathrm{A/m^2}$). The outer walls of the domain were initially modeled as walls, but later typically implemented as pressure outlets to allow a smaller domain and thus faster computations.

The relevant models and default boundary conditions are described in chapters 3-5. Note that the models are grid sensitive. In many cases, a somewhat coarse grid has been used to speed up computations. This can explain apparent inconsistencies between different series. Also, the approach to the non-LTE problem near the electrodes affects the computed maximum temperature under the cathode spot.

See also chapter 9 for results for upscaled free-burning arcs.

6.1 Comparison of SD-II vs MFD-β models on axisymmetric arcs

Figure 6.1 shows the concept of this series: We want to investigate how much the results given by the SD-II model (prescribed current) deviate from those computed by the MFD-β model. It is also of interest to investigate different types of assumed current distributions.

The total current and cathode spot radius were the same as for the corresponding MFD case.

Figure 6.1: Illustration of SD-II vs MFD-β models. The SD-II model assumes the arc has a simple shape, the real current distribution is more complex (shown here for a He arc)

6.1.1 Different SD-II model parameters for the same arc

Figures (6.2-6.5) show the results for different expansion factors in the SD-II parabola-like ("Ramakrishnan") arc. The expansion factor C_e is defined by the assumed shape of the arc

$$R(z) = R_c \left(1 + \sqrt{C_e \frac{z}{R_c}}\right) \tag{6.1}$$

where $R(z)$ is the arc radius and R_c is the given cathode spot radius. In all cases shown, the current distribution in the arc was assumed to be parabolic over the cross-section:

$$j_z(r) = \frac{2I}{\pi R^2}(1 - \frac{r^2}{R^2})$$

The relevant figures show the computed temperature field for different assumptions of C_e, and illustrates the difference between good (6.3) and poor (6.5) assumptions.

The good news here is that even the poor assumptions give the same qualitative results. In other words, as long as assumed expansion factor is reasonable[1], the SD-II model is useful for any system with a stable free-burning arc.

6.1.2 Different arc lengths

Figures (6.6-6.7) show results for shorter and longer He arcs as well as for an Ar arc.

[1] reasonable values for the arc expansion factor are suggested in various publications like [47][30]. Note that the factor is sometimes defined outside the square root, sometimes inside.

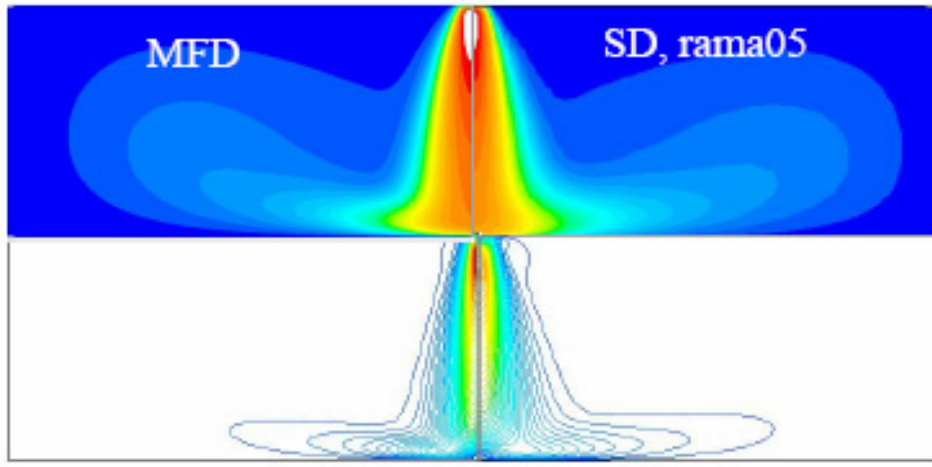

Figure 6.2: Computed temperature and velocity magnitude for a 10 cm He arc. MFD-beta model vs SD-II model with expansion factor 0.5

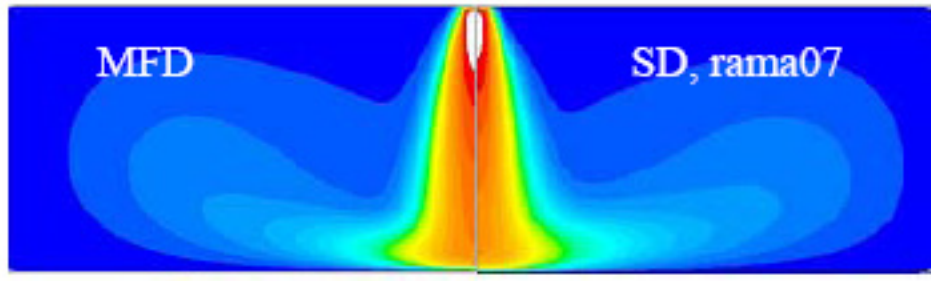

Figure 6.3: Computed temperature for a 10 cm He arc, MFD-beta vs SD-II with expansion factor 0.7)

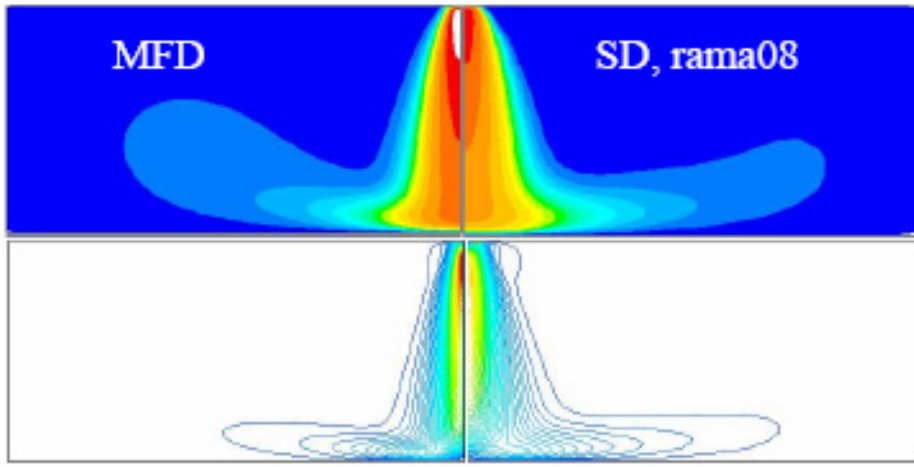

Figure 6.4: Computed temperature and velocity magnitude for a 10 cm He arc, MFD-beta vs SD-II with expansion factor 0.8

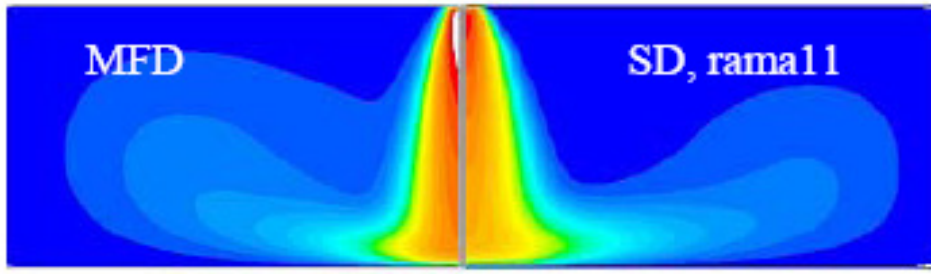

Figure 6.5: Computed temperature for a 10 cm He arc, MFD-beta vs SD-II with expansion factor 1.1

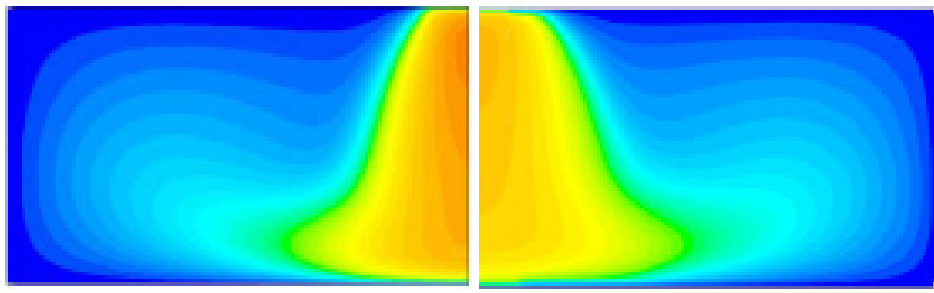

Figure 6.6: Computed temperature for a **3 cm** 1 kA He arc. MFD-beta vs SD-II model with expansion factor 0.8

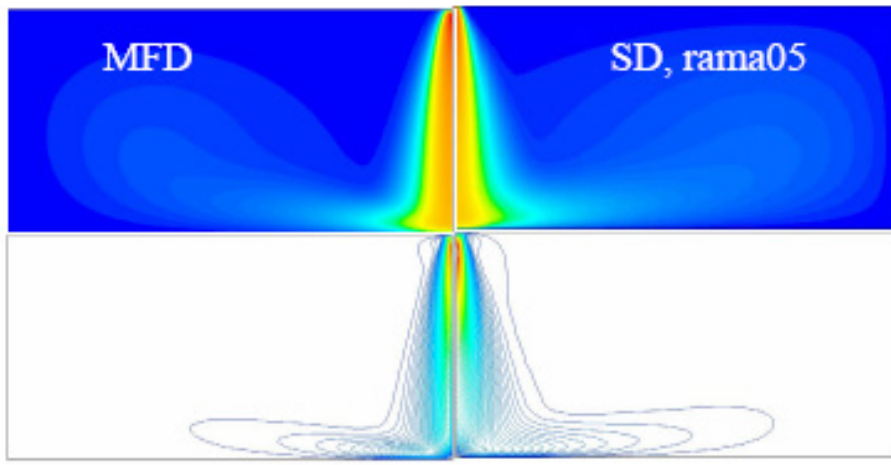

Figure 6.7: Computed temperature and velocity magnitude for a **20 cm** 1 kA He arc. MFD-beta vs SD-II model with expansion factor 0.5

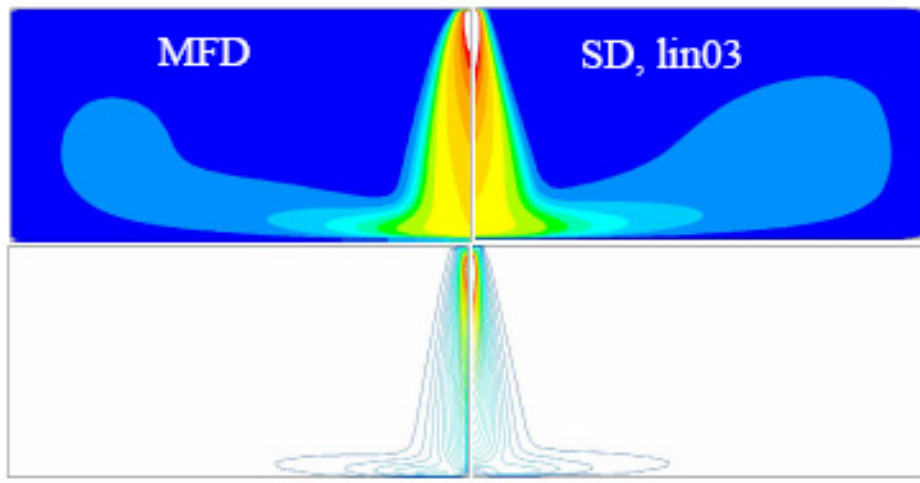

Figure 6.8: Computed temperature and velocity magnitude for a 10 cm 1 kA Ar arc. MFD-beta vs SD-II model

Note that there is no universal 'best assumption'. The expansion factor that gives the best match seems to depend heavily on arc length: shorter arcs need a larger expansion factor and longer arcs a smaller one. Also, as previously pointed out, argon and helium arcs behave differently near the cold anode. In this work it was found that even though the 'body' of an Ar arc is parabolic, the extra expansion near the anode makes for a better fit if the arc is modeled as a straight cone, unless the arc is very long. Helium arcs are better modeled as parabolic.

The SD results in these series all show the correct qualitative behaviour when compared to the MFD-beta results, and give good estimates for velocity and temperature *in the reactor outside the current conducting arc*. The computed voltage[2] and total power in the SD-II arc is typically too high by 30-100%, but can in some cases be too low. Where the ohmic heating from the prescribed current is too high, radiative heat loss is also correspondingly higher and vice versa. The results indicate that most of the extra arc power is lost by radiation, i.e. that the total (conductive and convective) energy transport to the gas outside the arc is much more realistic. The computed temperature fields are then still *realistic outside the arc*.

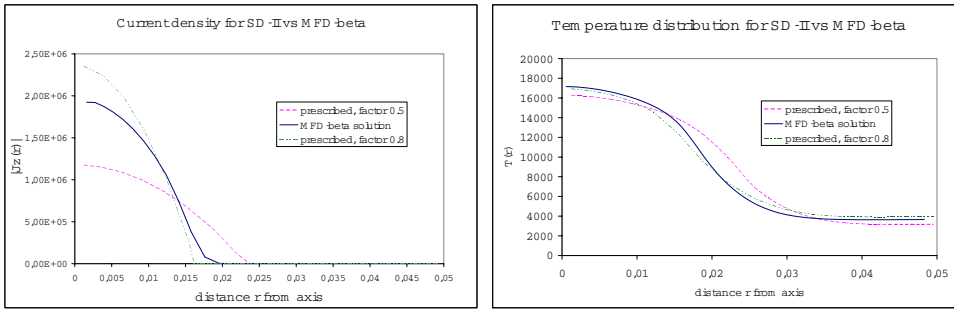

Figure 6.9: Current and temperature distributions halfway between cathode and anode. SD-II solutions for two different expansion factors vs the MFD-beta solution (best match, factor 0.7, is not shown in this plot).

All the displayed results show *lower* max temperatures in the prescribed current arc than in the computed ones. As seen in figure (6.9), the real current is very close to parabolic. The SD-II model could the be improved by investigating how the optimal expansion factor scales with arc length. However, effects of cathode spot bound-

[2]the voltage is obtained by integrating the total power and thus does not include any cathode or anode voltage drop

ary conditions and radiation model must also be included before we can draw rigid conclusions.

6.2 Boundary condition tests for the VP model

As discussed in chapter 4, boundary conditions for the vector potential $\vec{A}$ are not intuitive: we have a choice between giving values for the magnetic vector potential components themselves (Dirichlet condition) or for their normal derivatives (Neumann condition). Running a *test to compare the two options for the A_z component*[3] is therefore interesting. An illustration is provided in figure (6.10). Results are displayed in figures (6.11-6.16)

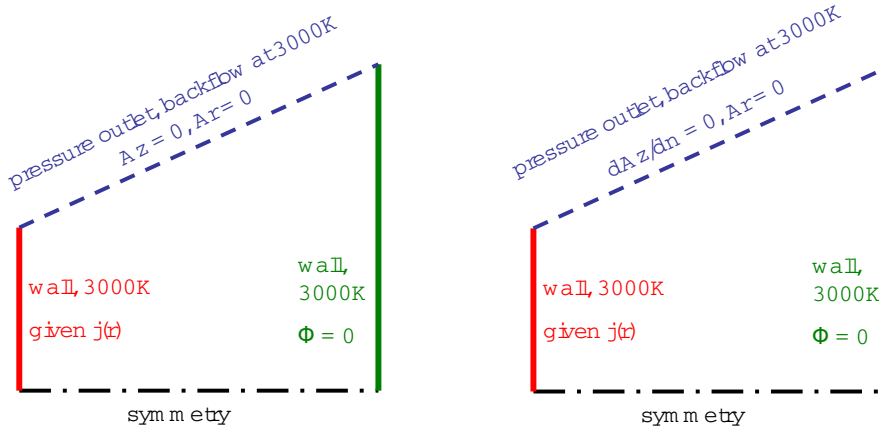

Figure 6.10: Illustration of the boundary condition test series. The only difference is the condition for A_z at the outer edge.

As shown by the figures, there is almost no discernable difference in the computed fields. Apart from the A_z itself, only the magnetic field shows a small deviation near the changed boundary. However, plotting of the β parameter (fig. 6.16) reveals that *both* choices of boundary condition gives a computed magnetic field that decays too fast outside the arc. Fortunately, *as long as the magnetic field inside the arc is correct the solution for the temperature and velocity fields will also be correct* as the magnetic field only affects them through the Lorentz force $\vec{j} \times \vec{B}$ which is negligible outside the arc.

[3] the $\vec{A}$ field is near axial, so the A_r component is not very relevant

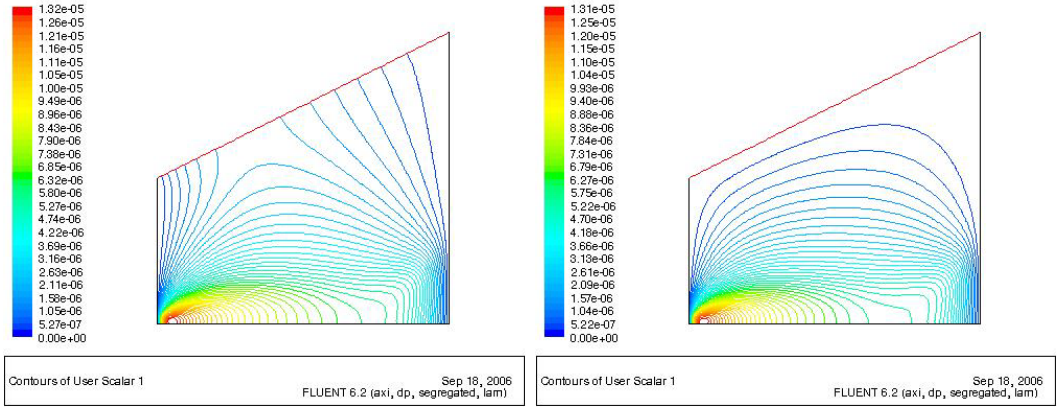

Figure 6.11: Comparison of Dirichlet and Neumann boundary conditions: Computed A_z component

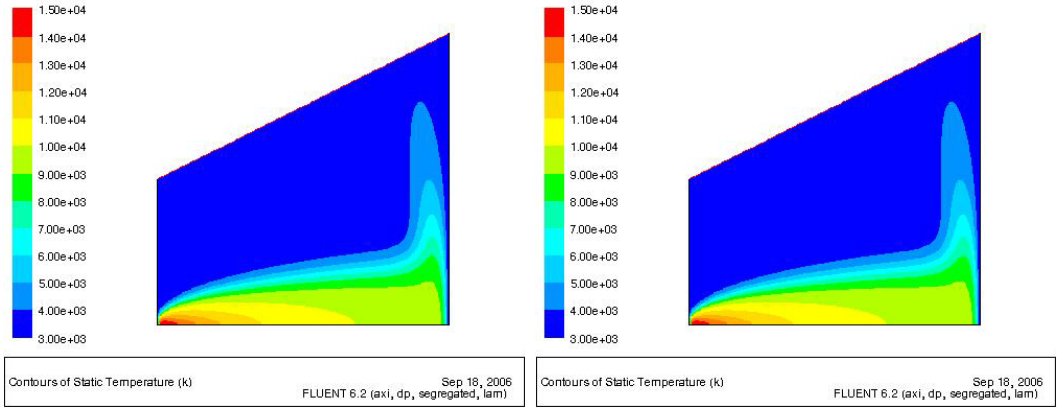

Figure 6.12: Comparison of Dirichlet and Neumann boundary conditions: Computed temperature distribution

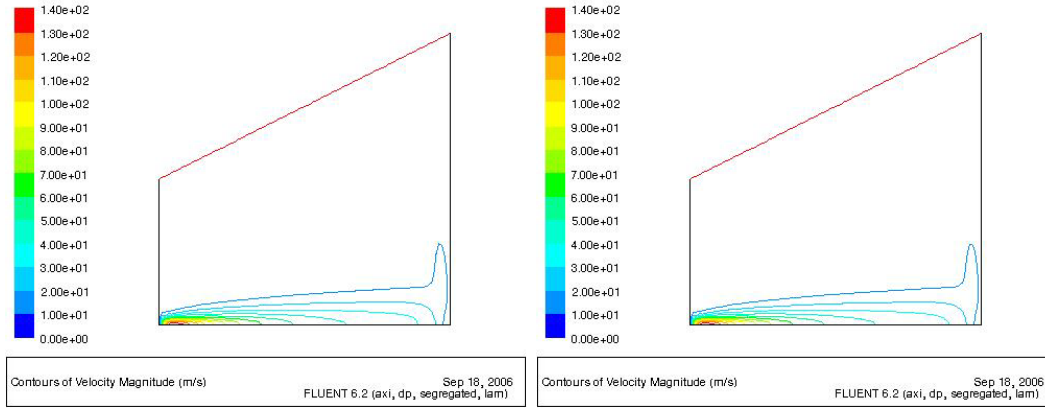

Figure 6.13: Comparison of Dirichlet and Neumann boundary conditions: Computed velocity distribution

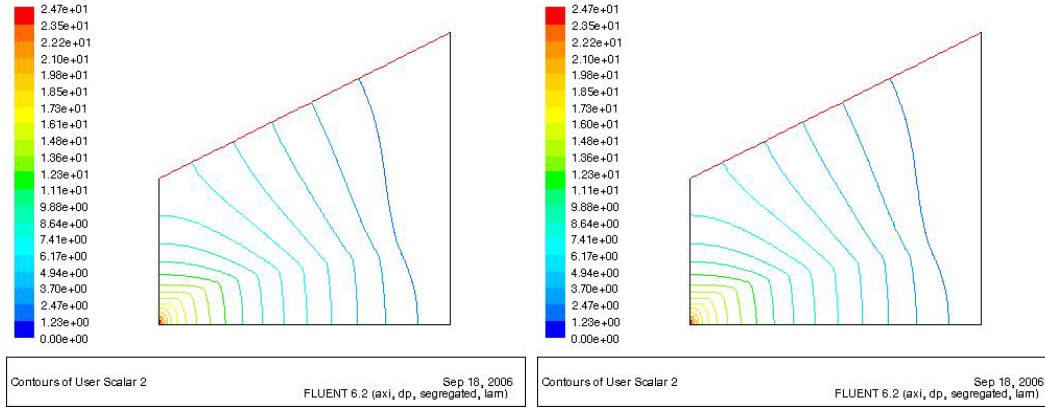

Figure 6.14: Comparison of Dirichlet and Neumann boundary conditions: Computed electric scalar potential

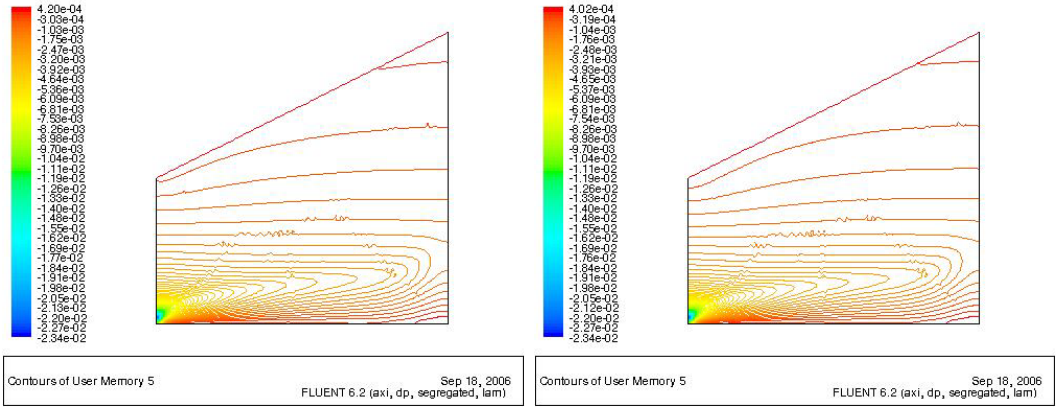

Figure 6.15: Comparison of Dirichlet and Neumann boundary conditions: Computed magnetic field ($B_\theta = \nabla \times \vec{A}$)

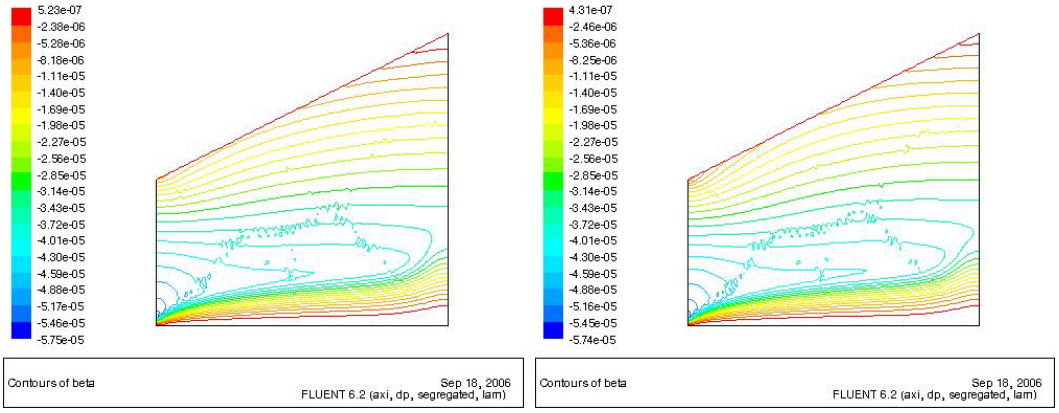

Figure 6.16: Comparison of Dirichlet and Neumann boundary conditions: Computed $\beta = rB_\theta$. Both boundary conditions give a field that decays too fast outside the arc.

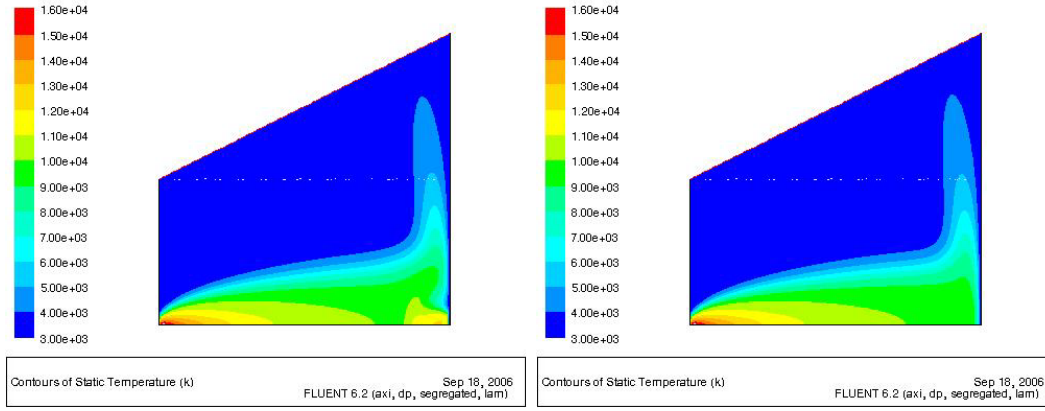

Figure 6.17: Comparison of no 'LTE-fix' (left) vs given conductivity in the bottom cells in the reactor (right). 1 kA 10 cm Ar arc. The arc constriction at the anode seen on the left is not realistic.

6.2.1 LTE-fix at anode

A much larger difference in temperature and gas flow is seen when changing the conditions in the presumed non-LTE zone near the anode. Figure (6.17) shows temperature profiles for the case with no 'LTE-fix' vs the simplest model where the bottom of the anode (3 mm in this case) simply has a given conductivity. As shown, the cooling near the anode gives a unrealistically high resistance if assuming perfect LTE, and this forces the arc to contract and punch a 'hole' in the barrier. With all the types of LTE-fixes used in this work, this tendency of arc constriction at the anode is removed and the arc gets a realistic shape.

6.3 PPM geometry studies with the simple SD-I model

These simulation series were done with the SD-I model, where the energy and momentum sources are prescribed independently. The important design criterion was whether proposed reactor geometries would give satisfactory recirculation of gas in the PPM reactor. The crucial assumption was that a very fast rotating arc could be modeled as a *stationary hollow cone*. A momentum source was computed from an assumed current distribution, and a reasonable total power was distributed homogeneously in the source domain. No radiation model was implemented yet for the plasma, as only qualitative trends in the gas flow pattern (i.e. recirculation or not) were investigated. The geometry was axisymmetric. The top of the tubular anode was modeled as floating inside the reactor, to emulate the passage of gas through holes in the bottom of the anode. For more on this type of modeling and more

results, refer to the early PPM project reports [57][58]

Because of the limitations of the numerical model at the time of these computations, only qualitative gas flow patterns were investigated. For the displayed cases (fig. 6.19-6.24), the total power is indicated on the figures. The momentum source is computed assuming a 1 kA, 5 mm radius arc subject to the axisymmetric magnetic field given by the time-averaged (hollow cone) arc.

Figure (6.18 left and right) show the real and simplified PPM reactor geometries, respectively.

The anode is modeled as floating inside the reactor and its position can be adjusted, corresponding to the different simulated geometries. The rounding of the cathode tip is ignored in several series to enable an orthogonal grid. The symmetry line is by default vertical in Fluent geometries and most plots are therefore rotated compared to the real geometry.

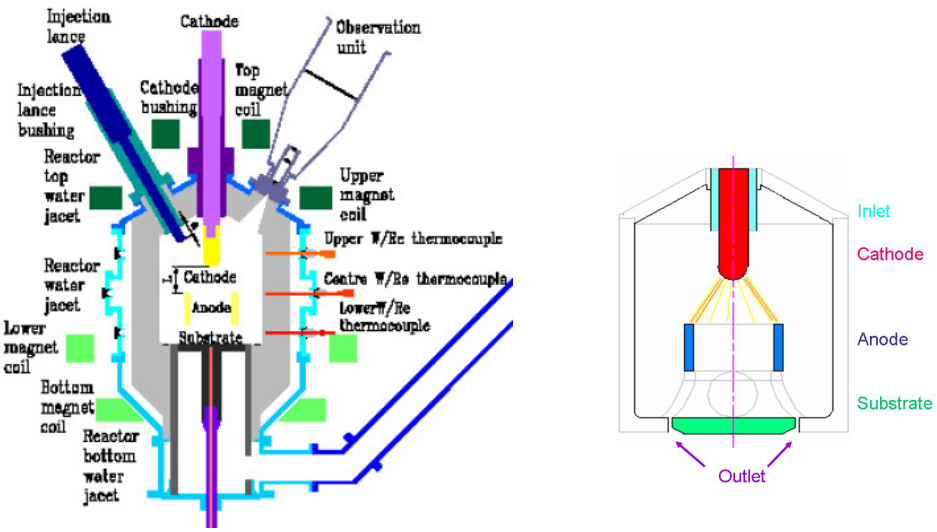

Figure 6.18: *Left*: The real PPM reactor geometry. The anode is hollow and the bottom conical part has holes to enable gas flow through it. The diameter of the anode is 20 cm, corresponding to geometry '*B*'. *Right*: Illustration of the simplified reactor geometry used in simulations.

6.3.1 Different anode geometries

Figures (6.19-6.21) show computed streamlines for the different anode geometries A ("wide"), B ("medium") and C ("narrow"). The arc length (12 cm), assumed total power (10 kW) and computed momentum source are the same for all geometries.

The arc is modeled as an axisymmetric source domain. Figures indicate that if the anode is too narrow (geometry C), much of the injected gas will pass outside the hot zone.

The quality of these results can be questioned as the assumed arc shape is far from realistic. A realistic arc would, in addition to all non-symmetric effects, typically burn straight down a short distance from the cathode before curving out towards the anode. See the discussion on rotation in chapter 8 for more on this.

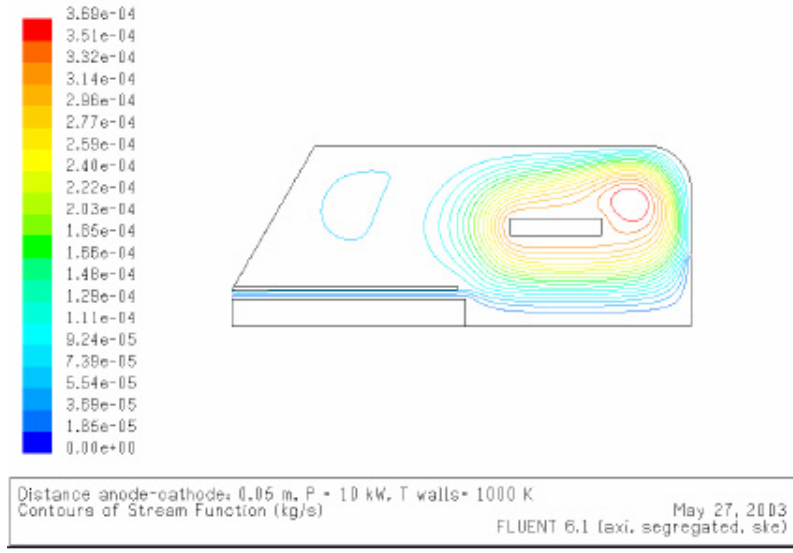

Figure 6.19: Computed streamline pattern for proposed anode geometry "A" (wide anode opening) in the PPM reactor. Arc is modeled as a symmetric source domain with 10 kW power.

6.3.2 Different arc parameters on same geometry

Figures (6.22-6.24) show computed streamlines for different arc assumptions on geometry B. The arc length is the same, but current and assumed total power varies. The injected flow inertia is negligible and the magnetically driven cathode jet dominates the system, giving generally good recirculation. The figures indicate that for higher current arcs with correspondingly higher velocities, the gas accelerated in the arc may hit the anode at sufficient speed to be deflected and set up a secondary recirculation pattern near the arc.

The quality of these results can be questioned as the assumed arc shape is far from

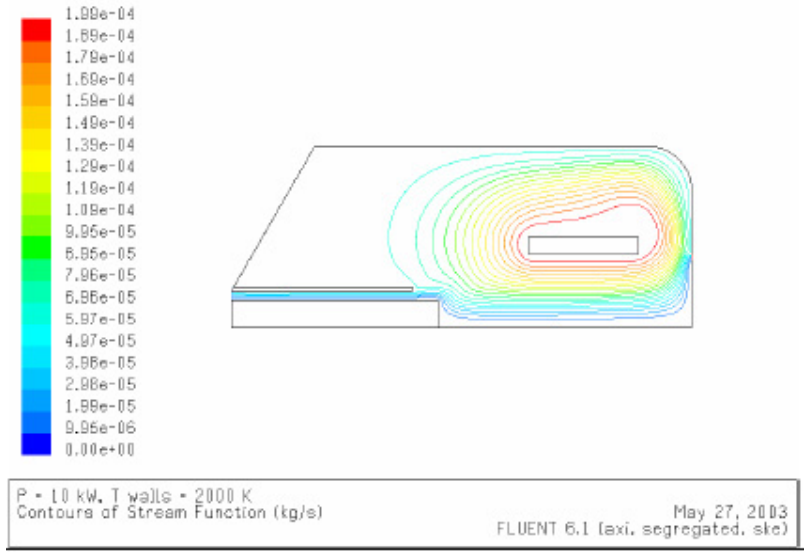

Figure 6.20: Computed streamline pattern for proposed anode geometry "B" (medium anode opening) in the PPM reactor. Arc is modeled as a symmetric source domain with 10 kW power.

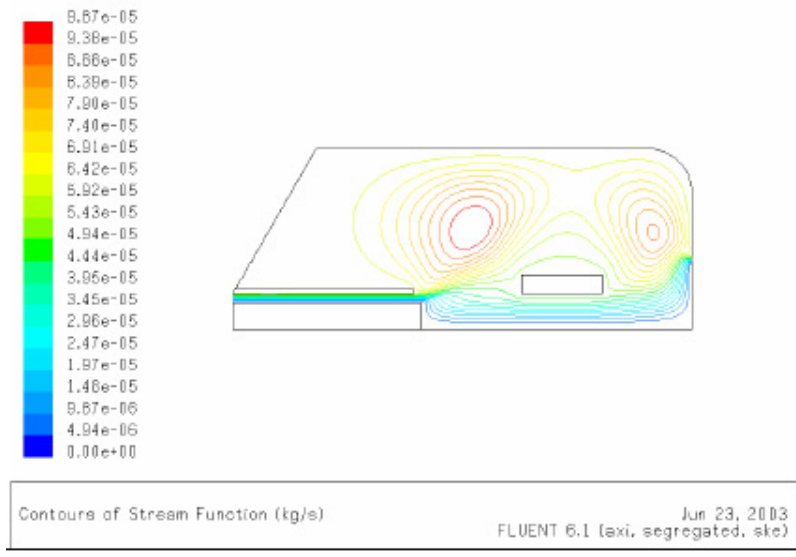

Figure 6.21: Computed streamline pattern for proposed anode geometry "C" (narrow anode opening) in the PPM reactor. Arc is modeled as a symmetric source domain with 10 kW power.

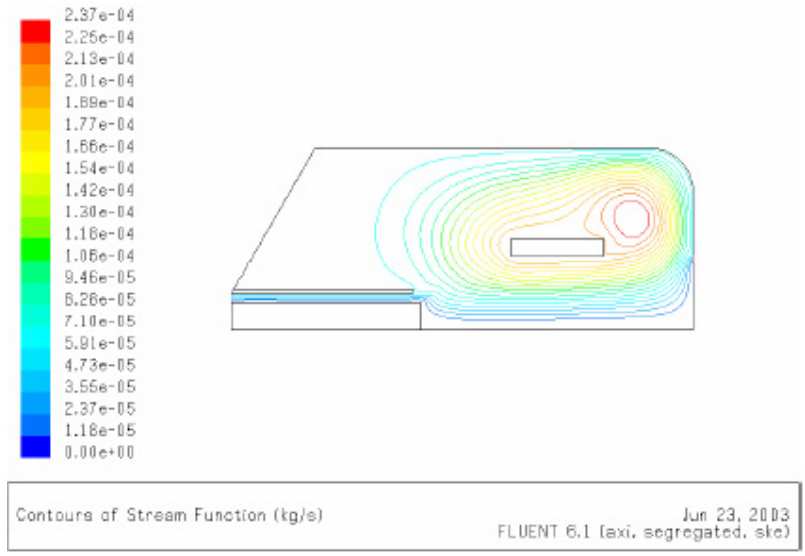

Figure 6.22: Computed streamline pattern for proposed anode geometry "B" in the PPM reactor. Arc is modeled as a symmetric source domain with 25 kW power. Recirculation is smooth and global.

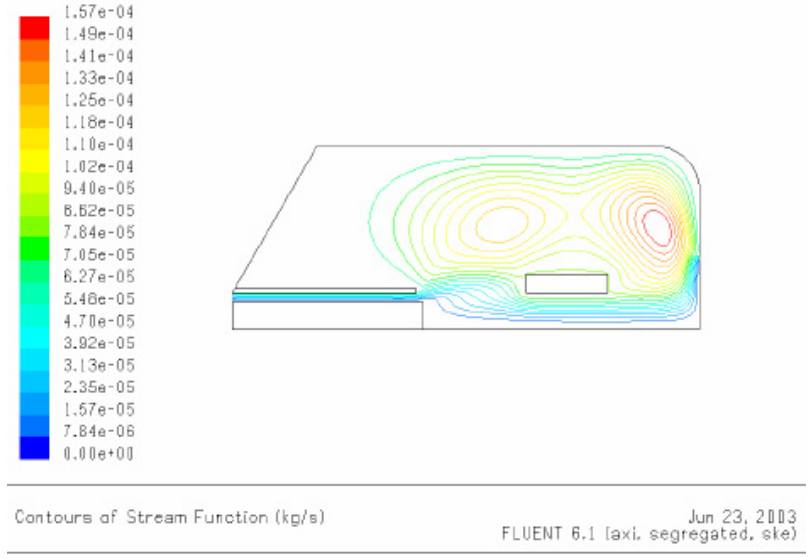

Figure 6.23: Computed streamline pattern for proposed anode geometry "B" in the PPM reactor. Arc is modeled as a symmetric source domain with 50 kW power. A secondary Recirculation pattern emerges due to high velocity gas being deflected off the anode top.

realistic. Also, the given arc powers are unrealistic due to the lack of advanced radiation model at this stage of the modeling: a real arc would have higher total power due to high radiation loss, but hopefully more comparable convective and diffusive energy transport.

6.4 Argon and He-C mixtures - VP model studies

This series was done with the VP model to show how the different material parameters lead to different types of arcs. All the simulated arcs are stationary, axisymmetric and made with the same assumptions on the same grid. Results are shown in figures (6.25-6.28) for Ar, He 1 and 0.6 bar as well as for a 10% He-C mixture.

For the 50% He-C mixture and pure C systems, the results are not stable for the boundary conditions used for the other materials. This is likely caused by the high emitted radiation (discussed in section 2.6.2) giving a higher energy loss than the ohmic heating can sustain. Because the model maintains a constant current regardless of arc voltage[4], the arc cannot be extinguished but instead goes into unphysical quasi-periodic behaviour. The 'hairs' in figure (6.29) are caused by the arc expanding and contracting again, giving magnetic forces pushing the gas from both above and below making a temperature bulge where the current is free to expand and contract even more. These 'hairs' typically move a bit up and down the arc and grow and shrink some, but the qualitative picture remains similar throughout these simulations that never converge properly. In reality, arcs in these gas mixtures must be expected to be difficult to maintain without artificial stabilisation.

The results indicate how the system changes with the plasma gas composition. Lower pressure gives correspondingly lower radiation density and thus slightly higher temperatures. Adding just 10% carbon vapour dramatically increases radiation at lower temperature (glowing bright green instead of faint purple), but also increases electrical conductivity. The combination gives an arc shape more resembling that in argon, with the arc body significantly cooler than for pure He, but without this cooling leading to severe constriction near the anode or to arc extinction.

The non-converged simulations indicate that a too high carbon concentration will give stability problems and voltage spikes. Indeed, on the first attempt with carbon black injection into the arc, the arc was extinguished. On subsequent experiments the carbon feed rate has been controlled to avoid over feeding.

[4]the model assumes an ideal constant current power supply without voltage limitations

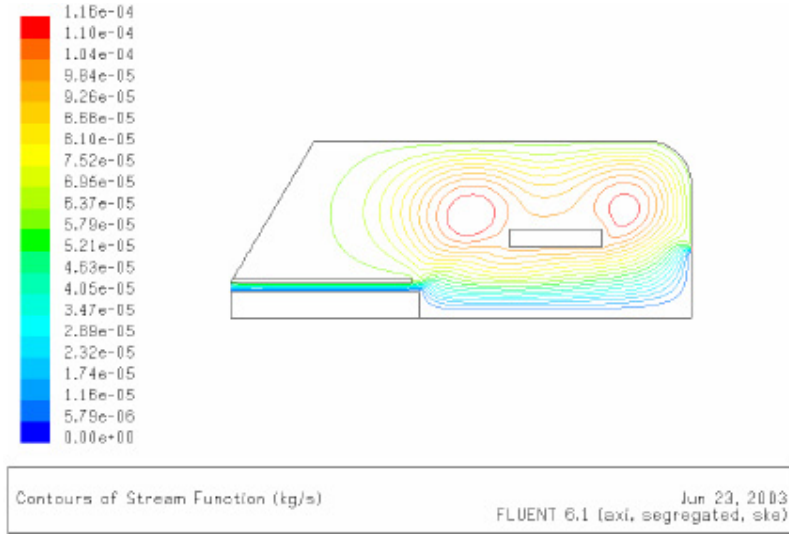

Figure 6.24: Computed streamline pattern for proposed anode geometry "B" in the PPM reactor. Arc is modeled as a symmetric source domain with 100 kW power. The secondary Recirculation pattern is stronger.

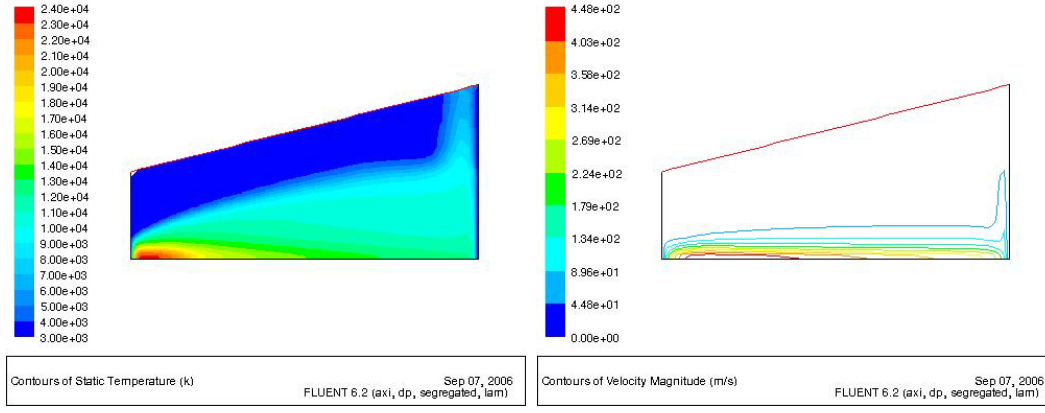

Figure 6.25: Computed temperature and velocity magnitude for a 10 cm 1 kA arc in pure Ar at 1 bar

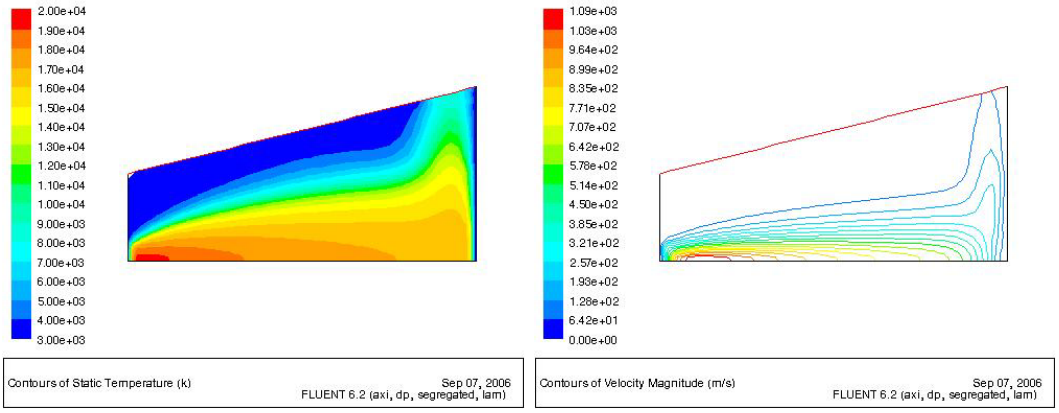

Figure 6.26: Computed temperature and velocity magnitude for a 10 cm 1 kA arc in pure He at 0.6 bar

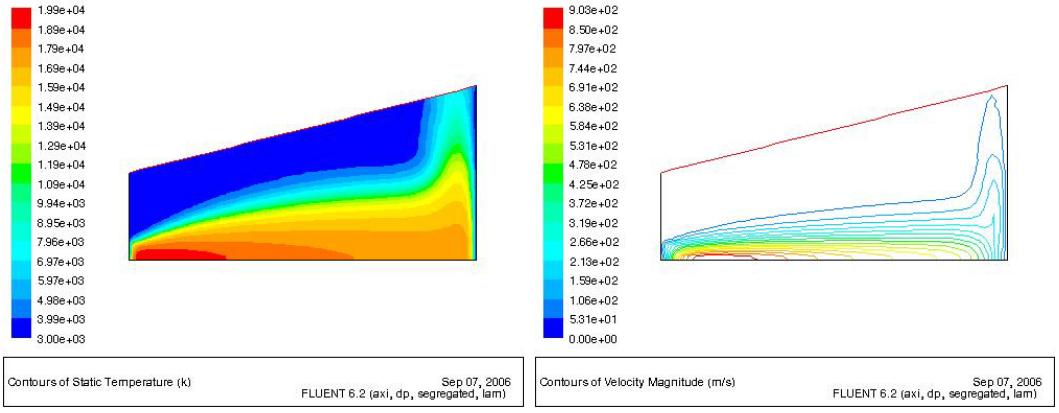

Figure 6.27: Computed temperature and velocity magnitude for a 10 cm 1 kA arc in pure He at 1 bar

6.5 3D SD model: prescribed current in a non-symmetric reactor

These cases demonstrate how the 3D version of the SD-II model[5] works. The current is prescribed in 3D, and the magnetic field is calculated from it. For simplicity, the current density is assumed symmetrical around a given axis, and the coordinate system in Fluent was rotated to match this. In principle any current distribution can be prescribed, but computing the corresponding magnetic field may take time. Even for a symmetric given current distribution, we clearly see 3D effects caused by the reactor geometry.

The cases in the simplified 3D PPM geometry may be regarded as boundary value cases for a very slowly rotating arc.

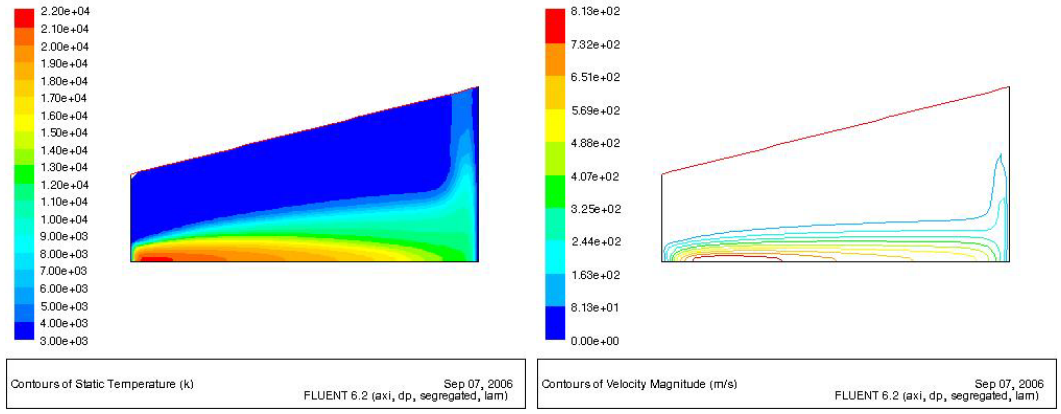

Figure 6.28: Computed temperature and velocity magnitude for a 10 cm 1 kA arc in He with 10% carbon vapour

[5]the SD-I model is trivial to expand to 3D and not shown here.

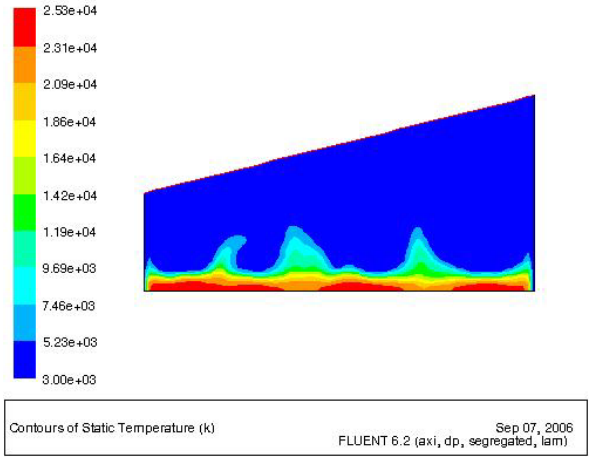

Figure 6.29: Typical non-converged computed temperature field for a 10 cm 1 kA arc in 50-50 He-C mixture. The hot spikes move around as the computation goes on. Attempts with pure carbon give similar results

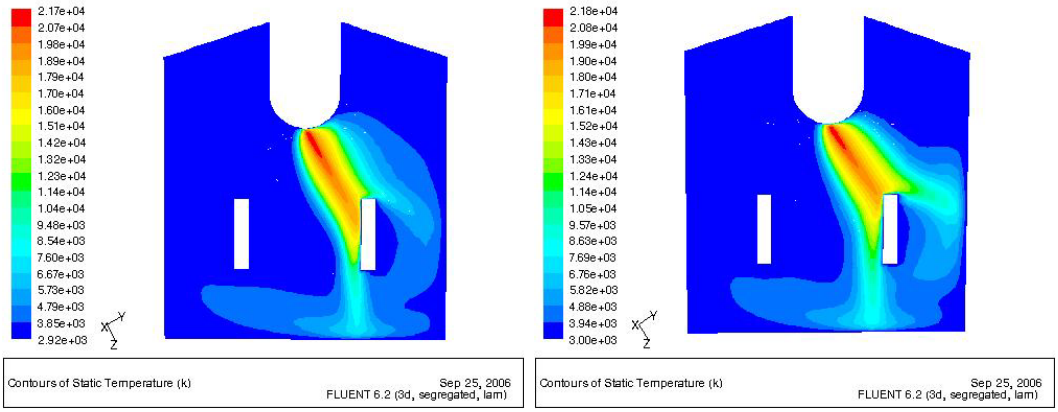

Figure 6.30: Temperature field for a prescribed straight burning 1 kA He arc. *Left:* the arc is assumed to burn at a 30 degree angle, hitting the anode below the top. *Right:* the arc is assumed to burn at a 35 degree angle, hitting the anode at the top corner

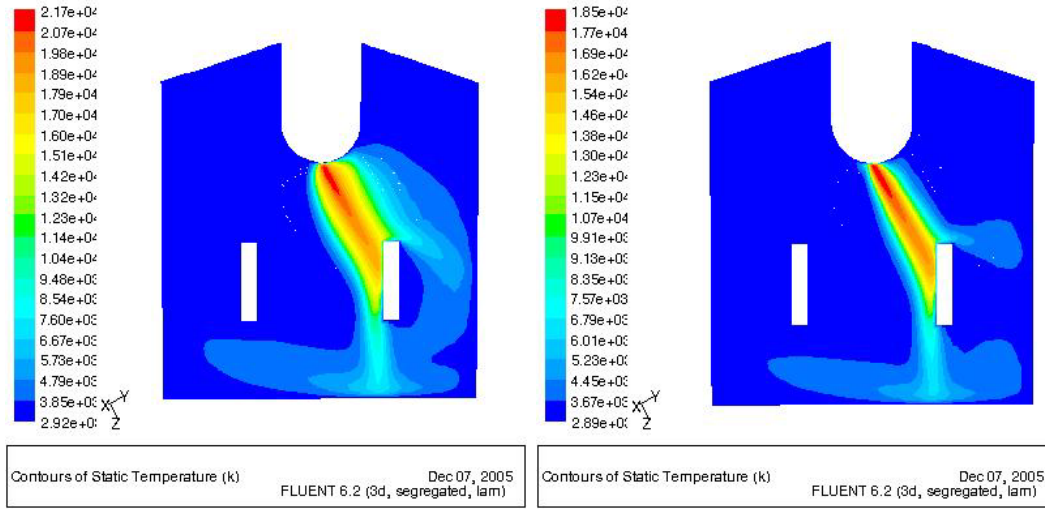

Figure 6.31: Temperature field for a prescribed straight burning He arc. The arc is assumed to burn at a 30 degree angle. *Left:* 1 kA arc in the simplified PPM geometry. *Right:* 4 kA arc in the geometry scaled up by a factor two

Chapter 7

Results: Deflected arcs

This chapter contains results from cases where the arc behaviour is affected by an outside influence. All cases in this chapters were solved with the 3D Vector Potential model described in chapter 4 using the transient solver.

Even though the cases with DC magnetic field and external gas flow *could* have been solved using the stationary solver, the transition from a free-burning state to the deflected one is interesting enough to treat them as transient problems. Of particular interest is the response time the arc needs to adjust to the new conditions.

All the results in this chapter use the same parabolic current distribution at the cathode (average current density of $1.27 \cdot 10^7$ A/m^2).

7.1 Arc deflected by external gas flow

The first real test for our 3D model is to let the arc be deflected by an external gas flow (from now on called gas flow, any reference to the cathode jet and associated gas flow will be labeled clearly to avoid confusion). This is the simplest 'deflection case' in the sense that the outside influence only comes into the boundary conditions and not into the MFD equations themselves.

Figures (7.1-7.2) show temperature profiles for a 1 kA Ar arc of nominal length 5 cm being deflected by a cold homogenous gas flow of 10 and 30 m/s respectively. The gas comes in from the left wall of a box-shaped domain and exits through the right, front and back walls. On the attached CD, the video file 'crossflow.mpeg' shows the transition to deflected state for a straight free-burning arc suddenly subjected to a gas flow of 30 m/s.

From figure (7.1) we can make two observations. One, that the angle of deflection

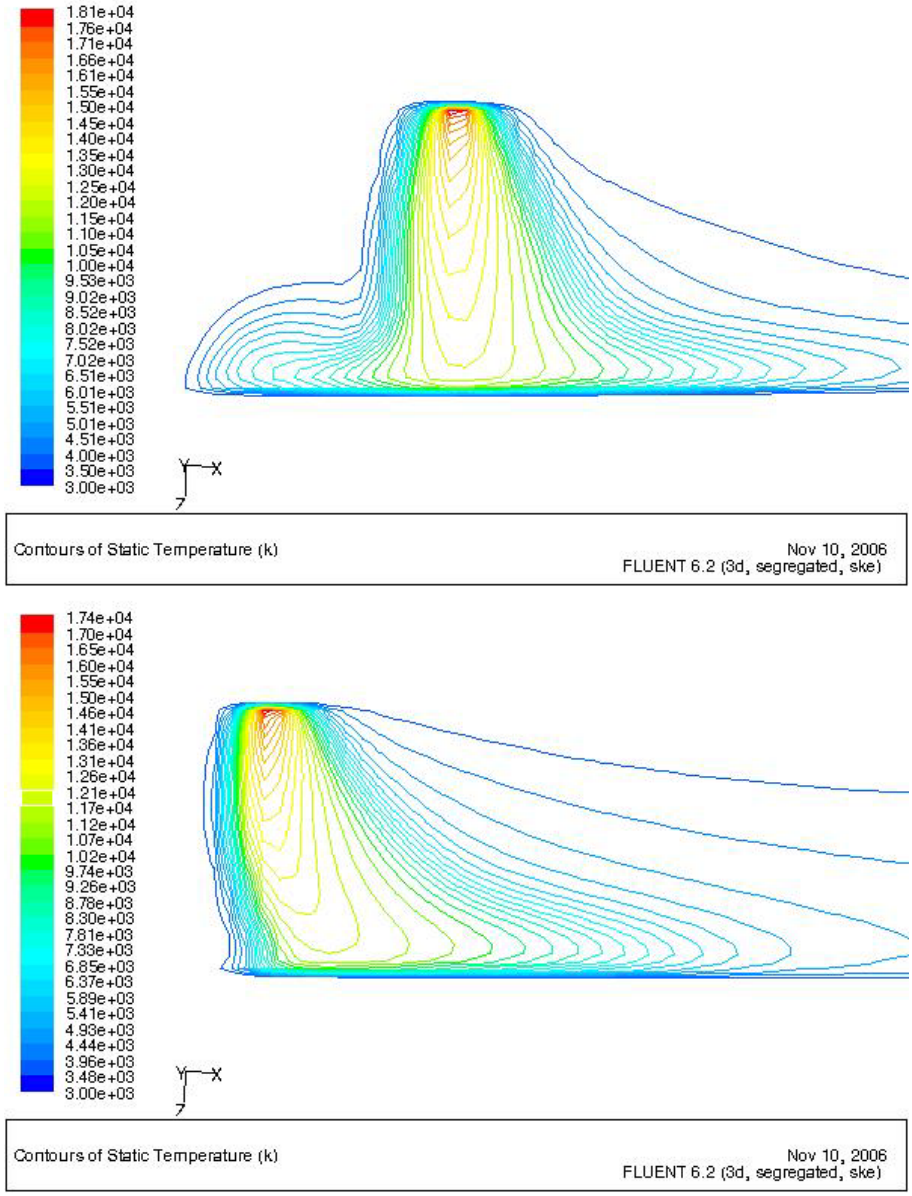

Figure 7.1: Temperature contours for a 5 cm 1 kA Ar arc deflected by a cold gas flow from the left. Vertical section through the center plane. *Top:* 10 m/s gas flow, *Bottom:* 30 m/s gas flow

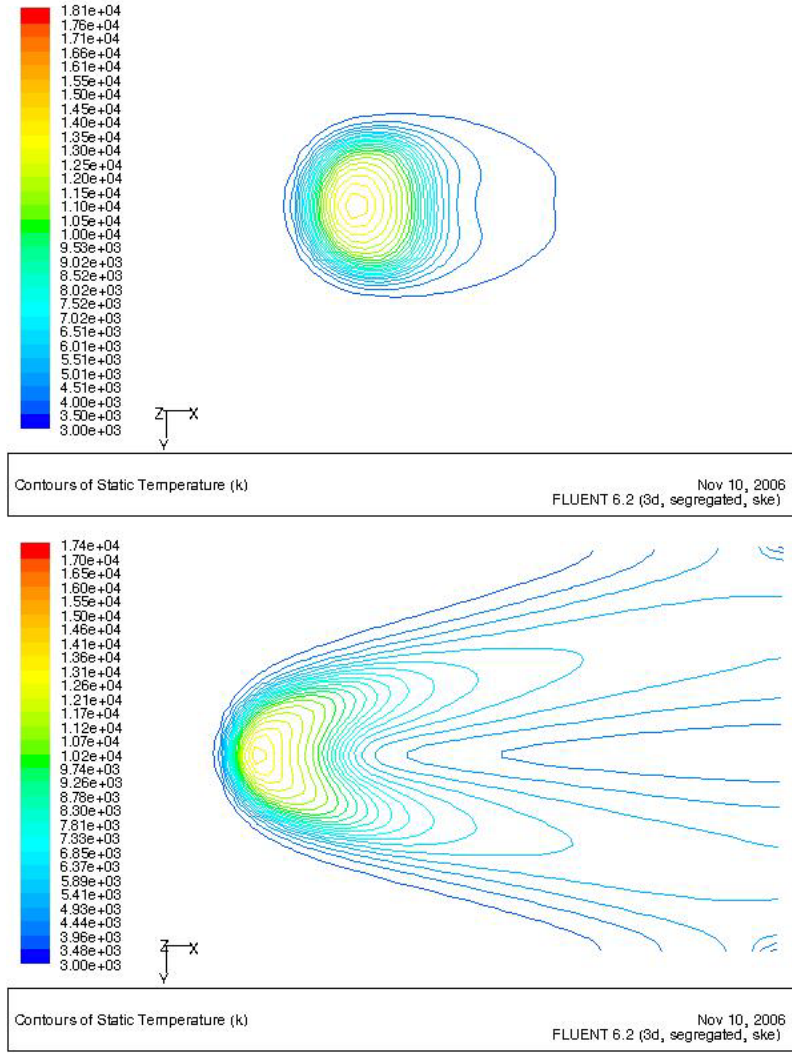

Figure 7.2: Temperature contours for a 5 cm 1 kA Ar arc deflected by cold gas flow from the left. Horizontal sections, 10 cm x 10 cm. *Top:* 10 m/s gas flow, section 3 cm below cathode. *Bottom:* 30 m/s gas flow, section 2 cm below cathode.

increases continuously from the cathode where it is (close to) zero. Two, that the deflection is more or less proportional to the wind velocity.

Using a simple *garden hose analogy* as illustrated in figure (7.3), one can imagine that hot gas is sprayed out by the cathode jet like water from a garden hose nozzle. Spraying water into perpendicular wind (case 'B') will result in the stream following a roughly[1] parabolic path. The deflection depends on the wind speed, but also on the velocity and mass density of the water jet. Likewise, if we assume that there are no forces except the cathode jet, we should expect an arc with roughly parabolic curvature, and with deflection dependent on wind speed, cathode jet and gas density.

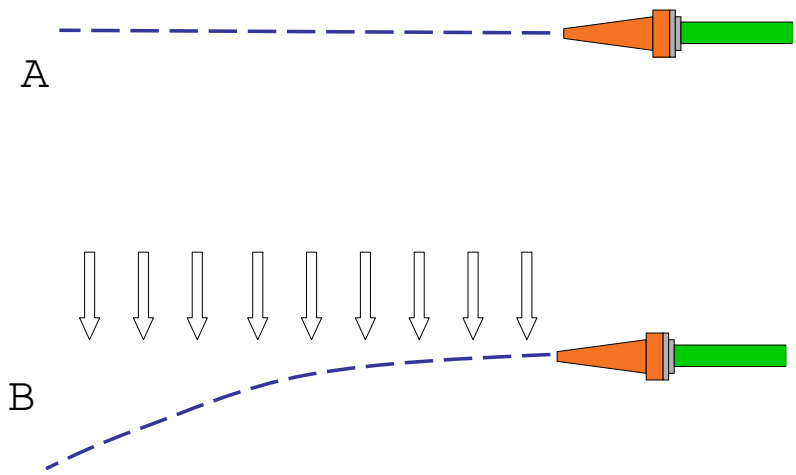

Figure 7.3: Illustration of the garden hose analogy. Case A is an undeflected water jet. Case B is a jet subject to a constant (drag) force, and follows a parabolic path. Case A is analog to a free burning arc, case B is analog to an arc in gas crossflow.

Several effects complicate this issue, such as the bending of the arc will give repulsive forces between the top and bottom of the arc, and the wind flow not being fully homogenous due to non-slip at the cathode and anode surfaces. Nevertheless, the results show a curvature very close to parabolic.

Figure (7.2) reveals an interesting phenomenon. Remember that the viscosity of

[1] only *roughly* a parabola because the drag coefficient will change as the stream expands or is blown apart. Similarly, the drag coefficient for the arc changes as it expands and is cooled.

the hot plasma gas is much higher than for the cool gas being pushed around it, so that the situation becomes a bit like gas flow around a (very soft and deformable) cylinder. As long as the drag is not too strong (top picture), the main change to the cross-section of the arc is that the extra cooling on the upstream side makes for an even steeper temperature gradient there. But when the wind becomes stronger (bottom picture), the high skin friction drag draws the arc with it on the sides. The fast gas streaming around the arc creates a wake on the downstream side that is filled by cold gas. The total effect is that the arc assumes a more or less 'half-moon' shape with a cold area directly behind the arc flanked by two hot edges. Between the 'elliptic' and 'half-moon' shapes shown in the figure, there is an intermediate situation where the arc cross-section attains an intermediate shape slightly resembling a tropical fish. These phenomena are related to the shapes of rising bubbles.

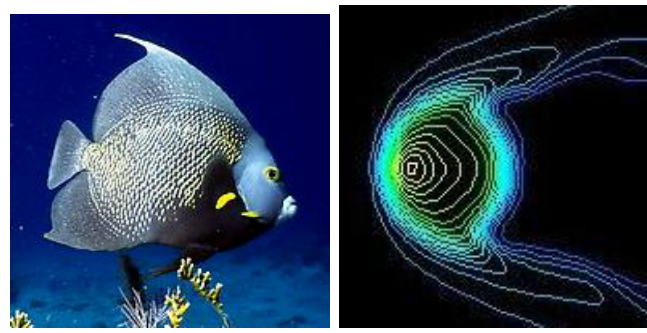

Figure 7.4: The 'fishy' intermediate shape of an arc in crossflow.

In all cases, the flattening and extra cooling of the arc gives an increased voltage. Obviously, turbulent effects are important for the high wind cases. Investigating the arc cross-section deformation with an advanced turbulence model (Large Eddy Simulations or equivalent) would perhaps give interesting information.

7.2 Arc deflected by perpendicular magnetic field

In these series, the arc is linearly deflected in y-direction by an homogenous external magnetic field in x-direction. The external magnetic field was modeled directly into the Lorentz force term. This was discussed in section 4.5, but is crucial enough to repeat.

Because of the superposition principle and how the equations are coupled, we can effectively solve the electromagnetic equations for the field $\vec{B}_0 = \vec{B}_{tot} - \vec{B}_{ext}$, where $\vec{B}_{tot}$ is the total (real) field and $\vec{B}_{ext}$ the externally applied component. The point is that the external component is imposed, i.e. determined *only* by the magnet coil

geometry and current, and is *curl-free* in the whole domain[2] and can thus be removed from the Maxwell equation:

$$\nabla \times \vec{B}_{tot} = \nabla \times (\vec{B}_0 + \vec{B}_{ext}) = \mu_0 \vec{j} \Leftrightarrow \nabla \times \vec{B}_0 = \mu_0 \vec{j}$$

The computed $\vec{B}_0$ field has the same boundary conditions as a free-burning arc. The corresponding $\vec{A}_0$ field must then also have the same boundary conditions as for the free-burning arc, saving us a lot of work.

The A_0 field is naturally affected by the external field, but *only indirectly, through the extra force giving a different current distribution.* We can further safely assume that the currents in the external coils are constant and independent of the movement of the arc.
The solver procedure is then:
• Solve for Φ and $\vec{j}$ from the previously computed temperature field and electric conductivity.
• Solve the $\vec{A_0}$ equation for the obtained $\vec{j}$ and boundary conditions for a free burning arc. (The effects of the external field are indirectly included in $\vec{j}$).
• Compute $\vec{B}_0$ from $\vec{A_0}$, find $\vec{B}_{tot} = \vec{B}_0 + \vec{B}_{ext}$.
• Compute electromagnetic forces from $\vec{B}_{tot}$ and $\vec{j}$ and ohmic heating from $\vec{j}$
• Solve the Navier-Stokes equations to obtain the new velocity and temperature fields.

Simulations were done with DC fields and normal sinusoidal AC fields. Using the transient solver and a DC field effectively solves for a step signal and can determine the response time of an arc to external influences. However, there is not enough reliable data to analyse this since most cases were solved from existing deflected solutions rather than from the axisymmetric one.

7.2.1 DC magnetic field

For these cases, the external magnetic field is homogenous and stationary. The cases were solved transiently, starting from the converged result for a free burning arc or from an arc in a weaker field. Figures (7.6-7.8) show fully deflected 1 kA Ar arcs of nominal length 5 cm in magnetic field strengths 0.5 mT, 1 mT and 2 mT. These magnet field strengths are comparable to the magnetic field generated from the arc itself: 1 kA distributed inside a 2 cm radius gives $B_\theta = \mu_0 I/2\pi r \approx 10$ mT. DC fields around 1 mT should then be expected to give a visible deflection without completely distorting the arc.

[2]The curl of any B_{ext} is only non-zero inside the magnet coils that generate it, which are not part of our domain. This is true also for a non-homogenous time-dependent external magnetic field.

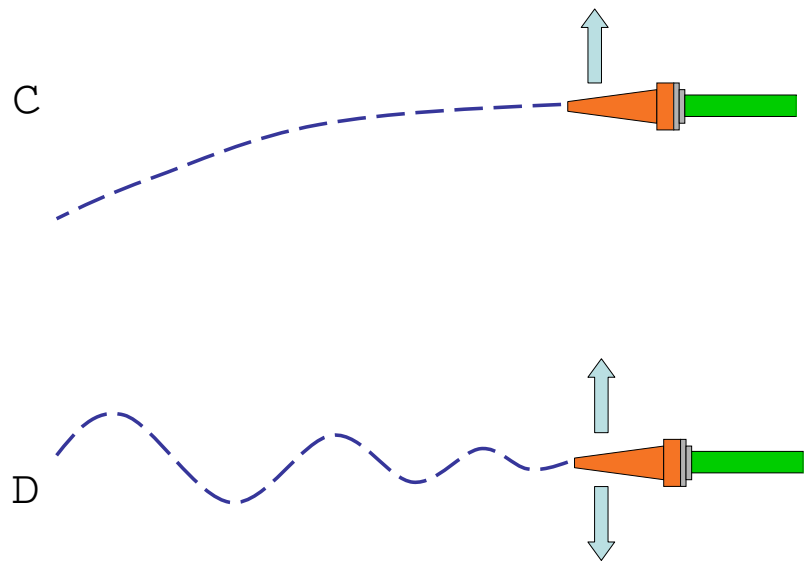

Figure 7.5: Continuation of the garden hose analogy - now applied to magnetic deflection. In case *C* the hose is moved constantly, the effect is the same as in case *B*. In case *D*, the hose is moved periodically back and forth: the resulting jet resembles a propagating wave. Case *C* is analog to an arc in a perpendicular DC magnetic field, case *D* is analog to one in an AC magnetic field

Like for the gas flow deflection cases, we can use the garden hose analogy (fig 7.5). The homogenous magnetic field and the preserved arc current gives the same deflecting force for all sections of the arc, but the direction of the force changes as the arc curves. For small deflections, the theoretical shape of the arc is that the centerline follows a parabola[3], as is confirmed by the results. For larger deflections, the theoretical shape should be more curved than a parabola (ultimately an ellipse) but in practice such an arc would be unstable or even extinct as the voltage would be too high (imagine the garden hose in a hurricane!).

7.2.2 AC magnetic field

These cases were solved similar to the DC cases above, with the only change being that the magnetic field component added to every cell was a function of solver time. It is crucial in these cases to select a relevant time step for the computation as there are two time scales involved: the time scale of the applied AC field and the

[3]the body of the arc has a nice parabola-like curvature, but the picture is distorted when the jet hits the anode wall.

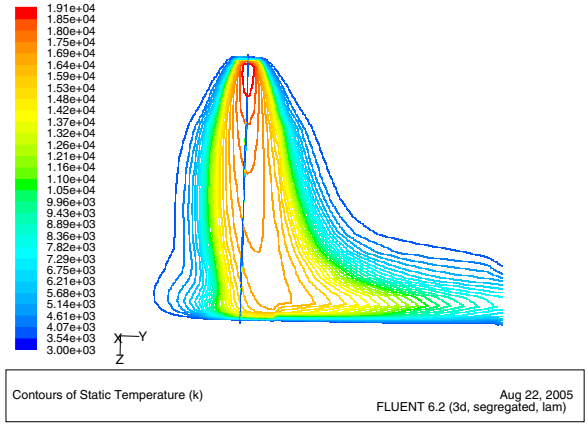

Figure 7.6: Temperature profile for a 5 cm 1 kA Ar arc being deflected by a perpendicular constant homogenous 0.5 mT DC magnetic field.

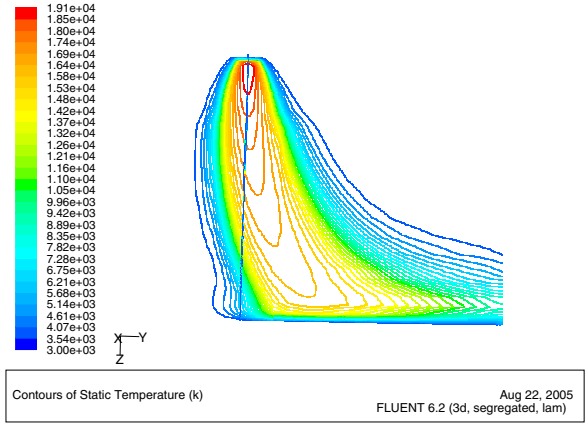

Figure 7.7: Temperature profile for a 5 cm 1 kA Ar arc being deflected by a perpendicular constant homogenous 1 mT DC magnetic field.

arc response time[4] that depends on arc length, current and type of plasma gas. As discussed later, the important number is $\omega z/v$, the ratio of the time that the plasma needs to move from cathode to anode divided by the time constant for the AC field.

[4]there is also a 'numerical system response' time scale given by the Courant criterion. This can be computed automatically, but in this work a constant time step was found to be more stable

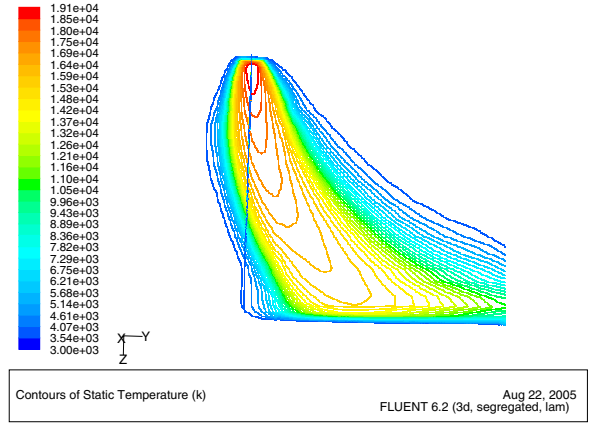

Figure 7.8: Temperature profile for a 5 cm 1 kA Ar arc being deflected by a perpendicular constant homogenous 2 mT DC magnetic field.

For AC frequencies much slower than the arc response time ($\omega z/v << 1$), the arc is at all times fully adjusted to the applied magnetic field. The arc then should have a parabola-like curvature with the total deflection proportional to the applied magnetic field.

For high frequencies ($\omega z/v \approx 1$), the response time of the arc system is comparable to the frequency of the magnetic field. Since the arc is fixed at the cathode and free at the anode, it must respond from the top and down. The bottom part of the arc, which also has to travel a greater distance, gets a much longer response time than the top part of the arc. The bottom of the arc will then lag behind and the arc curvature will assume a 'S-shape' if the AC field is just above the critical frequency. At even higher frequencies the bottom will lag more than a full period behind and the arc curvature will get a sinusoidal shape.

Figure (7.9) shows snapshots of a 5 cm 1 kA Ar arc in a 200 Hz AC field. Figure (7.10) shows snapshots of a 20 cm 1 kA Ar arc in a 50 Hz AC field. The animations for these figures are included in *ac1.mpeg* and *ac2.mpeg* on the CD.

Figure (7.11) shows snapshots of the 10 cm 1 kA Ar arc in a 200 Hz field. The corresponding animation[5] is included in *ac3.mpeg* on the CD.

[5]this animation was dubbed 'the belly dancer' because of its 'sensual moves'.

For very high frequencies ($\omega z/v >> 1$), the oscillation of the magnetic field is faster than the arc can respond and the arc will hardly move at all, just 'shake' a little bit[6].

7.2.3 Comparison with experiment

Some experimental work has been done on arc deflection, and the investigations by Zweben and Karasik [61][37] at Princeton are well suited for comparison. In their work, they photographed arcs of about 10 cm and 250 A burning in air.

Using an approach similar to the water-hose analogy, they assumed the arc to be a channel with constant radius, flow velocity and density, similar to a conducting wire.

For DC fields they observed a good match between the parabolic curvature predicted by the 'wire model' and the observed one. For AC fields they observed the growing sinusoidal shape and how the amplitude of oscillation decreases with increasing frequency. Their results matched the arc shapes predicted from the 'wire model', given by the equation

$$x(z,t) = \frac{I_0 B_y}{m\omega^2}\left[\cos(\omega t - \omega\frac{z}{v}) - \cos(\omega t) - \frac{z\omega}{v}\sin(\omega t - \omega\frac{z}{v})\right] \qquad (7.1)$$

The computed results in this work show the same qualitative behaviour: the arc has a parabolic curvature for DC or low-frequency AC fields, but transforms into a sinusoidal shape (with smaller amplitude) around the critical frequency $\omega = v/z$.

The typical magnetic fields in this work are much weaker than those used in [61]. The arc currents are higher and the gas density for Ar a bit higher. These factors all combine in the first scaling term in equation 7.1 and do not affect the transit from parabolic to sinusoidal. However, velocities are different for our system due to the difference in current and gas. According to [61], the governing parameter for the arc shape is $\omega z/v$, i.e. the ratio of time needed for the plasma gas to travel between the electrodes versus the timescale for changes in magnetic field.

As discussed in [61], the average computed (from curve fitting) velocities for the sinusoidally deformed arcs were *about a factor ten lower* than the computed maximum velocity at the cathode spot. Our 20 cm 1 kA arc has a maximum velocity of about 400 m/s, but the velocity at the edge of the arc is significantly lower. Also, one would assume that each curve of the arc reduces the speed, meaning that the

[6] there is another system dependent "critical frequency" where the arc displacement is the same scale as the grid size. If the arc is displaced less than one cell, the deflection is invisible in the simulations. Refining the grid might then reveal higher frequency oscillations.

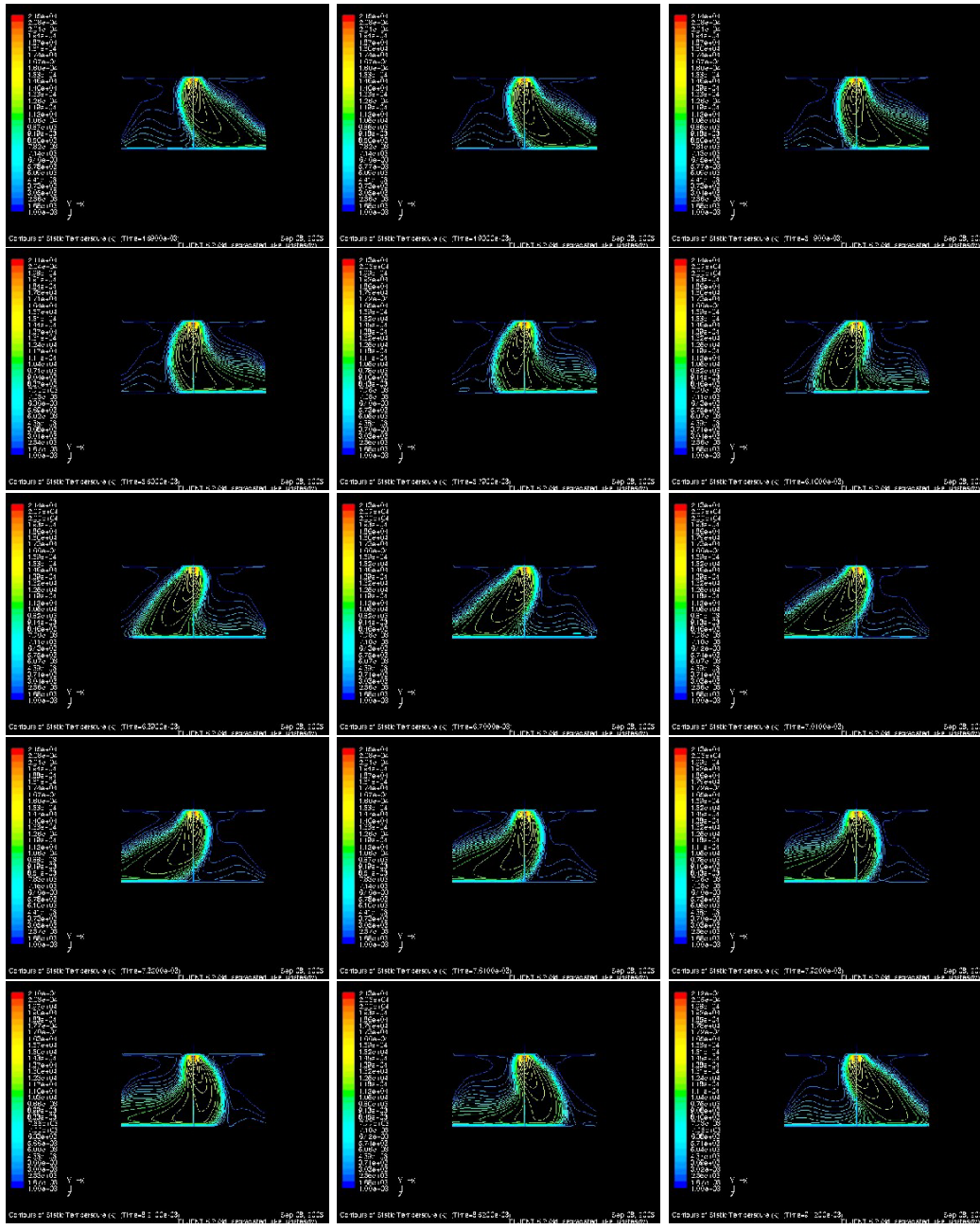

Figure 7.9: Snapshots of temperature contours for a 5 cm 1 kA Ar arc being subjected to a AC magnetic field of 200 Hz. For this frequency, we can see deviation from the parabolic shape, and that the anode end of the arc is lagging behind the top. The time difference between first and last frame is 5 ms, matching the 200 Hz AC frequency.

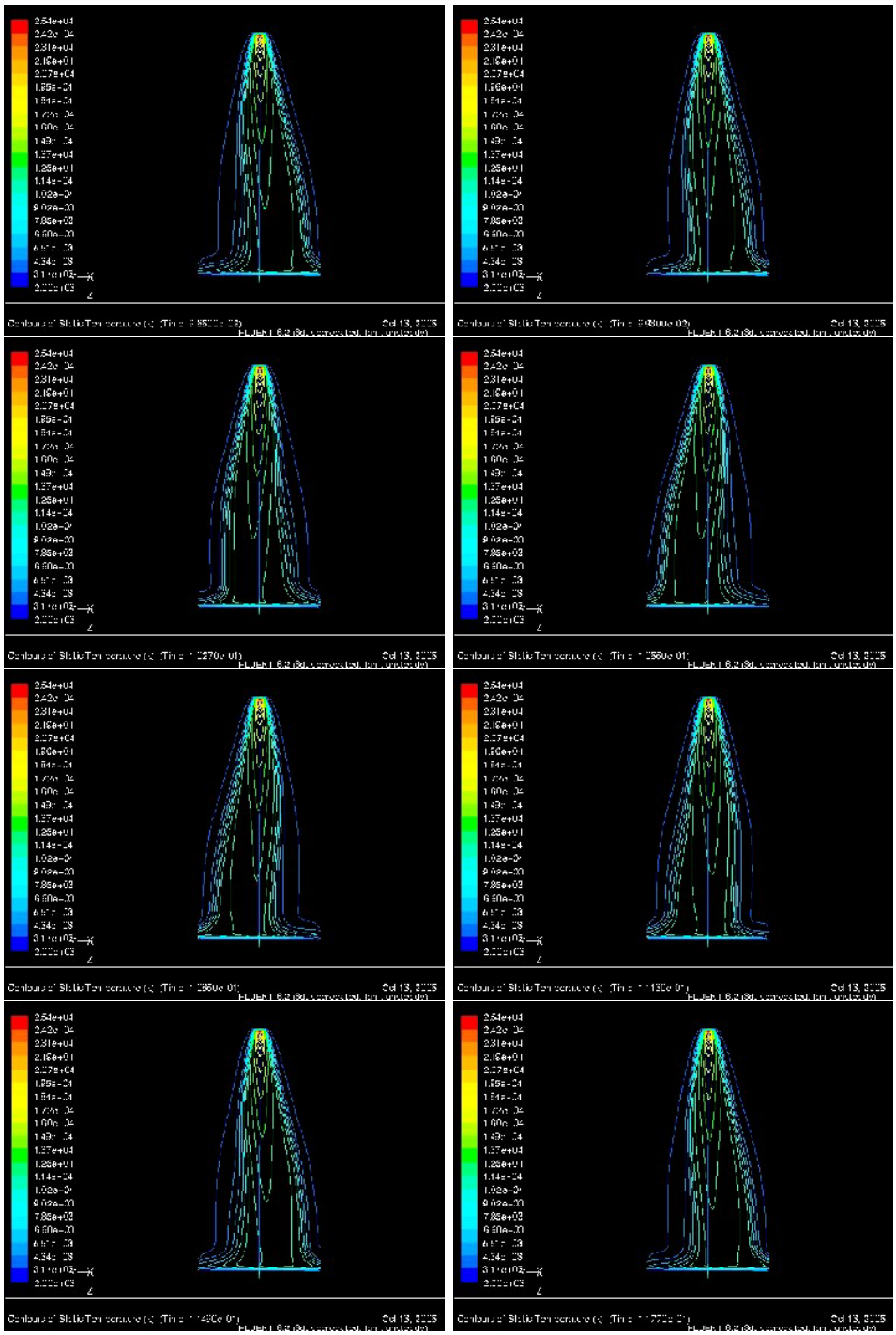

Figure 7.10: Snapshots of temperature contours for a 20 cm 1 kA Ar arc being subjected to a AC magnetic field of 50 Hz. The deviation from parabolic shape is similar to figure 7.9, except the amplitude of the AC field is much smaller here. The time difference between first and last frame is 20 ms, matching the AC frequency.

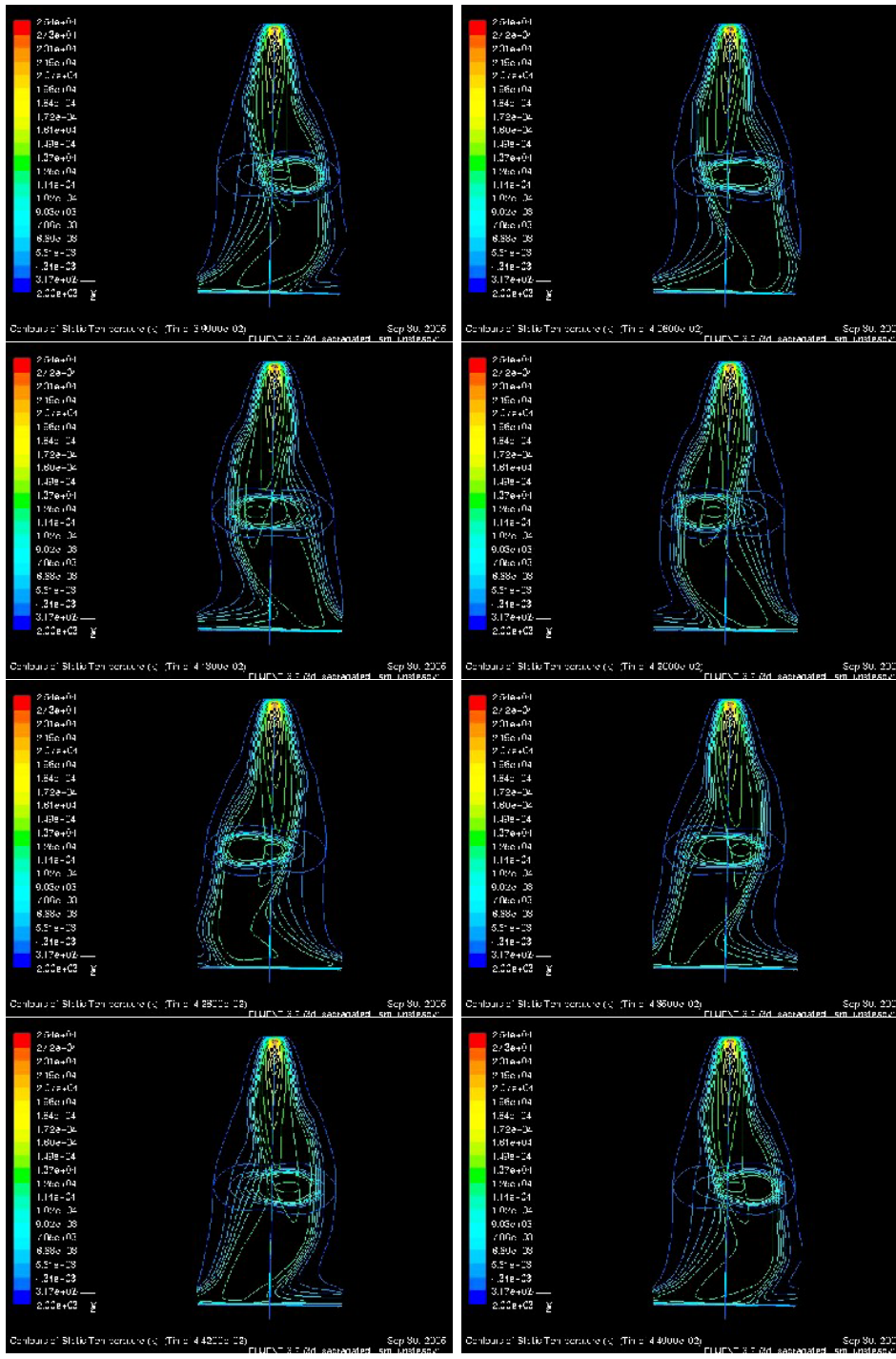

Figure 7.11: Snapshots of temperature contours for a 20 cm 1 kA Ar arc being subjected to a AC magnetic field of 200 Hz. The phase lag between the top and bottom of the arc is about a full period, giving a sinusoidal arc shape. Temperature contours are shown both in a vertical and a horisontal plane. The time difference between first and last frame is 5 ms, matching the AC frequency.

sinusoidal arcs have a lower average velocity than straight ones. *If the factor ten* is a reasonable guideline, we can assume an average arc velocity of 40 m/s giving a transit time of 5 ms for the plasma jet. For a 200 Hz AC field, we should then expect the bottom of the arc to lag a full period (5 ms) behind the top of the arc - which is *remarkably close to what we see* in figure (7.11). For a 50 Hz field on the 20 cm arc we should expect the same phase lag as for a 200 Hz field on a 5 cm arc if the characteristic velocities are the same. Again, this is what we observe.

The conclusion is that the results presented here are consistent with the experimental observations made by Zweben/Karasik. The mysterious factor 10 between the computed maximum velocity and the characteristic velocity used in the equation is only partially explained. But it is interesting that the same factor gives a good match both when curve-fitting experimental data and when analysing simulation from the VP model that does not make any of the coarse assumptions of the 'wire model'.

7.2.4 Application: Arc control and voluminous plasmas

The main motivation for doing simulations of arcs in external magnetic fields was to test the model. However, there are also interesting practical applications.

DC field deflection is mostly an unwanted problem in industrial arc furnaces for steel making: typically the bus bars and cables connecting the power supply to the electrodes run on one side of the furnace, and the high current gives a strong deflecting force on the arc. This effect was modeled for instance in [6], and gives non-symmetric conditions in the furnace. Understanding and modeling the problem is a key to solving or circumventing it, and by clever buswork geometry or even an extra external magnetic field, the arc can be forced back to the wanted position.

AC field deflection is a different matter: Moving the arc around in a controlled manner distributes the heating effect over a larger gas volume, generating a voluminous plasma. By controlling the AC magnetic field amplitude, the size of the heating zone can be controlled. By controlling the frequency, we control the amplitude of the temperature oscillations while retaining the same average heating and temperature, as illustrated in figure (7.12). Temperature oscillations are of course present in the gas as well as on the anode and other surrounding surfaces. Just remember that a high AC frequency will reduce the amplitude of the deflection as discussed in the previous section.

For the PPM project, a larger plasma zone means that the carbon feedstock can be

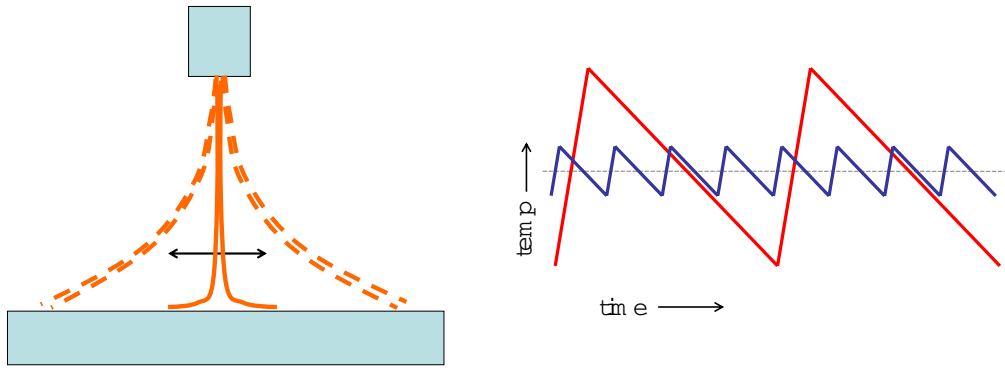

Figure 7.12: Illustration of AC magnetic field control of plasma heating. *Left*: The amplitude of the AC field controls the amplitude of the arc deflection, making the arc sweep through a larger or smaller volume. *Right*: Rough illustration of the temperature-time-dependency for a point heated periodically by an arc sweeping over it. For the high frequency, the temperature oscillations are much smaller than for the low frequency.

vapourised or decomposed[7] in a larger part of the reactor. Other uses of AC magnetic field deflection include moving the cathode or anode spots around to reduce the thermal strain on the electrodes and thus reduce electrode erosion. As suggested in [56], ladle reheating in steel production is another application for a plasma torch in an AC field. A similar effect might be obtained mechanically by mounting the plasma torch on a moving arm, but using an AC field is simpler, cheaper and allows much higher frequencies.

7.2.5 Application: Controlled rotation

This novel setup includes two sets of magnet coils generating (homogenous) fields in both x and y directions, as illustrated in figure (7.13). By giving the AC currents a 90 degree phase difference, the result is a field of constant (and homogenous) strength, but a direction vector that rotates with the AC frequency. A DC arc subject to this rotating field will be displaced in the r-direction according to the field strength, while the direction of the displacement changes, moving the anode spot in a circular path. The radius of the circle is given by the field amplitude, and the rotation frequency *is equal to the AC frequency*. This arc rotation concept can be compared to a two-phase *synchronous motor* with the rotating arc playing the part of an externally magnetised rotor.

[7] typical feedstock is carbon black or methane gas. The black must be vapourised while methane decomposes $CH_4 \rightarrow C + 2H_2$

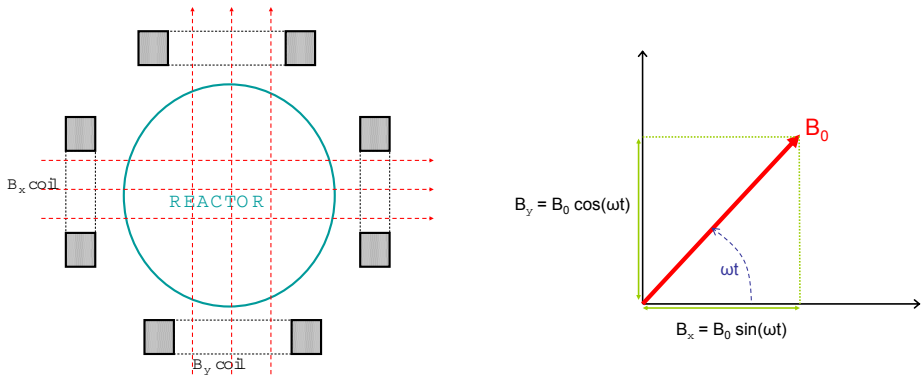

Figure 7.13: Illustration of the two-phase rotating field concept for controlled rotation. Two perpendicular sets of coils generate a sinusoidal AC field each, but with 90 degrees phase displacement. The figures illustrate the first half of a period. An arc in this field will be subject to a displacing force proportional to the field strength. As the direction of the force changes, the direction of the arc displacement changes, *rotating the arc with the frequency given by the AC field.*

Technically, a three-phase setup would be simpler and more economical than the two-phase one, and more attractive for upscaled industrial reactors. The concept can easily be scaled up to any multi-phase setup and for higher frequencies than the mains frequency. However, the two-phase magnetic field can easily be designed to give a homogenous magnetic field direction and strength in the whole arc domain, and is well suited for and numerical modeling. A two-phase coil current (with 90° phase difference) is readily available by using two transformers in a Scott-T connection which transforms three-phase to two-phase (see appendix C).

Let us compare the two-phase setup to the standard rotating arc setup with a (homogenous) axial constant magnetic field (see chapter 8). There are two main advantages of the two-phase setup. First, the two-phase setup allows the frequency of the rotation to be controlled directly and independently of the rotating force: the deflection is the same no matter how low the frequency is set. *For low frequencies this enables us to have full control of the rotation.* If the AC frequency is too high, the lower part of the arc cannot move fast enough (due to fluid dynamic drag) and will lag behind, giving something more like the familiar 'corkscrew' shape. What frequencies are 'high' and 'low' are as yet unknown, but a rough guideline is the critical frequency $\omega = v/z$ for AC deflection.

The second advantage of the rotating magnetic field setup is that the force is much more homogenous along the arc. For the axial field setup, the lower part of the arc

has a larger radial current component and thus gets a larger rotating force. As shown in section 8.2, at high rotation speeds this difference in force rips the arc apart, or at least gives extra deformation.

For the two-phase setup the tangential force depends on the phase lag, and will be largest on the part of the arc that is lagging 90 degrees behind. On a part of the arc lagging 180 degrees behind, the force would be in negative r-direction, reducing the radius and thereby enabling this part of the arc to move faster azimuthally and thus catch up. The result is that the we should never have dramatic and chaotic changes in arc length, and the voltage should thus fluctuate less during rotation.

Without some simulation work on this phenomenon, it is hard to speculate how the arc will respond to very high frequencies - most likely it will attain some sort of helical shape with a smaller radius than the same AC amplitude would give for lower frequencies. In a hollow anode like in the PPM project, the two-phase rotated arc could probably become metastable or chaotic at some frequency when the natural radius of the rotating arc becomes smaller than the anode radius. But even then the arc would not burn outside the anode and the voltage would be expected to be lower than for a chaotically burning arc in the axial magnetic field setup.

This should be investigated as a natural continuation of this work.

7.3 Periodic or unstable behaviour caused by geometry

These series solve simple cases that display very interesting behaviour: arc instabilities or periodic behaviour caused by the geometry of the system. Naturally, arc current and choice of plasma gas also determine whether a given arc is stable or unstable, the point is that geometry effects give a dynamic (periodic or quasi-periodic) behaviour without any imposed time-dependency in the system or boundary conditions. This type of behaviour is seen in gliding arcs[25], but also in transferred as well as non-transferred arc plasma torches.

7.3.1 Extinction and restrike

The basic concept is that for certain geometries, the cathode jet itself may blow the anode spot out of position, increasing the arc voltage as the arc grows longer. Eventually the arc dies and restrikes at (or near) the original cathode spot. The concept is illustrated in figure (7.14), a typical computed voltage function is shown in figure (7.15), and figure (7.16) shows various results for simple systems with this type of behaviour. Animations are included in *restrike1.mpeg*.

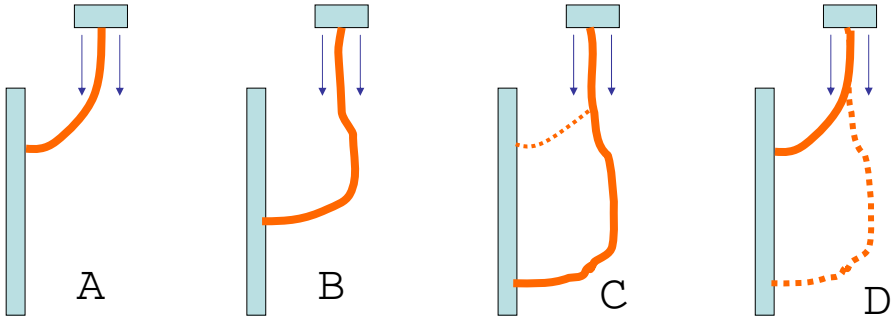

Figure 7.14: Concept of *restrike*. The arc burns from the cathode to a large anode. The cathode jet pushes the hot plasma along the anode until the arc voltage drop becomes too high and the arc restrikes at a closer point.

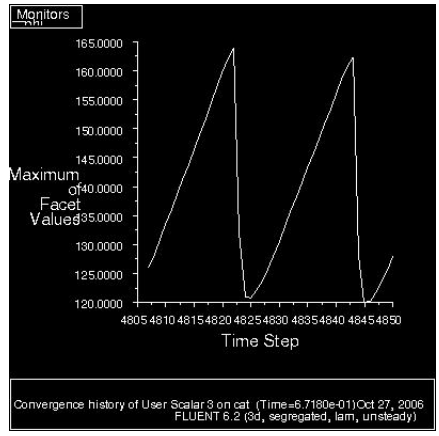

Figure 7.15: Computed arc voltage as function of time for two periods of the periodic restrike behaviour. Voltage varies between 120 and 165 V. One period is 1 ms long

7.3.2 Periodic take-over

To understand this phenomenon, one must remember that the current at the highly conductive anode must be normal to the surface. An arc burning almost parallel to the anode surface must bend itself into position. If the current is high[8], the arc cannot take a sharp turn but needs some space to bend. For narrow cylindrical or parallel anodes, the bending of the arc may move the arc close the opposite anode

[8]high current gives high velocities, and also stronger magnetic forces trying to straighten the arc

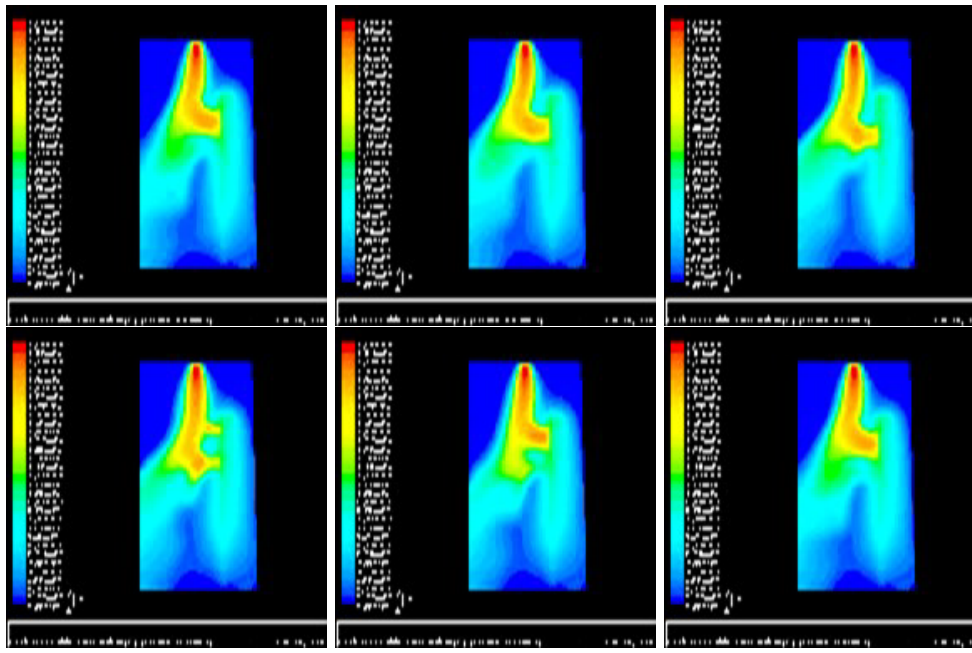

Figure 7.16: Computationally observed restrike. The behaviour in this case was perfectly periodic at about 1 kHz; the first and last snapshots look identical.

surface and eventually short-circuiting itself. As the arc tries to stabilise in the new position, the situation repeats itself (usually with the anode spot being blown downwards like in the extinction cases).

Figure (7.17) illustrates the concept, and figures (7.18) shows a simple system with this behaviour. The corresponding animation is *takeover.mpeg*.

7.3.3 Comparison with other work

Trelles, Heberlein and Pfender [54][55] have modeled[9] flow instabilities in DC plasma torches. From experiments and modeling they report three different modes of arc operation, depending on current and gas inflow: a steady (more or less stationary) burning mode, a periodic takeover mode, and a quasi-periodic chaotic restrike mode. Which mode is obtained depends on the amount of gas blown through the torch, as well as the geometry and arc current.

The cases presented in this chapter have simpler geometry as well as a model that

[9] their model includes two-temperature equations and sub-grid scale FEM modeling.

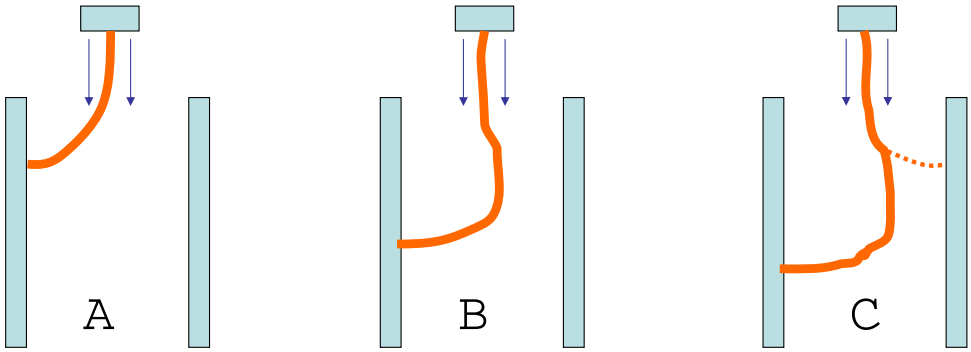

Figure 7.17: Concept of *periodic take-over*. Similar to the restrike mechanism illustrated in 7.14, but here the bending of the arc means that the new arc will burn to the opposite side of the old one.

deals very primitively with the non-LTE area near the anode. Still, the same three arc modes were observed, indicating that our Magnetic Vector Potential model can simulate the real behaviour of complicated systems.

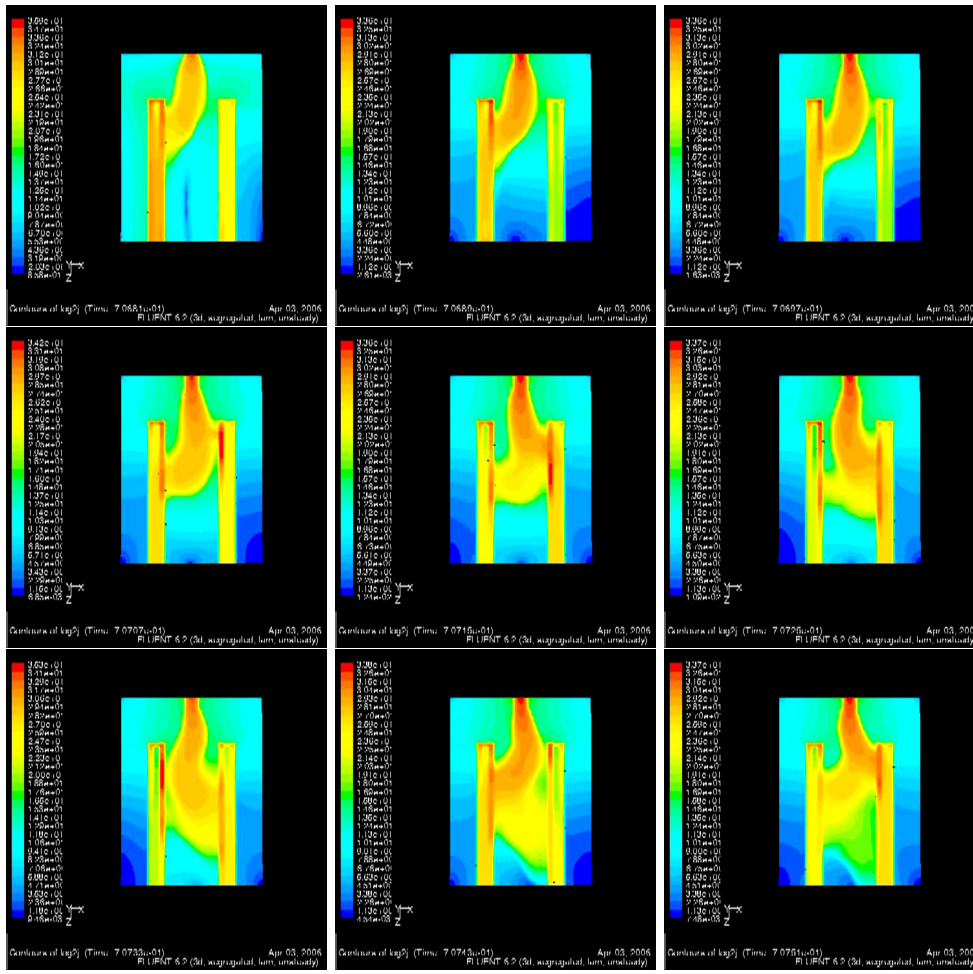

Figure 7.18: Computationally observed take-over behaviour. The right conductor was changed from floating potential to an anode at the start of the series. The snapshots show the two initial take-overs, after this the whole system changes periodically with a period of about 0.7 ms.

Chapter 8

Results: Rotating arcs

This chapter contains some results from cases where the arc is rotated by a homogenous axial magnetic field. The cases were solved with the 3D Vector Potential model described in chapter 4 using the transient solver.

Both argon and helium arcs have been simulated, with magnetic flux densities ranging from 1 mT to 40 mT. All cases use the same parabolic cathode spot current distribution as the cases in the preceding chapter, with a total current of 1 kA and an average current density of $1.27 \cdot 10^7$ A/m^2.

Rotating arcs are difficult to do calculations on. If starting from an axisymmetric free burning arc, the rotating force will tend to just twist the arc around itself rather than start a real rotating movement. If starting from some non-symmetric initial value, the initial movement may be very erratic and finding the stable movement may be very difficult. Of particular importance were the geometry and boundary conditions near the anode.

8.0.4 Anode modeling

In order to emulate the real PPM reactor geometry, the anode is modeled as a hollow cylinder of highly electrically conductive material. The current can only exit the domain through the bottom of the cylinder. To keep the domain as small as possible, the outer walls of the domain was assumed to be pressure outlets rather than solid walls. The bottom wall on the inside of the anode could not be modeled as a wall either, as hot gas then would be trapped inside the anode and give it a unrealistically high temperature. Modeling the surface as a pressure outlet created a different unphysical situation: unrealistically high backwash of cold (set temperature) gas through parts of the bottom wall distorting the picture.

The solution was, like in the real PPM reactor, to make a taller anode that en-

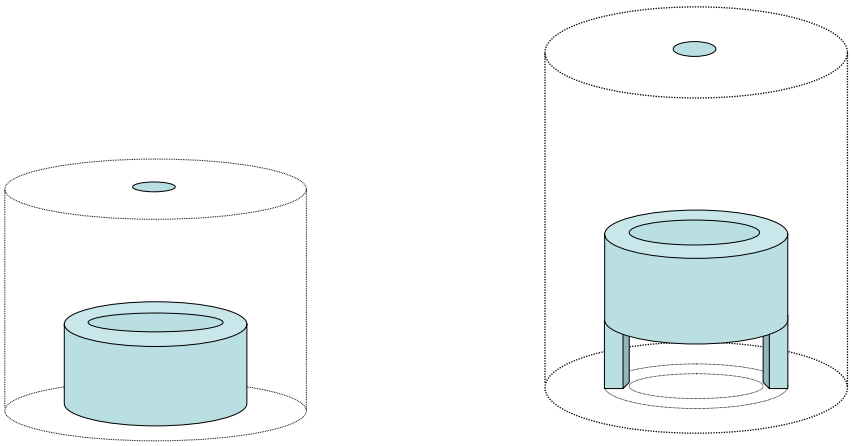

Figure 8.1: *Left:* The initial geometry. Cathode spot and the conducting hollow anode shown. The bottom inside of the anode gave problems whether modeled as a wall or as a pressure outlet. *Right:* The final geometry. The anode cylinder is mounted on legs conducting the current out of the domain while enabling gas to flow between them.

abled the gas jet to flow through it. For simplicity, the anode in the simulations was modeled as a cylinder mounted on two conducting 'legs'. The current then can only exit through the bottom of these legs. Figure (8.1) illustrates the initial and final geometries used for simulating the rotating arcs.

8.0.5 Why plot the logarithmic current density?

The choice of plotting current density rather than temperature (see figure 8.2) was made for several reasons. The current distribution is the parameter that determines everything else. Seeing how the current distribution (i.e. the electric arc) is influenced by the rotation is then fundamentally more interesting than looking at the temperature field. If we can control the current, we control the heating. Also, from a modeling perspective, the current distribution is the critical parameter to watch for unstable or unphysical behaviour. The choice of plotting the current density logarithmic is natural as the current density varies with four to six orders of magnitude in the system.

The temperature distribution tells us whether we have achieved a voluminous plasma or not. For stable rotation, the temperature will typically be quite high (5-6000 K) inside most of the anode cylinder.

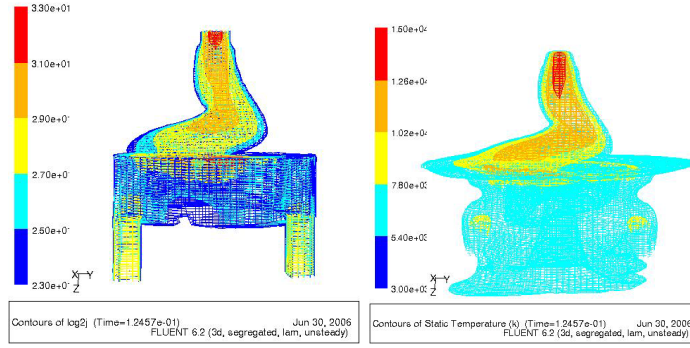

Figure 8.2: Plots of log2 of current density vs temperature for the same arc (1 kA Ar).

8.1 Arc deformation in stable rotation

The first observation we make of the rotating arcs is that they have curved, corkscrew-like shapes.

As the arc is moved by the electromagnetic rotating force, it experiences fluid-dynamic drag. The equilibrium between the driving force and the drag force determines the rotating speed. However, neither of the forces are uniformly distributed[1], so for an assumed given angular speed there will be forces acting on the arc to deform its shape. Specifically, the outer (lower) part of the arc has a much higher drag force compared to the angular speed and will lag behind.

This deformation makes the arc longer than the nominal arc length, with correspondingly higher voltage. The arc also gets a tangential current component which we shall come back to.

Figure (8.3) show the typical arc shape for a stable rotating arc. Figure (8.4) shows a picture sequence for stable rotation of a 1 kA Ar arc in a 10 mT axial magnetic field. The direction of rotation is counter-clockwise in all the figures in this chapter: motion is towards the reader on the left side and away from the reader on the right side.

8.1.1 Rotation speed

The rotation speed is theoretically determined by the balance of driving and drag force. As confirmed by the simulations, the drag force is higher and the angular velocity is lower the further away from the axis we get. The electrode mechanisms

[1]The driving force depends on the r component, i.e. direction of the arc, and the drag depends on viscosity and arc thickness as well as rotation speed.

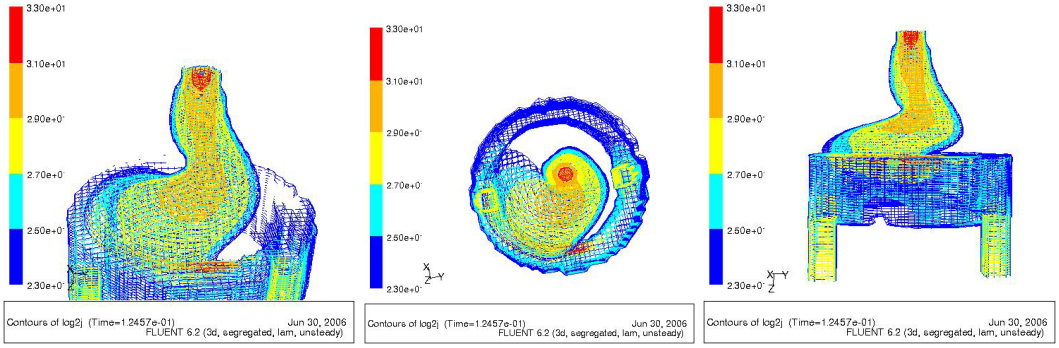

Figure 8.3: Oblique, top and side view of typical arcs deformed by rotation. Plot of log2 of the current density. The arc gets a characteristic helical shape. The current density in the anode cylinder and legs is high enough to show on the plot.

of the anode spot are assumed to happen faster than the timescale of the rotation, so that there is no 'friction' on the anode surface.

Based on the very limited data for rotating arcs, it is impossible to draw conclusions for systems other than the simulated one. For the PPM geometry, frequencies of some hundred Hz can be expected with the currently used magnetic fields. The main point is that *there is a maximum velocity* where further increasing the driving force kicks the arc into unstable behaviour rather than increase the rotation frequency. (More about this in section 8.2).

After discovering this, the operation of the PPM reactor was made more stable by simply decreasing the driving magnetic field.

Arcs in different plasma gases and at different pressures get deformed in the same way, but the degree of deformation for a given rotation speed is different. Also, the maximum rotation speed and transition from stable to unstable rotation depends on pressure, viscosity and other material parameters.

Arc flattening: deformation of the arc cross-section

In addition to the deformation described above, the cross-section of the arc is also deformed. The degree of deformation depends on the aerodynamic drag, somewhat similar to that of an arc in cross flow. The arc gets flattened in the direction of movement, and fast moving arcs resemble flat bands more than cylinders.

The important observation here is that our *radiation model cannot deal properly*

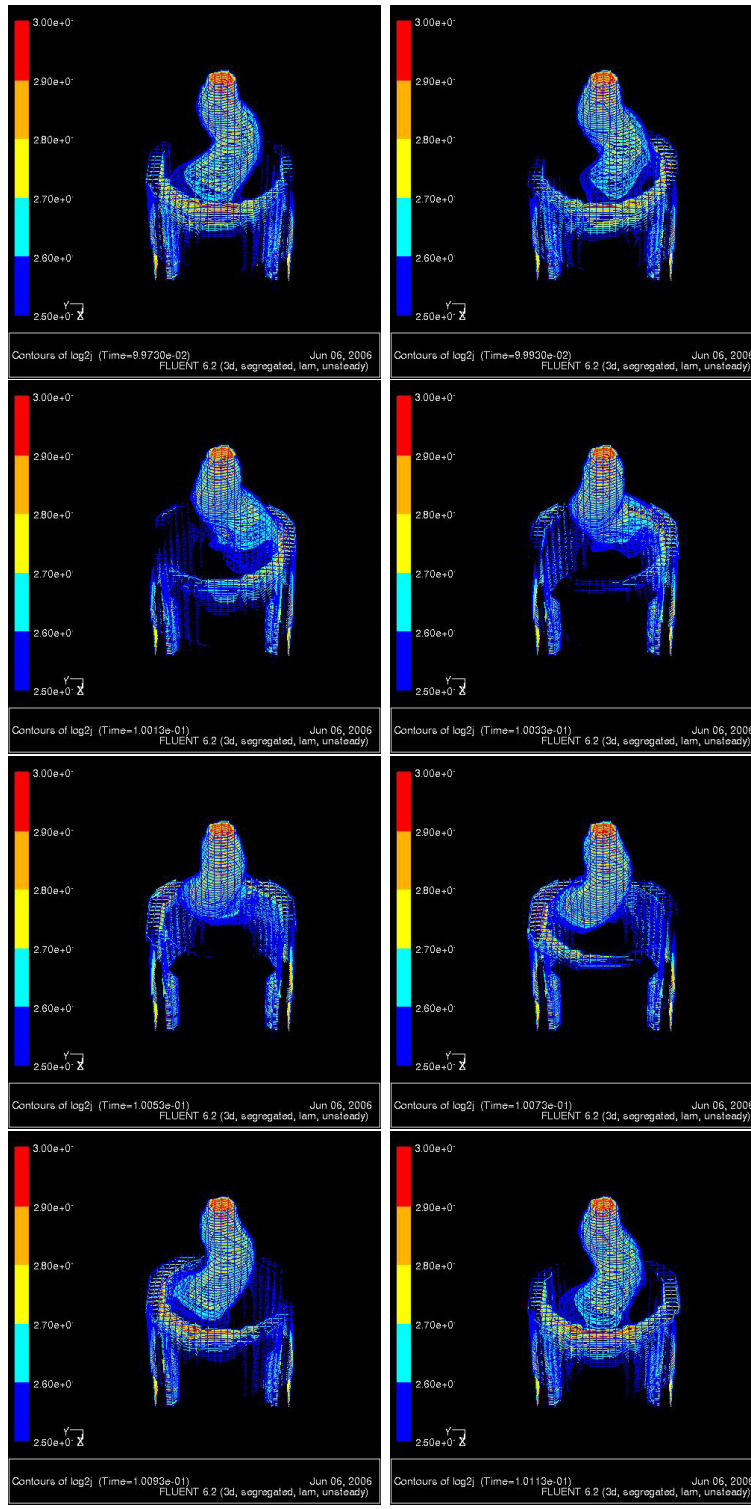

Figure 8.4: Time series for a 1 kA Ar arc in a 10 mT axial magnetic field. Plot of log2 of current density. The period obtained is about 1.4 ms, or about 700 Hz.

with this. The model used assumes the radiation to have a characteristic radius for reabsorption. For the flattened arc, radiation escapes more easily through the flat sides (up and down) than through the 'sharp edges', making the radiation problem more anisotropic. Implementing the full IMPC model (described in section 2.3.3) will help resolve this.

Also, the drag coefficient and boundary layers change as the arc gets flatter, thus affecting turbulence. The flattened shape is more aerodynamically favourable than a cylinder, so the flow field should be smoother - however the shape is affected by the heat balance through the temperature-dependent viscosity. To do accurate computations for the arc flattening, the IMPC radiation model must be used together with an appropriate turbulence model, a finer grid and possibly a moving grid method.

Comparison with theoretical model

There exists a simple theoretical model for deformation of rotating arcs in an axial magnetic field, by Essiptchouk et al [18]. This model is based on a coaxial system where the relative radius of the anode and cathode are not too different, and both anode and cathode spots can move freely. The model further assumes the arc to be a fixed channel with constant current density and velocity along the channel, very similar to the wire model ('garden hose model') described in the previous chapter.

Given all these assumptions, the theoretical arc shape is given by the curvature angle $\phi(r)$ as:

$$\phi = \sqrt{\left(\frac{r}{A}\right)^2 - 1} - \arccos\frac{A}{r} \tag{8.1}$$

where A is a constant containing the anode radius, arc diameter, arc density, drag coefficient, arc current and magnetic field strength.

Essiptchouk's model is not immediately applicable to our geometry, as it assumes the arc to be in a plane. It still serves as a guideline for what should be expected. The significant qualitative results are that the curvature increases with r, and that the curvature is *independent of the anode radius*. Making more comparisons with this simple model seems risky since the arcs in this work burn horizontally from the cathode, and thus have the cathode jet acting axially rather that radially as the model assumes. Also, the real arc expands and does not have the same drag coefficient along the entire length. Still, the spiral shape acts as a reference shape in the same way as the AC deflected shape for the wire model.

8.1.2 Vertical anode attachment position

Another observation made both from the simulations (see figure 8.5) and during experiments is that *the anode attachment moves up and down, depending on the rotation.* In the real reactor, the applied magnetic field is not purely axial but has a controllable radial component just to control this movement (ref. section 9.4.1). But in the simulations, this effect must be explained by something else.

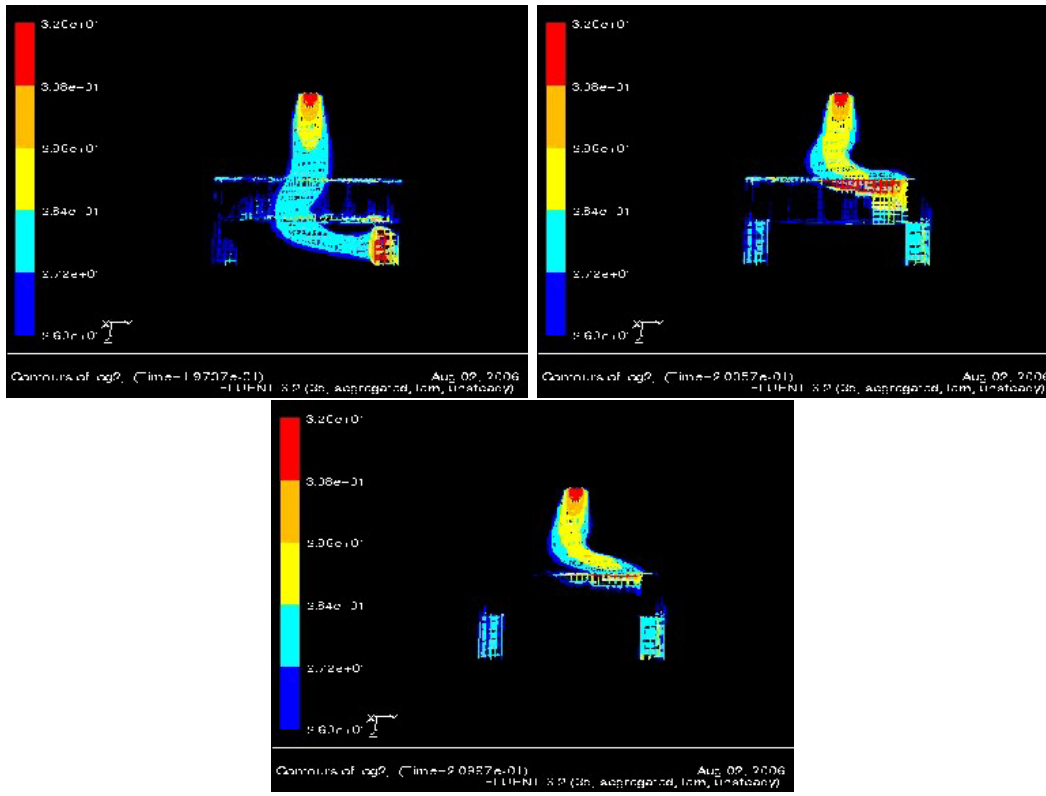

Figure 8.5: Pictures showing different anode attachment heights for different magnetic field strengths in the range 5-20 mT.

The rotating arc system is dominated by two forces: the cathode jet acting downwards, and the electromagnetic driving force acting in azimuthal direction. Since both depend on radial current components, the ratio of forces equals the ratio of the self-generated and the externally applied magnetic fields. The self-generated magnetic field is not easy to calculate, but let us assume it is similar to the field for the free burning mode: about 10 mT for 1 kA distributed in a 2 cm radius arc. The axial fields used for rotation are correspondingly in the 5-40 mT range; i.e. of the same order of magnitude.

The explanation for the anode spot vertical movement is related to the ratio between downwards and outwards force. For low rotation speeds, the cathode jet pushes the arc down. But as the rotating force increases, the outwards push becomes stronger and the arc hits the anode at a higher position. The following section reveals what can happen if the rotating force is too high.

8.2 Stable, metastable, overshooting and short-circuiting rotation modes

As illustrated in the video files and in figures (8.4-8.12), there are at least four different modes of rotation for the plasma arc in the PPM-like geometry.

8.2.1 Stable rotation mode

The first mode is the simple *stable rotation mode* where rotation speed, arc deformation and thus arc length and voltage are all constant in time. In this rotation mode, the rotation speed changes with the magnetic field strength. The arc shown in figure (8.4) is an example of stable rotation.

8.2.2 Metastable rotation mode

The second mode is difficult to recognise on plots and even on the video files, but is obvious if tracking the arc voltage. This is the *metastable*, or *periodic mode* which occurs when the magnetic field is increased. It looks similar to the stable mode but the arc length and voltage oscillate periodically. The explanation for this is that the lower (outer) part of the arc cannot rotate fast enough to keep up with the upper (inner) part, and the arc actually rotates with two speeds. As the fast rotating part outdistances the slow one, the arc length increases, to decrease again as the fast overtakes the slow again as illustrated in figure (8.6). The voltage thus varies periodically with the beat[2] frequency of the system. Also, the anode spot velocity also seems to vary periodically, but the variations are small and hard to measure.

The obvious way to recognise the metastable mode is to look at the voltage variations. Apart from this, a 'kink' on the arc (the faster rotating top coil) is an indication.

[2]If you add two periodic signals together, the envelope curve varies with a frequency equal to the frequency difference between the signals: this is the beat frequency.

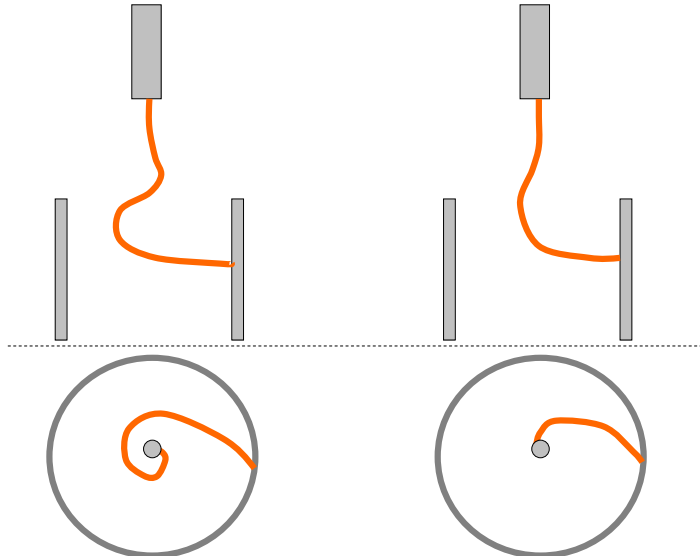

Figure 8.6: Illustration of the metastable rotation mode (exaggerated). The top part of the arc rotates faster than the bottom part of the arc. The total arc length varies depending on the relative phase difference. The lower parts of the arc are at the same phase in both drawings, but the upper parts have different phases.

The next two rotation modes are both complex (chaotic) rotation modes that can occur when the magnetic field is too high for stable rotation. Typically the simulations give a mixture of the two modes, but as they depend differently on the geometry they should be treated as two different modes, especially if considering upscaling of the reactor. Figure (8.8) shows a typical voltage/time plot for the 'chaotic rotation mode' that is actually a mixture of overshooting and short-circuiting.

8.2.3 Overshooting mode

The third rotation mode observed is a quasi-chaotic *overshoot mode*, with no simple periodicity and extreme voltage peaks. This is directly related to the strong rotation force moving the arc outwards and upwards until it misses the anode and overshoots. The resulting arc is very long and unstable. This overshoot mode depends on geometry[3] as well as rotation speed and could in theory be periodic, but no regularity was observed in the simulations.

Overshooting of the anode is a prime suspect for the arc short-circuiting to the con-

[3]if the anode reaches to the top of the reactor, the arc cannot pass over it!

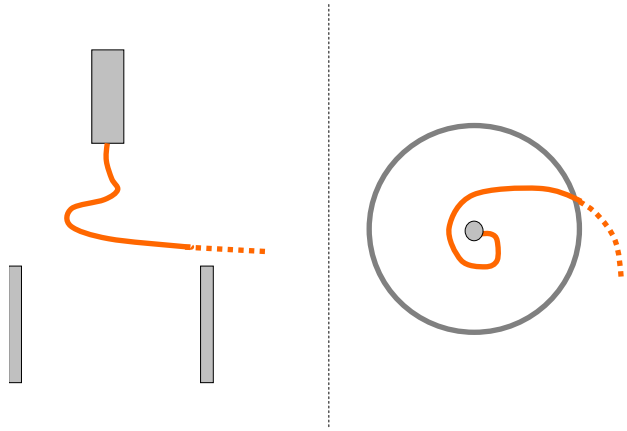

Figure 8.7: Illustration of overshoot mode. Front and top view. The strong rotating force drags the arc out too far too early to hit the anode. The result is a much longer, unstable arc.

ducting graphite walls[4]. However, with careful tailoring of the rotating magnetic field as suggested in section 9.4.1, the arc position can be controlled.

8.2.4 Short-circuiting and restrike modes

There fourth observed rotation mode is a *short-circuit mode*, which resembles the metastable mode, is chaotic or at least not simple periodic. As illustrated in figure (8.9), if the deformation of a rapidly rotating arc is large, the arc will form several coils, like a curled-up snake. If the radial distance is small between two coils, the arc may short-circuit on itself. If the outer arc travels almost parallel to the anode, it may also short-circuit on the anode. Any short-circuiting distorts the velocity and temperature field, making the system unstable and starting new short-circuits. The result is a complex rotation mode with frequent and large voltage drops and peaks.

In the simulations, the arc typically short-circuited on itself rather than on the anode. Often this happened together with the overshoot mode, so that the arc gets too long and very deformed, with the adjacent arc coils very close to each other. Also, the different rotation speeds of the coils (similar to the metastable mode) can bring them very close.

The short-circuit mode does not have to be as extreme as suggested in the illustration: if some effects on the anode slows down the movement of the anode spot itself, then the arc will make a new anode spot when the old one lags too far behind.

[4]This happened once in the PPM reactor. After changing the magnetic field from a diverging field to a 'magnetic bottle' field, it has not happened again.

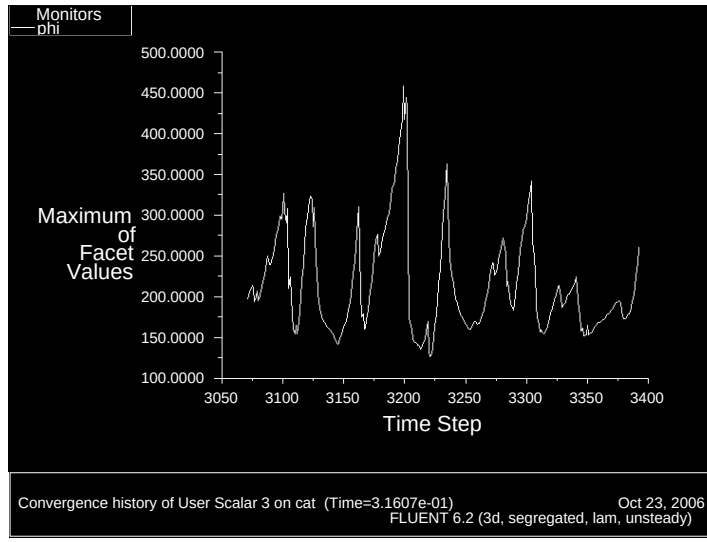

Figure 8.8: Voltage/time plot for chaotic rotation mode. This is a combination of overshooting and short-circuiting behaviour. The distance between peaks are typically 1-3 ms.

This kind of *restrike mode* is a variation of the short-curcuit mode, and can work in combination with a metastable rotation mode with the periodic voltage oscillation generating the 'punch' needed for the short-circuiting.

8.3 Time-series plots of selected phenomena

The thesis format is ill suited for presenting animations! The enclosed CD contains some animation files containing much more information than what can be plotted here. Some selected phenomena must be shown though.

Figure (8.10) shows snapshots of an arc short-circuiting on itself as it gets ripped apart by the rotation force.
Figure (8.11) shows snapshots of an arc short-circuiting on itself as two coils get too close to each other, as illustrated above.
Figure (8.12) shows snapshots of an arc with a jumping anode spot.

8.4 Experimental observations

No dedicated experiments has been done to observe the different rotation modes. However, high-speed video footage from function testing with Argon in the PPM

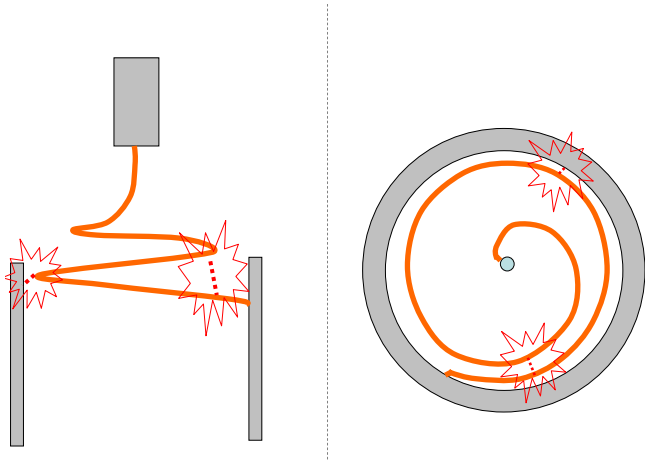

Figure 8.9: Illustration of the short-circuit (arc-arc) and restrike (arc-anode) modes. If the deformation of the rotating arc is extreme, the arc can easily short-circuit on the wall or on itself as indicated in the drawing. The vertical distance between the arc coils is typically small, and the real arc is much thicker than the illustrating line.

reactor reveals different modes. Temporary arc splitting and extinction/ restrike behaviour was observed, as shown in figure (8.13). The jumping anode spots typically moved slower than the arc body, and (although hard to discern) the upper part of the arc seemed to rotate faster than the lower part.

This behaviour is indicative of the restrike mode described above coupled with a metastable rotation. As the frequency of the rotation is orders of magnitude faster than the voltage logger (1 Hz), no periodicity in the voltage oscillations due to the actual restrikes could be detected. However, differences are registered for changes in the typical length obtained before the restrike.

Footage was also made of an arc in helium. The main observations were that the radiation spectrum of helium makes it difficult to resolve the arc against the hot background (graphite at about 2000 K), and that the helium arc was rotating much faster than the argon arcs. Due to limitations of the camera, only a small portion of the arc could be filmed at the needed time resolution. Still, the footage (figure 8.14) suggests that the helium arc has a stable helical shape near the cathode, that the anode spot moves *much slower* than the arc body, and that the arc goes two or three full rounds before hitting the anode. Because of camera limits, only snapshots were taken, and we cannot know for sure whether the anode spot jumps or move continuously.

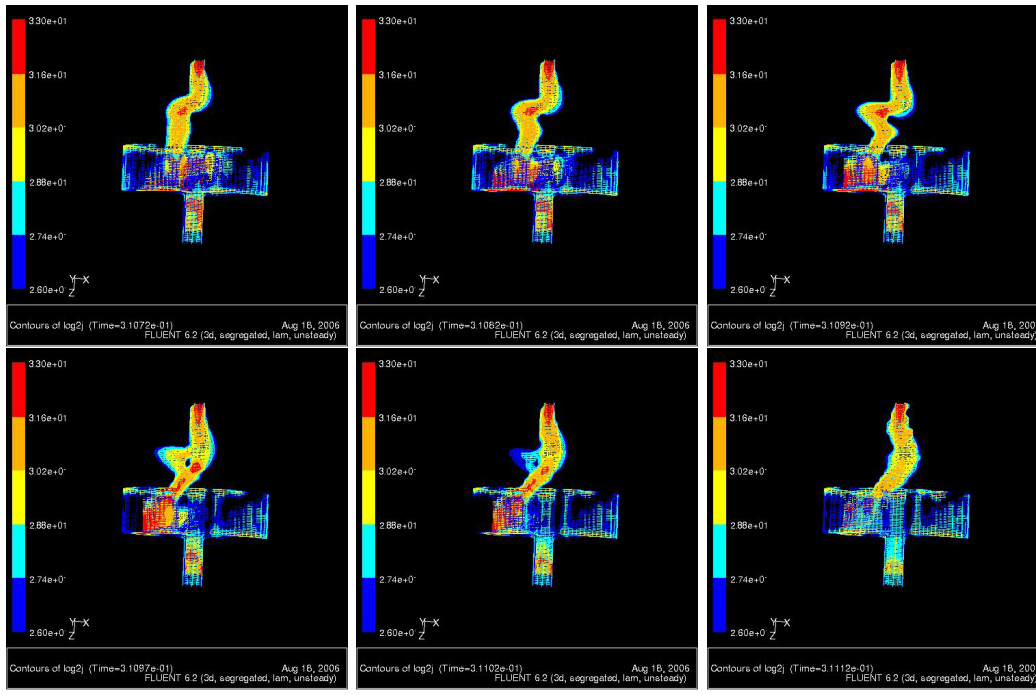

Figure 8.10: Snapshots of a He arc displaying a simple *short-circuiting behaviour*. A kink in the arc gives a large difference in rotation force, dragging the arc out horizontally until the voltage becomes too large and the arc short-circuits on itself.

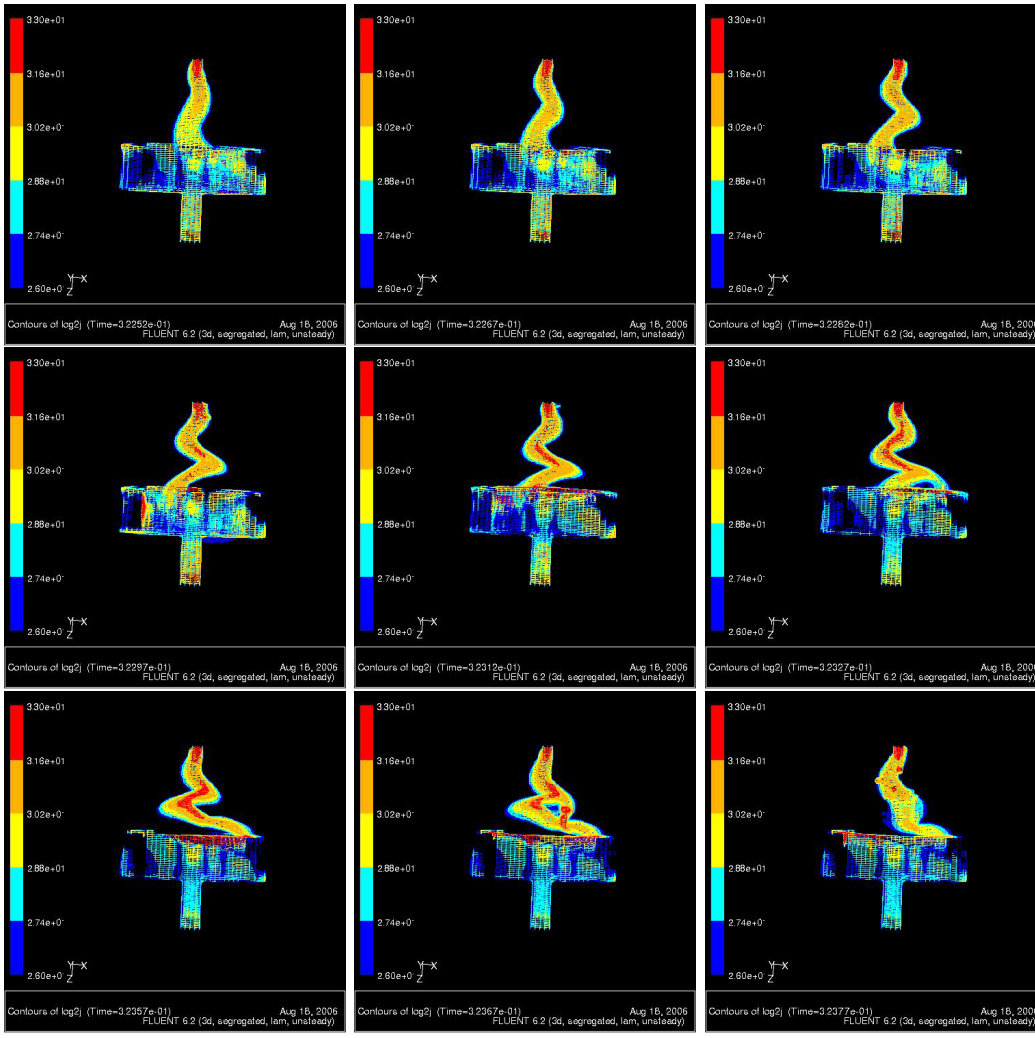

Figure 8.11: Snapshots of a He arc displaying a different *short-circuiting behaviour*. Drag deformation gives the arc an increasing number of coils. Eventually the arc coils come close enough to short-circuit the arc, similar to the illustration in figure (8.9). An anode restrike can also be seen.

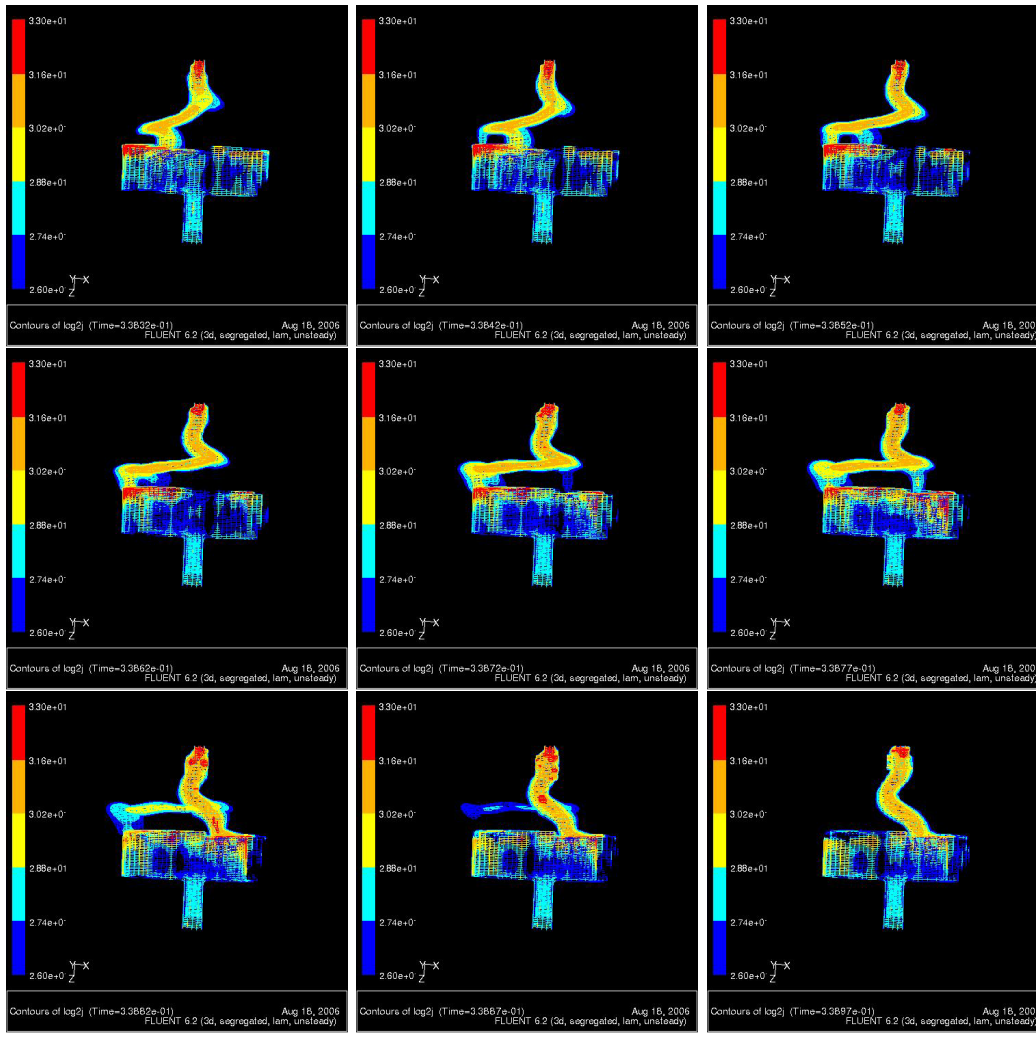

Figure 8.12: Snapshots of a He arc displaying *restrike behaviour*. The anode spot jumps around as the arc rotates. (The arc initially burns on the far side on the anode, the first jump is also in the direction of the movement).

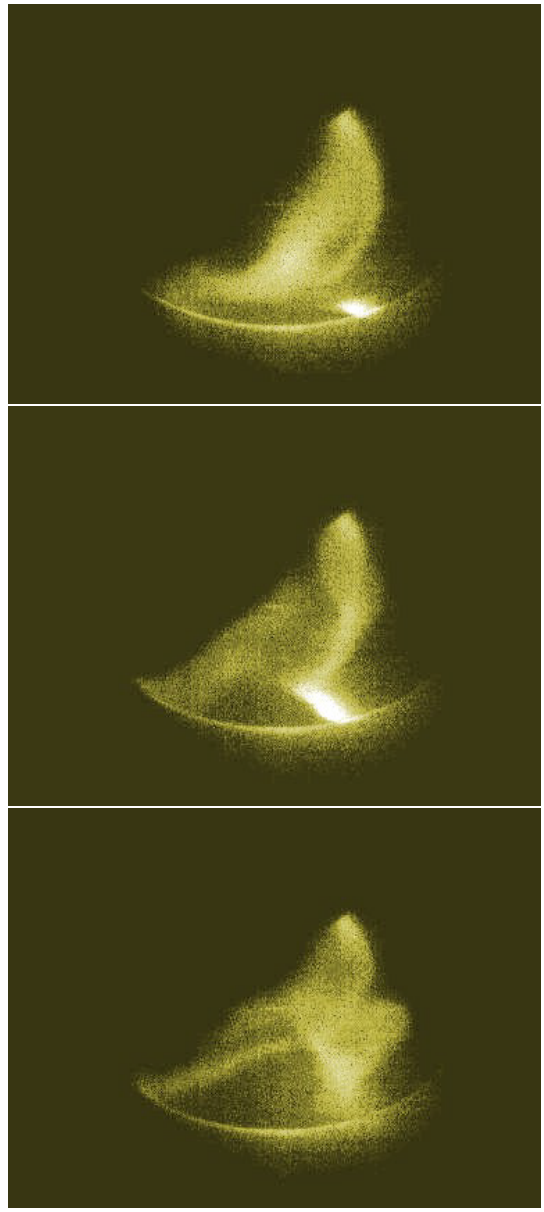

Figure 8.13: Snapshots of a rotating Ar arc. The poor quality is due to filming the arc indirectly through the observation window, and the arc cannot be seen at all when on the far side of the cathode. This sequence shows the same short-circuit behaviour as simulated in figure (8.11). Initially, the arc is extremely dragged out, disappearing to the left and coming back around on the right to the glowing anode spot. We then see the arc short-circuiting and reducing its length by a full round. The last frame shows the same characteristic arc shape as the last frame in figure (8.11).

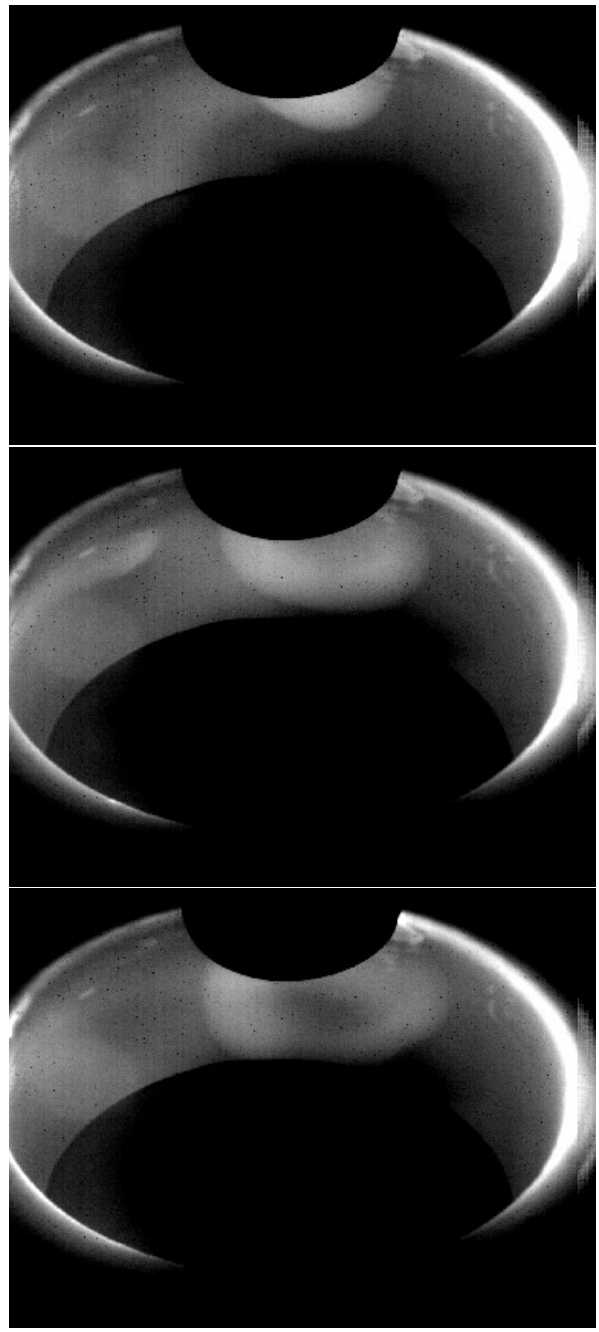

Figure 8.14: Snapshots of a rotating He arc. Pictures show the low visible light emission of helium plasma, and indicates the spiral shape. The arc settles on the hot anode spot on the right of the picture. In the top picture, the arc goes about one and a half round, in the bottom about two rounds. Pictures are from different periods of rotation.

This behaviour is indicative of the chaotic short-circuit mode. Again, the voltage logger cannot hope to resolve the voltage fluctuations. The practical conclusion is that the magnetic field used for rotation is too strong, and while the arc indeed is dragged out to make a voluminous plasma zone, the voltage instability is not wanted. Later experiments with the PPM reactor used weaker magnetic fields and observed a more stable arc (i.e. less flickering observed on the monitoring camera).

Chapter 9

Upscaling of geometry and arc current: effects on temperature, flow and arc power

One of the most useful applications of a working arc model is to predict the effects of upscaling from lab scale to industrial scale. The vector potential model as presented in this work is capable of doing this, it is just a question of computing power. Since the gradients in a high current arc are as steep, and the anode spot movement just as fast, the resolution in space and time should ideally be just as high as in the smaller system.

Due to limitations in time and computing power, a full investigation has not yet been made of an upscaling of the rotating arc in the PPM reactor. However, simulations have been made of upscaled simpler systems that give valuable information when combined.

9.1 Results from upscaling axisymmetric arcs

This simulation series uses the VP method to investigate how the temperature field and arc voltage changes with upscaling of the geometry and arc current in the system. The modeled arcs are axisymmetric free-burning arc in the simple computational domain shown in figure (9.1). Results for temperature profiles are shown in figures (9.2-9.6). Computed current-voltage characteristics are shown in figure (9.8).

In this series there were two parameters to be tested: geometry scale (arc length)

and current. In the axisymmetric simulations these are independent variables [1]. A reasonable a-priori choice would be to scale the arc current proportional to the reactor area, but in order to get good data for the arc current-voltage characteristics the parameters must be tested independently. Figures therefore also include cases with the reference 1 kA current in scaled geometries.

9.1.1 LTE solution

In this particular series, the non-LTE problems near the anode have been circumvented through the primitive method of letting the computational domain contain part of the anode. By allowing the anode material to be heated (above what may be a realistic temperature), the computed temperature gradients become less steep and the non-LTE effects much smaller. The anode fills the same fraction of the total domain for the cases in figures (9.2-9.7).

9.2 Arc characteristics and arc splitting

Figure (9.8) shows computed current-voltage characteristics for axisymmetric argon and helium arcs of different lengths.

Extrapolating this information seems to tell us everything about how the arc power scales. However, reality is always more complicated. As will be discussed below, the length of a moving arc will depend on more factors than just the geometry. Aerodynamic drag deforms the arc, making a rotating arc longer than its nominal length. The aerodynamic drag also tends to flatten the cross-section of the arc, giving a real current-voltage characteristic that also depends on velocity, which in turn is controlled by the externally applied magnetic field.

9.2.1 Different anode attachment modes

One interesting observation from the series is that we see the two different anode attachment modes for He arcs: For higher current arcs, the temperature profile near the anode is *diffuse*, like in Ar arcs. But for lower current arcs, we can see a clear *constriction* of the arc. The transition from diffuse to constricted mode occurs around 100 A, as found from the current-voltage characteristics plot in figure (9.9) which is plotted on logarithmic scale to exaggerate the difference. The different attachment modes are illustrated in figure (9.10).

[1] assuming that the current-voltage characteristic of the power supply allows us to maintain the given current irrespective of the nominal arc length chosen

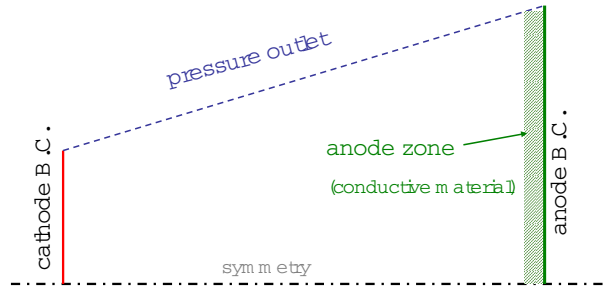

Figure 9.1: The simple computational domain used for upscaling of axisymmetric arcs. The material in the 'anode zone' (corresponding to graphite) is immobile and has a very high electrical conductivity compared to the plasma ($\sigma = 10^5$ S/m). The cathode current has a parabolic distribution and an average current density of 10^7 A/m^2 for all cases

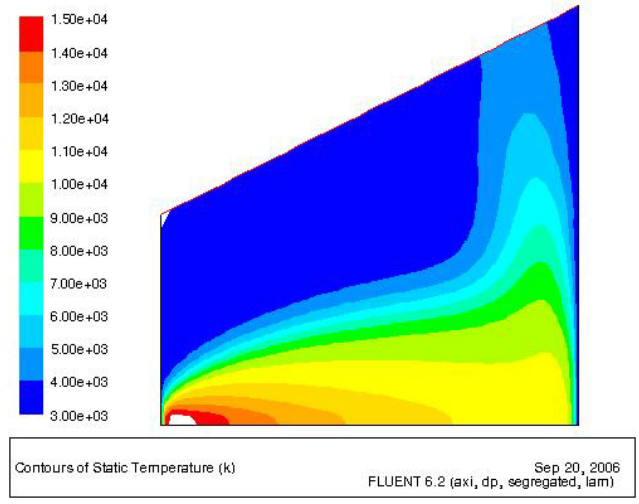

Figure 9.2: Temperature plot for an axisymmetric 5 cm 250 A Ar arc (computed with the VP model)

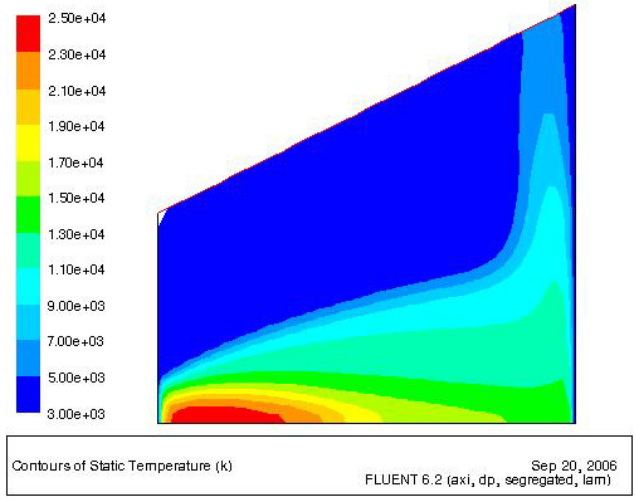

Figure 9.3: Temperature plot for an axisymmetric 5 cm 1 kA Ar arc. Note that the temperature scale is very different from the previous figure

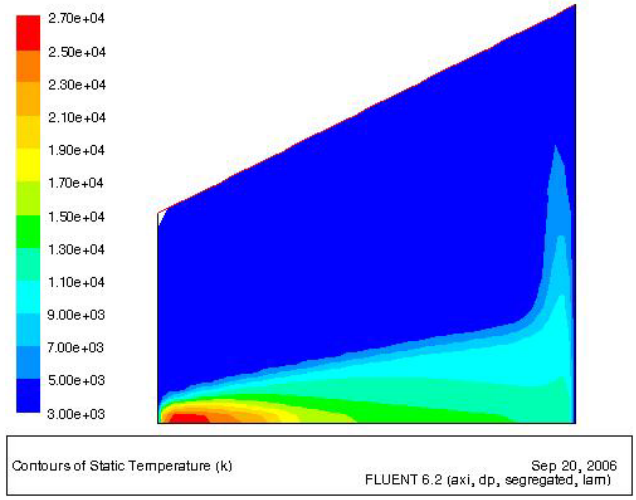

Figure 9.4: Temperature plot for an axisymmetric 10 cm 1 kA Ar arc

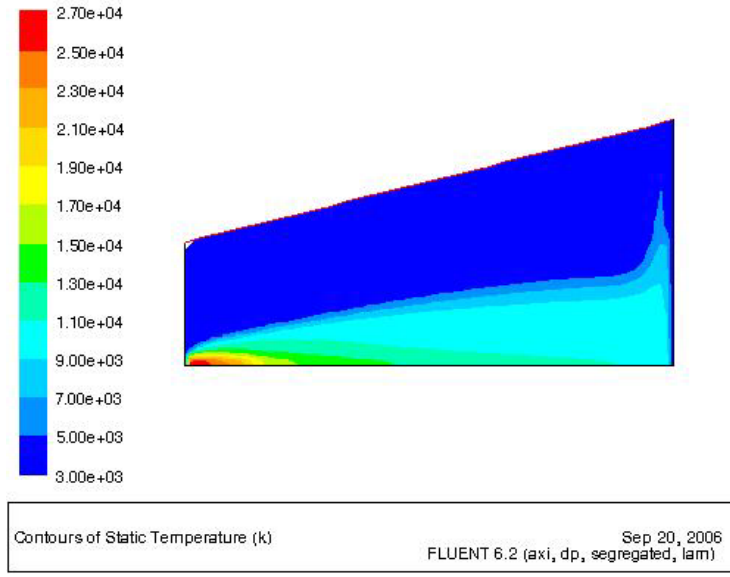

Figure 9.5: Temperature plot for an axisymmetric 20 cm 1 kA Ar arc

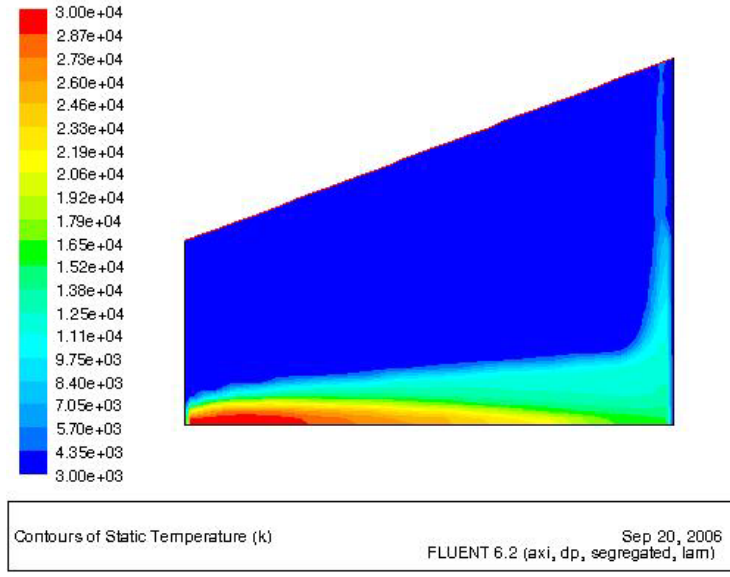

Figure 9.6: Temperature plot for an axisymmetric 20 cm 4 kA Ar arc

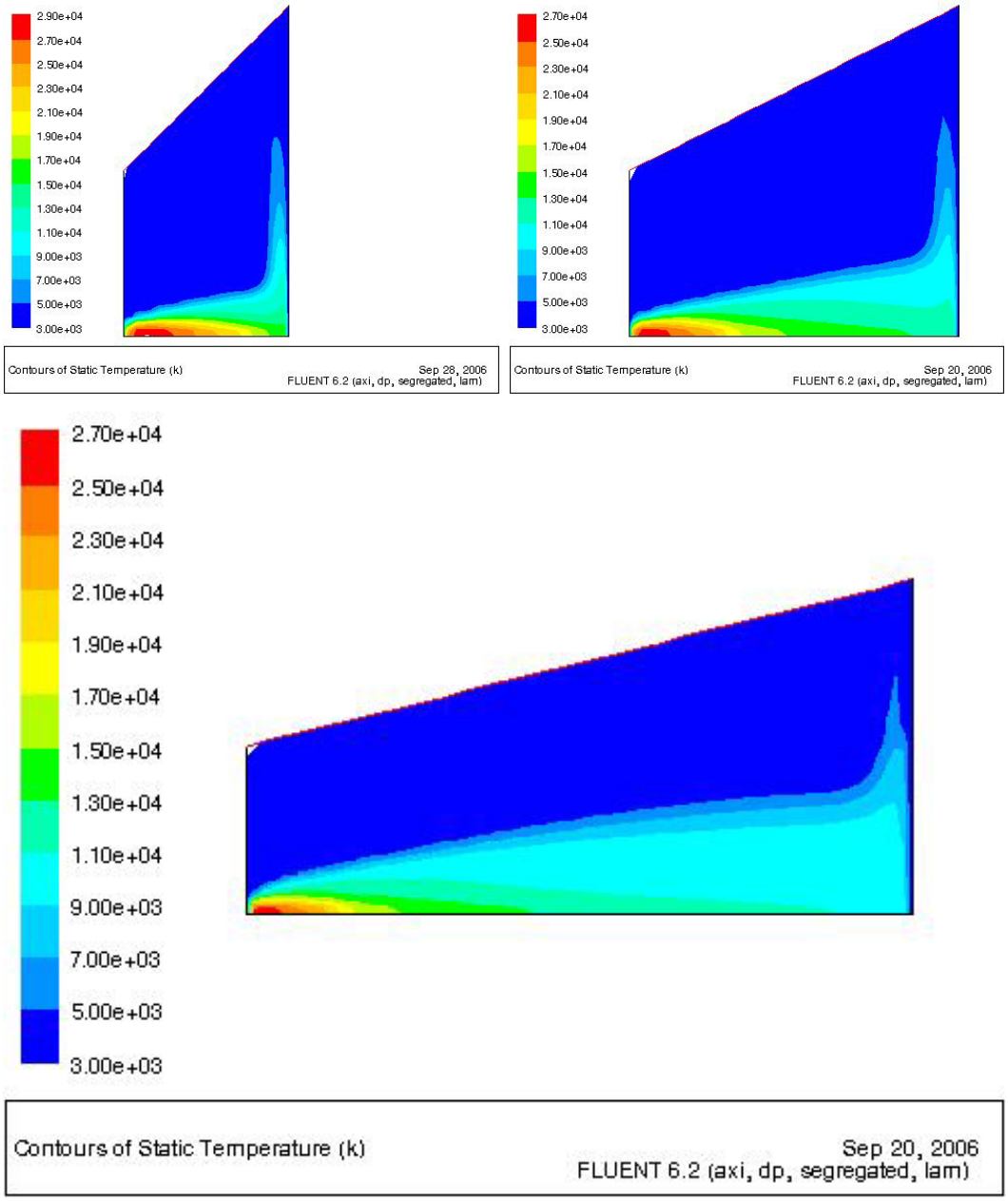

Figure 9.7: Same-scale plots of a 1 kA Ar arc of 5 cm, 10 cm and 20 cm.

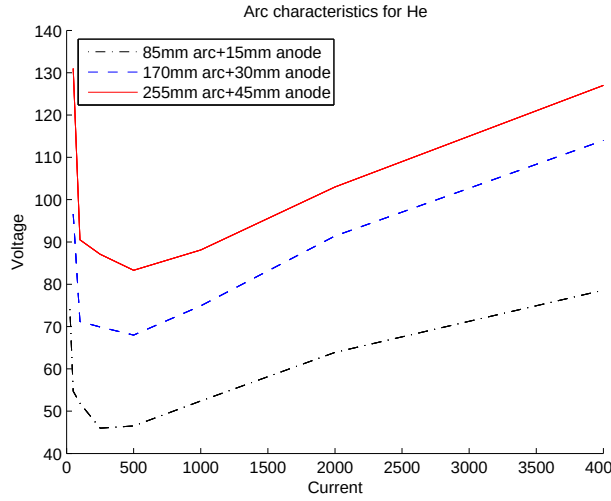

Figure 9.8: Plot of He arc current-voltage characteristic for three different arc lengths

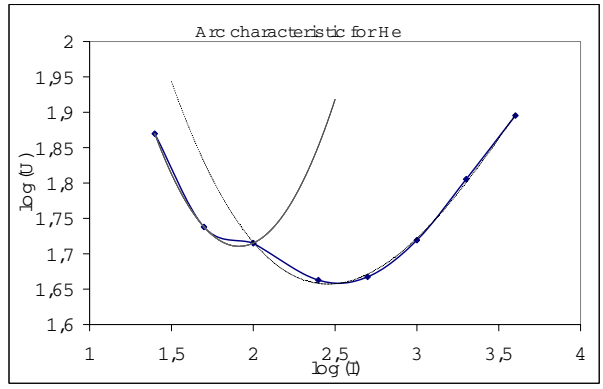

Figure 9.9: Same data as the bottom graph in figure 9.8) pertaining to a 85 mm He arc, but plotted on log-log axes. Imaginary trend lines are added to exaggerate the difference between constricted and diffuse anode attachment mode.

This phenomenon is similar in appearance to the one shown in figure (6.17) that was caused by our simple LTE assumption. The present phenomenon, however, comes from the material properties, namely the steep temperature dependence of electrical

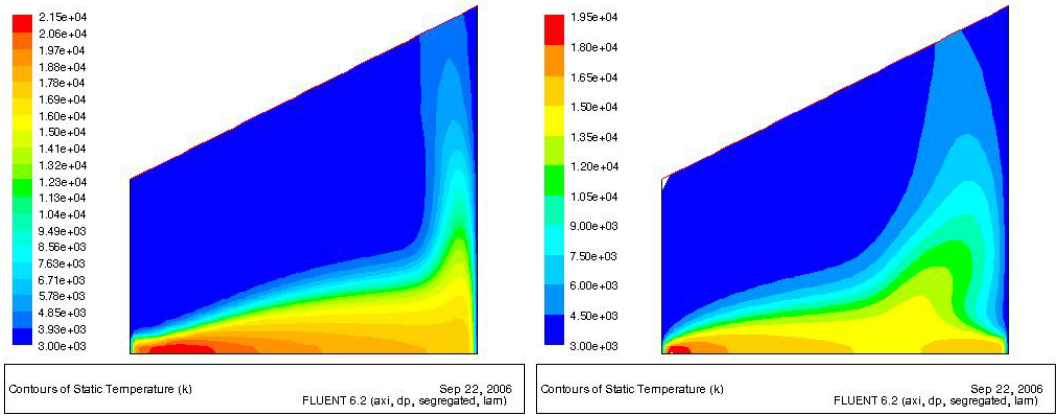

Figure 9.10: Illustration of different anode attachment modes for helium. *Left:* 10 cm 1 kA arc shows a normal diffuse mode. *Right:* 10 cm 250 A arc shows a constricted mode.

conductivity in helium, and is therefore a real physical effect. When the total arc power is too low, the anode plume is simply too cold to conduct well.

As this phenomenon only occurs for relatively low arc power, it is not so relevant to industrial upscaling except as an illustration of how computed results for small scales as a rule cannot be extrapolated directly.

9.2.2 Arc splitting

If the voltage over two parallel arcs at roughly half current is less than the arc voltage at full current, then the arc will be more stable if it splits in two. This can have consequences for the stability of the arc plasma in the reactor, as the voltage can make large sudden drops.

The arc current-voltage characteristics let us predict the possibility of arc splitting. Because the two 'baby arcs' interact both through attracting magnetic forces and through convective and radiative heat transfer, the prediction cannot be accurate. Also, there is a high voltage barrier for the splitting itself that requires an external influence (deformation from movement, voltage spikes in the power supply, inhomogeneities on the electrodes etc) to overcome.

The characteristics plot indicate for what current ranges splitting is possible: we see that for a 10 cm argon arc $\partial U/\partial I$ is *positive* (rising characteristics) from about 100 A, and an arc of some hundred amperes could viably split, in particular if reactor conditions are unstable. Indeed, high-speed filming of the PPM reactor arc

has revealed arc splitting when testing rotation in pure argon, as discussed in section 8.4. Below 100 A, $\partial U/\partial I$ is negative and arc splitting is not energetically favourable.

For helium the characteristic is rising from about 500 A, meaning there can be no stable[2] arc splitting for currents below this. No splitting of He arcs have been observed with high-speed filming, but this could in part be due to the low emission of visible light (the radiation is dominated by ultraviolet light) and the much faster rotation of He arcs making them hard to film.

For an industrial scale (10-100 kA) arc in helium, we must take into account that the arc can split and significantly reduce the voltage. However, voltages in this range are probably not interesting for nanotube production.

It is believed that a slowly *rising* arc characteristic is the most beneficial in order to achieve high power. A rising characteristic means less current is needed, reducing the cost of the power supply. A too steeply rising characteristic will encourage arc splitting and thus less total power. But if the characteristic rises slow enough, the attractive electromagnetic forces between parallel arcs will probably reduce the chance of spontaneous splitting sufficiently that good control of the reactor conditions can hold the (metastable) arc together.

As shown in chapter 8, a chaotic rotation mode will give (unstable) arc splitting regardless of characteristic.

Stability conditions and effects of arc splitting of high-current ($\sim$ 100 kA) AC arcs in submerged arc furnaces for Si metal production (SiO+CO plasma) were investigated by G.A.Sævarsdottir[51] using a MFD B-field model. The results in that work give similar conclusions, namely that upscaling to high currents makes arc splitting energetically beneficial.

In the PPM project, arc splitting would probably not be so bad as it would help generate a larger hot reaction zone. However, control of the arc behaviour is more important in order to reproduce the wanted conditions for nanotube growth.

9.3 Scaling laws for plasma arc power

Armed with working arc models and a bit of computing power, it is possible to search for some 'scaling laws' for plasma arcs. Similar to scaling laws for furnaces, these are not laws as such, but thumb-rules for how the current/power and geometry size should be scaled relative to each other in order to aquire 'similar' conditions.

[2]there may still be temporary arc splitting when we have extinction and reattachment etc

Based on results presented here and in [60], we can draw a few conclusions.

• Different variables scale differently: it must be clear *which* conditions we want to reproduce in the upscaled system

• Higher current gives larger forces and higher[3] velocities. If the heating rate of feedstock and quenching of products are important, a simple upscaling is probably not enough.

• In order to have similar temperature conditions in the reactor, the power generated in the system must scale proportional to the power transported out of the system. Radiative energy transport scales proportional to the volume of the radiating arc ($\propto S^3$) assuming an optically thin plasma. Convective/conductive energy transport scales with the surface of the arc column ($\propto S^2$).

• The balance between convective and radiative losses depends on plasma gas, total power (ie. temperatures) and rotation. A smeared-out plasma will be more governed by convective/conductive heat transport than an axisymmetric free-burning arc. Also, again we must define what we mean with 'similar' conditions: are we interested in the temperature and flow near the arc or far away from it?

• It is not trivial how the arc power scales with the current, especially for dynamic arcs. For straight stationary arcs, arc characteristics can be computed.

• Nor is it trivial how the power scales with the nominal arc length for a given current. Unless close to extinction, the scaling factor is less than one (ie. double length gives less than double power). This is mainly due to the cathode and anode fall voltages which are almost independent of arc length.

• If the arc is scaled 'out of proportion' there are large qualitative changes: if the current is too low the arc will die. If the current is too high compared to the reactor size, the hot gas will be recirculated through the reactor faster than it can be cooled and the whole reactor will reach extreme temperatures.

Drawing conclusions from these observations is an uncertain venture indeed. The only certainty is that the arc power be scaled to somewhere between S^2 and S^3 where S is the linear geometry scaling factor.

Incidentally, the same ambiguity (S^2 vs S^3) is present in the procedures for di-

[3]A simple estimate gives $B \propto j$ and thus $F \propto j^2$, but higher gas velocity will keep the arc constricted and give a smaller j_r. We then cannot know the real scaling of F, only that it increases.

mensioning and upscaling of industrial submerged arc furnaces.

For a stationary, straight arc a doubling of the length gives a factor of maybe 1.5, and a quadrupling of the current gives a factor of maybe 5-6 depending on the arc characteristics, corresponding to a total power scaling of 7-9, or 'a bit less' than S^3. Just a doubling of arc current would give a total power scaling of 4-5, or 'a bit more' than S^2.

9.4 Upscaling of the rotation

Due to limited time and resources, only relatively simple simulations have been made for long high-current arcs. Some predictions can still be made from first principles and the existing results.

The upscaled arc has three important differences from the lab scale one that affect rotation: It has higher current, it is longer, and it has a stronger cathode jet and higher characteristic velocities. The cathode jet will typically try to straighten the arc, pointing it straight out from the cathode spot. The higher current means that the rotating force $\vec{j} \times \vec{B}$ from the external magnetic field will be much stronger, which will give higher rotation speed and thus more deformation. This can be countered by decreasing the external magnetic field generated by the magnet coils. The tendency for higher current to straighten the arc will partly counter the fact that the larger radius gives a larger deformation.

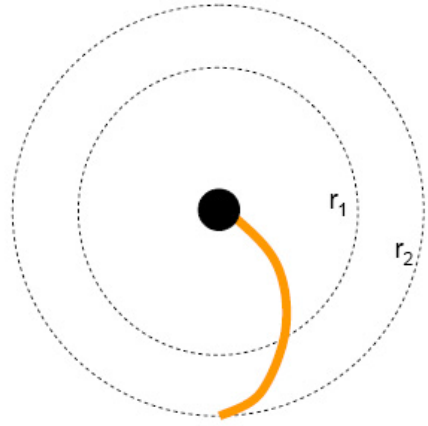

Figure 9.11: Illustration of how the stably rotating arc is deformed. When scaling up the anode radius, it is obvious that the total arc length increases by more than the geometric scaling factor. The rotation is counter-clockwise

The total length of the deformed stable arc increases non-linearly with geometry (see figure 9.11), so the larger geometry leads to a longer and more deformed arc even when the magnetic field is decreased to give similar rotation frequencies. The anode spot velocity also becomes higher in the upscaled system. This gives a lower maximum frequency before the rotation goes from stable to metastable mode. The transition from metastable to chaotic mode depends on geometry, but in general the higher velocity in the upscaled system will make it more prone to entering unstable rotation modes. As has been discussed in chapter 8, a customized magnetic field with a slight 'bottle effect' helps holding the anode spot at the desired height and prevent loss of control. This has already been implemented on the existing PPM reactor.

Our predictions then about the stable rotation of a long high-current arc are these:

• The external magnetic field must be lower, and the arc will therefore be more sensitive to magnetic disturbances, such as the magnetic stray field from the cables connecting the reactor to the power supply.

• The external magnetic field should have a 'bottle effect' to help maintain the anode spot at the desired height (see figure 9.12 and discussion below). If the anode spot moves too much, the arc can overshoot and miss the anode, giving chaotic rotation mode.

• Even with the same rotation frequency and a bottle effect, the upscaled arc will have a different shape: straighter near the cathode but more deformed away from it. The total arc length will increase more than the geometric scale factor.

• The upscaled arc will easier go into a meta-stable or chaotic rotation mode, with a periodic voltage fluctuation and a jumping anode spot.

9.4.1 Magnetic bottle effect

The magnetic bottle effect illustrated in figure (9.12) has been observed during operation of the PPM reactor. This means *azimuthal* currents are flowing in the plasma. There are two plausible causes for this:
• The *spiral shape* of the deformed rotating arc is associated with an azimuthal current component.
• If the plasma (which is a conducting media) moves in axial direction towards a 'bottleneck', the radial component of the magnetic bottle field will give an *induced* azimuthal current $j_\theta = \sigma v_z B_r$.

In both cases, the magnetic bottle effect gives a stabilising force that keeps the

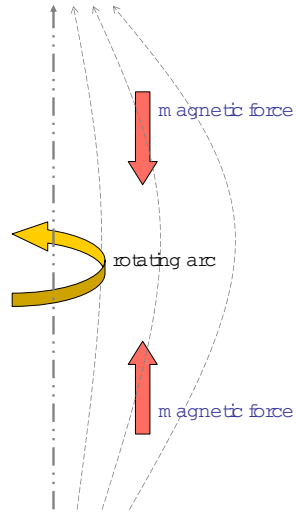

Figure 9.12: Simple illustration of the magnetic bottle effect. The azimuthal current component will be subject to a force pushing it up or down towards the middle of the bottle. By shaping the external magnetic field it is possible to control the anode attachment position.

arc burning at the desired height. By shaping the magnetic field during operation the anode spot can be kept in position even if the rotation force is increased or decreased.

9.5 Is industrial scale CNT production feasible?

There are still many unknown variables that must be determined before we can predict the accurate behaviour of the arc in an upscaled reactor. However, many of these variables, like rotation speed, are directly or indirectly controllable and can be varied to get the conditions we want.

This chapter has shown that we have a beneficial arc characteristic for upscaling, and that it should be possible to scale the total power towards the megawatt range employing a conventional DC power supply. Also, the figures show that with the proper balance between reactor size, arc length and total current, we can reproduce temperature or flow fields that much resemble those computed for the lab scale reactor. Rotation of a long high current arc is harder to predict, but we have many controllable parameters: number of coils and their position, radius and current (direction and magnitude) can be adjusted[4] to get the magnet field that gives the

[4]only the current through each coil can be adjusted during operation, but all the parameters are independent of the reactor geometry, except that the coil radius must be large enough to fit around

desired rotation.

At the time of writing, optimal conditions for carbon nanotube growth have not yet been determined. The preliminary upscaling tests indicate that we will have a large degree of control of the temperature and flow patterns in a upscaled reactor. Assuming the nanotubes grow on surfaces only the temperature field is really important and the challenge it more a matter of maximising the region with good conditions and making sure nanotubes can be taken out without dismantling the reactor. Assuming that the nanotubes instead grow in-flight, the velocity field becomes much more important. The high current arc may generate a mainstream recirculation that is very strong, but this too can be controlled, for instance with smaller holes in the anode to slow down the circulating flow.

All in all, the degree of control we retain on an upscaled arc together with the fact that we can reproduce similar conditions as in the lab scale arc leads to the conclusion that upscaling the PPM nanotube production process to the megawatt range is technically possible. The economic feasibility has not been investigated in this work though.

the reactor.

Chapter 10

Conclusions

10.1 Numerics and the arc models

The first and main conclusion to draw is that *the models work!* As demonstrated, we can model a wide range of arc behaviour, and those results that can be compared with experiments give matching results.

The main difficulties in modeling is the extreme gradients we get, particularly for the conductivity and temperature. Because all equations are interconnected and parameters are so nonlinear, the solutions can often be unstable in time and success or failure can depend on the choice of initial solution. As shown in this work, a relatively coarse grid and time resolution can give good 3D transient results while still keeping the workload in the range of what a single desktop computer (from 2005) can manage in a weekend.

Since the various models presented have different areas of use, they merit separate discussion.

10.1.1 The SD models

The SD models are simple and fast. This was the reason for investigating them at all, and the conclusion is that they are very fast. The obvious limitation is in the specification of the heating/momentum or choice of prescribed arc current distributions. Still, for axisymmetrical free-burning arcs the simple 'Ramakrishnan shape' ($r(z) = R_0 + c\sqrt{z}$) the model gives quite good results. This makes the SD models useful tools to keep, and in part validates much of the older work on plasma reactor modeling.

10.1.2 The MFD-B and MFD-β models

The MFD B-field model looked very promising from earlier works, but was hard to reconstruct due to changes in Fluent. The scaled β-model ($\beta = rB_\theta$) variant can reproduce old 2D-results, but the magnetic transport equation becomes unstable in 3D with the current solver.

The model is interesting in 2D and for validation purposes as there are less assumptions made and the boundary conditions used are not approximated like in the VP model. But for 3D cases it cannot compete with the VP model.

10.1.3 The MFD-VP model

The Magnetic Vector Potential model has been shown to be the most versatile and robust model. The computed results look physically sensible, and testing of two different approximations for boundary conditions give the same results for both cases, indicating a robust model, and also partly validates other work where the choice of boundary conditions may not be consistent.

The various assumptions are valid for the cases tested, but particularly if upscaling to high currents (100 kA range), the assumptions must be re-examined. Also, there are several improvements that should be made, as discussed later.

10.2 Physics of dynamic arc systems

The behaviour of the simulated arcs was not always as predicted. But in retrospect it was logical, and taught us much about arc physics.

The physics of helium and He-C arcs differ notably from the more common argon, nitrogen and air systems. The critical parameters are the *electrical conductivity* (σ) and the *net volumetric radiation density* (S_{rad}). For fast moving arcs the viscosity is also important when the drag force deforms the arc cross-section shape.

10.2.1 Characteristic shapes

The arc is influenced by *external forces*, magnetic forces that work in the whole arc and drag force that only works on the arc 'surface'[1]. For a constant external force, the arc settles into a characteristic parabola-like equilibrium shape.

[1]We can talk about the arc 'surface' because of the extreme temperature gradients and the temperature dependence of the viscosity. In addition to the steep rise in viscosity, the cathode jet also defines the arc as a separate 'object' for fluid-dynamic purposes.

There is a *characteristic response time* for the arc, and if the external force changes faster than this response time, the arc will never reach the equilibrium. For arc in an external AC field, the shape goes from parabola-like to sinusoidal as the frequency rises. Since He arcs have much higher characteristic velocities than Ar arcs, the He systems similarly have much lower response times and can be moved at much higher AC frequencies.

For rotation motion, the parts of the arc near the anode have phase lag compared to the cathode. This gives a *characteristic deformed shape* where the arc typically goes relatively straight down from the cathode but may end in a nearly flat spiral near the anode.

10.2.2 Characteristic behaviour patterns

Periodic or quasi-periodic behaviour can be caused by geometry effects or rotation motion. Some characteristic behaviour patterns have been identified:

For instability caused by geometry effects, there are two different modes: *extinction-restrike and periodic take-over*. Extinction-restrike mode happens on one surface, and happens when the arc is pushed down by the cathode jet or external flow until it becomes too long to sustain and short-circuits only to be pushed down again. The take-over mode is similar but happens on two surfaces: as the arc is pushed down or straightens out after short-circuiting, the top of the arc comes too close to the opposite surface and short-circuits.

For the rotating arc, there are several restrike or short-circuit modes in addition to a *metastable rotation mode*. The metastable rotation mode has a fluctuating arc length due to slightly different rotation speeds at different parts of the arc, but where the rotation is still slow enough that the arc expands and contracts rather than rip apart and restrike.

An *overshoot mode* was observed when the rotation forces moves anode spot position higher than the anode. This causes the arc to be extremely long and restrike shortly after.

Different *short-circuit modes* were observed during rotation. These can be divided into three groups, although real behaviour often shows a combination of these. All three types can be periodic or chaotic:

• Short-circuiting due to the arc becoming too long. These produce the highest voltage spikes, as the restrike often must be over a long distance. This is analog to

the extinction-restrike mode at a wall, and is typically connected to overshooting, but can be caused by any dynamic behaviour leading to an unstable arc shape.

• Arc-arc short-circuiting due to the arc connecting with itself. A too fast rotating arc will have the anode spot lagging further and further behind. At some point, two of the arc coils may get too close to each other (vertically and radially) and the arc short-circuits on itself. The voltage spikes are much lower than for the mode above, as the arc takes a shortcut in the existing current path rather than making a new path.

• Arc-anode short-circuiting due to the bottom of the arc running near tangential to the anode. Simply put, the anode spot jumps around rather than move smoothly. This is analog to the periodic take-over mode between two walls, but is not necessarily periodic. This mode also occurs for 'helix' arcs where the vertical distance between the coils is large.

10.3 Process control and engineering

As shown by the PPM project it is possible to produce carbon nanotubes with a thermal plasma process, but the degree of success depends on the conditions in the reactor. Having the tools to model conditions in and around a rotating arc is a great step towards finding and re producing the perfect conditions. There is still much work to be done, but some important conclusions can be drawn.

10.3.1 Controlling rotation

Rotating arcs are complicated, and easily go into unstable rotation modes. Three different approaches are suggested to control this:

• Using a tailor-made external magnetic field with a *magnetic bottle effect* helps control the vertical position of the anode attachment. This prevents overshooting mode and reduces the chance of the reactor being damaged by the arc short-circuiting to the walls. With two (or more) independent magnet coils, the anode attachment can be moved up and down by adjusting the ratio of currents in the coils.

• Simply reducing the external magnetic field strength. If the rotating force is too strong the rotation will not be much faster, but just become unstable. A weaker magnetic field allows the arc to stay in stable or metastable rotation mode, keeping the voltage and reactor conditions much more stable.

• The novel idea of using a two-phase external AC magnetic field to directly control the frequency of rotation. This has not yet been tested, but looks promising on the theoretical stage, especially if slower rotation is desirable.

10.3.2 Modeling the real PPM reactor - assumptions and reality

In addition to containing an unstably rotating arc, the real PPM reactor also has very complicated chemical conditions with an inhomogeneous mixture of helium, carbon vapour, methane and hydrogen plus condensed carbon micro- and nanostructures. The methane injection lances are positioned off-center, the external magnetic field is not homogenous and neither is the temperature on the cooled walls. Still, the simulations reveal behaviour that matches what is observed with high-speed cameras, and all recommendations made on the basis of simulations have given the expected results. The conclusion must then be that *even with all the simplifying assumptions, we can still model what happens in the PPM reactor.*

Again, there are still many improvements that can (and should) be made, and the success of modeling the PPM reactor does not automatically mean that the results will match as well for an upscaled version. Modeling must still be treated only as a useful tool to supplement experiments.

Chapter 11

Suggestions for further work

The overall conclusion for this work is perhaps that we have developed good tools for investigating arc phenomena, but there is still improvements to be made and more phenomena to be investigated. The selection presented here is not a plan for the continuation of the PPM project, but rather a list of tasks that can or should be done to complement and improve the work presented here. Several of the tasks are more or less obvious improvements and have already been mentioned in the preceding chapters, others are new and interesting directions of research.

11.1 Model improvements

There are many model improvements that can be made for the VP-model. In principle, all the simplifying assumptions could be replaced with less restrictive ones. However, some are more crucial than others, specifically the cathode model, the radiation model and the turbulence model.

The cathode current density has been prescribed for all cases presented in this work, typically as a parabolic distribution. A test series is needed for different distribution functions and average current densities on standard cases: currently many authors seem to have their own 'favourite distribution' that is used, based on what works best numerically and gives agreement with measurements. Also different total arc currents are interesting to investigate. Further work in this field should include combining G.Sævarsdottir's cathode/anode submodel[51][1] with the arc model, as well as improving the cathode model. Also, cathode and anode fall voltages should be accounted for, as these influence the total arc voltage and power.

[1]The cathode model is not described in this work as it was not implemented. The purpose of the model is to calculate the cathode spot current distribution and anode fall voltage as functions of the thermal conditions at the cathode, the thermionic work function of the cathode material and the ionisation potential of the gas.

Radiation losses have been modeled with the simple Lowke model, assuming the same characteristic reabsorption length R_{eff} in all direction and for all parts of the arc. For a coiled, expanding and severely flattened arc this assumption is obviously not good. Also, thick 'upscaled' high-current arcs will have areas at the surface of the arc where the reabsorption of radiation from the inner part can be so high as to give a positive net radiative heat transport. Implementing the full IMPC radiation method described in section 2.3.3 will solve these shortcomings, but gives a numerical problem that scales poorly with the grid resolution. In addition to the actual code implementation, the work in this field should then be in two directions: finding ways to reduce the problem size (for instance by assuming that all gas outside the arc is perfectly transparent), and finding ways to solve the problem on parallel processors.

Turbulence has been neglected in most of the presented simulations, simply to save time (and memory to avoid computer crashes). For the fast moving deformed and flattened rotating arcs, turbulent effects should be very interesting to investigate: turbulent drag should differ from laminar drag, and both conductive and convective heat transport will be changed. The first obvious step is a classical k-epsilon model, but a full Reynold Stress model or Large Eddy Simulation is needed to resolve the effects of turbulence in recirculating flow. The turbulence model should take into account that plasmas have high viscosity compared to normal gases.

For fast moving arcs, and especially if considering upscaling to high currents, the effects of **induced electric field** ($\nabla \times \vec{B}$) and corresponding current must be investigated. Order-of-magnitude analysis show that the induction term can be neglected from the scalar potential equation for our standard cases, but the effects are known to be important in industrial scale furnaces. For calculations on those, the induction term should be implemented in the code.

Testing should also be done to validate the assumption that we can neglect the **time-derivative of the magnetic vector potential** from the $\vec{A}$ field equation. The arguments are convincing, but a validation would be even more so. This term is connected with induction due to variations in the externally applied magnetic field.

In addition to an improved turbulence models, some **multiphase flow modeling** could be useful. This could perhaps be useful to investigate mixing of *hot and cold gas* (rather than assuming an interpolated homogenous temperature with corresponding transport properties in the whole cell). Even more useful would be the use of multiphase flow to model the mixing of *injected methane and plasma gas* in the PPM reactor.

As a special variant of two-phase flow, a **two-temperature model** could be implemented to investigate non-LTE effects near surfaces, in particular the anode, and

for short-circuiting and extinction behaviour. In addition to the model itself, thermophysical data must be calculated for the two-temperature systems. This is a field where others are likely to produce more good results very soon.

Further model improvement include adding an **electric circuit equation** for the whole reactor system. The real power supply will have a limited maximum voltage and a minimum response time. This means an absolute constant current (as assumed in this work) cannot be realized. A dynamic circuit model may reveal much more about arc instabilities. In addition, it will enable more realistic modeling of AC arcs.

As already suggested for the radiation model, work should also be done on rewriting the existing code for **parallel processing**. In a direct continuation of this work Fluent would still be the program of choice, but alternatively the model equations could be implemented in other existing code.

Finally, the code can forever be improved by adding transport and radiation data for new plasma gas mixtures and new pressures. However, the data itself is not as interesting as the capability to generate them.

11.2 PPM project support

These are 'practical' tasks to solve problems relevant to the PPM project at this time, but still of general interest.

Much more numerical model testing is needed for **upscaling of rotation behaviour**. As concluded, the different types of rotation modes depend on different geometric and operational parameters. When upscaling the reactor, it is not easy to predict if and how the rotation behaviour will change, so more testing on different upscaled geometries is valuable for the PPM project.

More testing is also desirable for rotation by (axisymmetric) **non-homogenous magnetic fields**. The magnetic bottle effect has been proved to work well experimentally, but is not adequately described theoretically for arc plasma. The coil setup may be further improved based on simulation results. This is also important when considering upscaled reactor geometries.

To determine and understand what conditions are needed for nanotube production, computations should be done to determine the full **temperature history** of injected carbon particles. This can be done through the *Discrete Phase Model* included in Fluent, but may require the computational domain to include outflow, cooler and filter in addition to the injection lances.

11.3 Novel application: two-phase rotation

The most exciting novel idea from this work is the concept of using two-phase or multi-phase AC fields to give a controlled arc rotation frequency, as described in section 7.2.5. Alternatively, by setting different frequencies for the coil sets, a number of more complicated periodic movement patterns can be obtained.

Work on this should include modeling, particularly to investigate what happens when the rotation speed reaches the arc response speed. More important though is to design *small-scale experiments* to prove the principle in practice.

In addition, there is the task of considering *possible applications*: the main advantage is that the arc heating effect can be spread more or less homogeneously over a large area in a controlled fashion, which potentially makes it useful for many situations. However, the physical placement of the magnet coils may perhaps provide limitations for certain applications.

Bibliography

[1] B.Andresen: *Process model for carbothermic production of silicon metal*, Dr.Ing thesis, NTH (1995)

[2] G.Backer and J.Szekely: *The interaction of a DC transferred arc with a melting metal: Experimental measures and mathematical description*, Metallurgical Transactions B, Vol.18 B, pp.93-104 (1987)

[3] J.A.Bakken:*Modelling of fluid flow, heat transfer and diffusion in arcs*, High Temp. Chem. Processes 3 (1994)

[4] M.S.Benilov et al: *Vaporization of a solid surface in an ambient gas*, J.Phys D:Appl.Pys 34 (2001)

[5] R.B.Bird, W.E.Stewart, E.N.Lightfoot: *Transport Phenomena 2nd Edition*, John Wiley & Sons inc. (2002)

[6] A.Blais, P.Proulx and M.I.Boulos: *Three-dimensional numerical modelling of a magnetically defelcted dc transferred arc in argon*, J.Phys.D: Appl.Phys, Vol.36, pp.488-496 (2003)

[7] T.K.Bose: *On interaction of gas cross-flow with electromagnetic fields*, Plasma Phys. 15 (1973)

[8] A.B.Cambel: *Plasma Physics and Magnetofluidmechanics*, McGraw-Hill (1963)

[9] F.F.Chen: *Plasma Physics and Controlled Fusion* 2nd ed., Plenum Press (1984)

[10] Xi Chen and He-Ping Li: *On the two-temperature modelling of thermal plasma systems*, lecture and paper ISPC-17, Toronto, Canada (2005)

[11] V.Colombo et al. *Time-dependent 3-D Numerical simulation of transferred arc plasma treatment*, ISPC-17, Toronto, Canada (2005)

[12] V.Colombo et al. *Three-dimensional modelling of inductively coupled plasma tourches*, Lecture and paper ISPC-16, Taormina, Italy (2003)

[13] S.Coulombe *Probabilistic modelling of the high-pressure arc cathode spot displacement dynamic*, J.Phys. D:Appl.Phys 36 (2003)

[14] C.Delalondre et al. *Turbulence modelling in electric arc*, proceedings of Intl. symp. on heat and mass transf. under plasma cond (editor P.Fauchais), Begell House Inc. (1995)

[15] C.Delalondre et al. *Fluid dynamic modelling of electric arcs for industrial applications*, ISPC-13, Beijing, China (1997)

[16] C.Delalondre et al. *3D Fluid dynamic modelling of electric arcs*, ISPC-14, Prague, Czech Republic (1999)

[17] R.S.Devoto *Simplified expressions for the transport properties of ionized monoatomic gases*, Phys.Fluids, Vol.10 p.2105 (1967)

[18] A.M.Essiptchouk, A.Marotta, L.I.Sharakovsky: *The electric field and voltage in a magnetically driven arc burning between coaxial electrodes*, Conference paper, TPP-7, Strasbourg (2002)

[19] A.M.Essiptchouk, A.Marotta, L.I.Sharakovsky: *The effect of arc velocity on cold electrode erosion*, Physics of Plasmas, Vol.11 nr.3 (2004)

[20] A.M.Essiptchouk, A.Marotta, L.I.Sharakovsky: *On the effect of arc current, arc velocity and electrode temperature on cold electrode erosion*, TPP-7, Strasbourg (2002)

[21] P.Fauchais, M.I.Boulos, E.Pfender: *Thermal Plasmas Fundamentals and Applications*, vol.1, Plenum Press, New York (1994)

[22] Fluent Inc: *Fluent 6.1 UDF Manual*, Fluent Inc (2003)

[23] Fluent Inc: *Fluent 6.1 MHD package Manual*, Fluent Inc (2003)

[24] L.Fulcheri et al. *Synthesis of carbon nanomaterials by thermal arc plasma*, lecture and paper ISPC-17, Toronto, Canada (2005)

[25] A.Fridman et al: *Gliding arc gas discharge*, Progress in Energy and Combustion Science, Vol.25 no.2, pp.211-231 (1998)

[26] E.Ghedini and V.Colombo: *Time-dependent 3-D simulation of a DC non-transferred arc plasma torch: Anode attachment and downstream region effects*, lecture and paper ISPC-17, Toronto, Canada (2005)

[27] J.J.Gonzalez et al: *Numerical modelling of an electric arc and its interaction with the anode: part II. The three-dimensional model - influence of external forces on the arc column*, J.Phys.D: Appl.Phys, Vol.38, pp.306-318 (2005)

[28] J.J.Gonzalez, P.Freton and A.Gleizes: *Comparisons between two- and three-dimensional models: gas injection and arc attachment*, J.Phys.D: Appl.Phys, Vol.35, pp.3181-3191 (2002)

[29] J.Gonzalez-Aguilar et al. *Analysis of the motion of a three-phase plasma arc*, Paper ISPC-16, Taormina, Italy (2003)

[30] Liping Gu: *Transport Phenomena in Silicon Vapour Inflitrated Argon Arcs and Anodic Metal Pools*,Dr.Ing thesis, NTH (1993)

[31] Liping Gu:*CHECOMP*, software for computing chemical composition and transport properties for He-C mixtures (2002)

[32] N.Holt: *A metallurgical reactor with three plasma torches, numerical simulation and experimental results*, Dr.Ing Thesis, NTH (1994)

[33] K.C.Hsu, K.Etemadi and E.Pfender: *Study of the free-burning high-intensity argon arc*, J.Phys D: Appl.Phys., Vol.54, No.3, pp.1293-1301 (1983)

[34] P.Kovitya and J.J.Lowke: *Two-dimensional analysis of fre burning arcs in argon*, J.Phys D: Appl.Phys., Vol.12, pp.53-70 journal (1985)

[35] He-Ping Li, J.Heberlein and E.Pfender:*Three-dimensional modelling of non-equilibrium effects in a transferred DC arc plasma with lateral gas blowing* , lecture and paper ISPC-17, Toronto, Canada (2005)

[36] A.Kaddani et al: *Three-dimensional modelling of unsteady high-pressure arcs in argon*, J.Phys.D: Appl.Phys, Vol.28, pp.2294-2305 (1995)

[37] M.Karasik: *Driven Motion and Instability of an Atmospheric Pressure Arc*, PhD Thesis, Princeton University (2000)

[38] M.Kelkar and J.Heberlein: *Physics of an arc in cross flow*, J.Phys. D:Appl.Phys.33 (2000)

[39] J.J.Lowke: *Predicitons of temperature profiles using approximate emission coefficients for radiation losses*, Jour.Quant.Spectrosc.Radiat.Transfer, Vol.14, pp.111-122 (1974)

[40] Hilde Løken Larsen: *AC Electric Arc Models for a laboratory set-up and a silicon metal furnace*, Dr.Ing thesis, NTH (1996)

[41] H.Maecker: *Plasmaströmungen in Lichtbögen infolge eigenmagnetischer Kompression*, Zeitschr.Physik, Vol.141, pp.198-216 (1955)

[42] J.McKelliget and J.Szekely: *Heat transfer and fluid flow in the welding arc*, Metalurgical Transactions A, Vol.17 A, pp.1139-1148 (1986)

[43] E.Meillot, .Guenadou, A.Saget:*Time-dependent D.C. plasma flow modelling*, ISPC-17, Toronto, Canada (2005)

[44] K.A.Naylor and A.E.Guile: *The effective drag width of short moving arcs in argon*, Br.J.App.Phys. 18 (1967)

[45] E.Pfender et al. *Prediction of the anode root position in a DC arc plasma torch*, Lecture and paper ISPC-16, Taormina, Italy (2003)

[46] E.Pfender: *Thermal plasma technology: Where do we stand, and where are we going?*, Plasma Chem. Plasma Proc. Vol.19, No.1 (1999)

[47] S.Ramakrishnan, A.D.Stokes, J.J.Lowke: *An approximate model for high-current free-burning arcs*, J.Phys D: Appl.Phys., Vol.11, pp.226-2280 (1987)

[48] H.Schildt: *C:The Complete Reference*, 4th ed., Osborne/McGraw-Hill (2000)

[49] V.Sevastyanenko: software for computing chemical composition and radiation data for He-C mixtures (2002)

[50] V.G.Sevastyanenko: *Radiative gas-dynamics in multicomponent plasma*, proceedings of the Intl. Symposium on Heat and Mass Transfer under Plasma Conditions, Cesme, Turkey, pp.45-51 (1994)

[51] Gudrun A Sævarsdottir: *AC High Current AC Arcs in Silicon and Ferrosilicon Furnaces*, Dr.Ing thesis, NTNU (2002)

[52] G.Sævarsdottir, H.Palsson, M.Jonsson, J.A.Bakken: *Final Report for the project "Arc Electrode Interactions"*, University of Iceland, 2004

[53] R.N.Szente, R.J.Munz, M.G.Drouet: *The influence of the cathode surface on the movement of magnetically driven electric arcs*, J.Phys. D:Appl.Phys.23 (1990)

[54] J.P.Trelles, E.Pfender and J.V.R.Heberlein: *Three-dimensional finite-element modelling of dynamic behaviour in a DC plasma torch*, IEEE Intl. conference on plasma science 2006, Traverse City, Michigan (2006)

[55] J.P.Trelles, J.V.R.Heberlein and E.Pfender: *Numerical modelling of flow instabilities in direct current plasma torches*, http://www.me.umn.edu/labs/highT/projects/juan/juan.htm

[56] T.Toh at al.: *Magnetohydrodynamic simulation in steelmaking process by the 3D finite volume method*, 4th intl. conf. on CFD in the oil and gas, metallurgical and process industries, Trondheim, Norway (2005)

[57] A.Westermoen and B.Ravary: *Simulations of gas flow in the PPM reactor*, Sintef report STF24 F03545 (2003)

[58] A.Westermoen: *Simulations of gas and particle flow in the PPM reactor*, Sintef report STF80MK F05384 (2005)

[59] A.Westermoen, B.Ravary, J.A.Bakken: *A comparison of the 'source domain' and the magneto-fluiddynamical models to characterize a DC plasma reactor*, ISPC-17, Toronto, Canada (2005)

[60] A.Westermoen: *Simulations of temperature and gas flow in an upscaled PPM reactor*, Sintef report STF80MK F06062 (2006)

[61] S.Zweben and M.Karasik: *Laboratory Experiments on Arc Deflection and Instability*, PPPL Report 3441, Princeton Plasma Physics Laboratory (2000)

[62] US Provisional Application US 60/690,863 regarding carbon nanotube production (2005)

[63] Norwegian patent application no.2005 6149 *Method and reactor for producing carbon nanotubes* (2005)

[64] PCT application PCT/NO06/00229 *Method and reactor for producing carbon nanotubes* (2006)

Appendix A

Basic source code for the VP model

The current source code for the VP model is far to extensive to include here. The code in this appendix is a stripped-down version showing the basic structures for defining material properties and boundary conditions plus all the source terms that go into the equation set.

```
// ************************************************************************
// * UDF for 3D Vector-Potential MFD Plasma Model
// * started june 05 Andreas Westermoen
// * edited and stripped-down example version nov 06

// * gamma and material properties function of T only (not P), mu = mu0

// * INDEX:
// * 0-include statements and constants
// * 1-example of material properties
// * 2-example UDS macros
// * 3-example source term macros
// * 4-example boundary condition
// ************************************************************************

// * UDS numbering: #4 total#
// *  0-2: Vector Potential (A) x,y,z components
// *  3:Scalar Potential (Phi)

// * UDM numbering:
// *  0-2: lorentz forces x,y,z
// *  3: ohmic heating (scalar)
// *  4:sigma (redundant)
// *  5-7: B-field x,y,z
```

```
// *  8-10: j-vector x,y,z
// *  11: total "heating"
// *  13: J^2
// *  15: e_diff term
// *  16: S_eqy; total heating
// ************************************

// --------- 0: include statements and constants ----------
#include "udf.h"
#include "math.h"

// * constants are included at this point, such as:
#define mu0            1.2566E-6  //Magnetic permeability of vacuum
#define TABLESIZE  59

// ----------- 1: example material property -------------
// Several properties can be entered through the Fluent 6.1 user-defined database
// Input: cell and thread id (c,t). Returns interpolated value from the table.

DEFINE_PROPERTY(Argon_density, c,t)
{
 double T;
 double table[TABLESIZE][2]={  //table of computed density data for Argon at 1bar
  {1000,4.87E-01},{1500,3.25E-01},{2000,2.44E-01},{2500,1.95E-01},{3000,1.62E-01},
  {3500,1.39E-01},{4000,1.22E-01},{4500,1.08E-01},{5000,9.74E-02},{5500,8.86E-02},
  {6000,8.12E-02},{6500,7.49E-02},{7000,6.96E-02},{7500,6.49E-02},{8000,6.08E-02},
  {8500,5.71E-02},{9000,5.38E-02},{9500,5.06E-02},{10000,4.77E-02},{10500,4.48E-02},
  {11000,4.19E-02},{11500,3.90E-02},{12000,3.60E-02},{12500,3.30E-02},{13000,3.00E-02},
  {13500,2.71E-02},{14000,2.45E-02},{14500,2.21E-02},{15000,2.01E-02},{15500,1.85E-02},
  {16000,1.72E-02},{16500,1.62E-02},{17000,1.53E-02},{17500,1.47E-02},{18000,1.41E-02},
  {18500,1.36E-02},{19000,1.31E-02},{19500,1.27E-02},{20000,1.23E-02},{20500,1.19E-02},
  {21000,1.15E-02},{21500,1.11E-02},{22000,1.07E-02},{22500,1.03E-02},{23000,9.89E-03},
  {23500,9.46E-03},{24000,9.02E-03},{24500,8.60E-03},{25000,8.19E-03},{25500,7.80E-03},
  {26000,7.44E-03},{26500,7.12E-03},{27000,6.83E-03},{27500,6.57E-03},{28000,6.34E-03},
  {28500,6.13E-03},{29000,5.94E-03},{29500,5.78E-03},{30000,5.62E-03}
 };
 int n;
 double x[2],y[2],rho;
 T=C_T(c,t);
 for(n = 0; n < TABLESIZE-1; n++){
    if((T > table[n][0]) && (T <= table[n+1][0])){
        x[0]=table[n][0];
        x[1]=table[n][1];
        y[0]=table[n+1][0];
        y[1]=table[n+1][1];
  rho=(y[1]-x[1])/(y[0]-x[0])*(T-x[0])+x[1];
    }}
 return rho;
```

```
}

// ------------ 2: UDS Macros ---------------
// The el.conductivity (sigma) acts as diffusivity in the Phi-equation.
// UDS_FLUX can be set to zero for the cases presented in this work
// here is the basic version of argon_sigma macro. no LTE-fix is made here.

DEFINE_DIFFUSIVITY(Ar_sigma, c, t, i)
{
 if (i==3)  //if(equation = Phi-equation)
 {
 double sigma [TABLESIZE][2]={
  {1000,1},{1500,1},{2000,1},{2500,1},{3000,1},{3500,1},{4000,1},
  {4500,1.21E+00},{5000,5.91E+00},{5500,2.43E+01},{6000,6.88E+01},
  {6500,1.64E+02},{7000,3.20E+02},{7500,5.67E+02},{8000,9.06E+02},
  {8500,1.32E+03},{9000,1.78E+03},{9500,2.27E+03},{10000,2.78E+03},
  {10500,3.30E+03},{11000,3.82E+03},{11500,4.35E+03},{12000,4.89E+03},
  {12500,5.41E+03},{13000,5.93E+03},{13500,6.42E+03},{14000,6.88E+03},
  {14500,7.31E+03},{15000,7.71E+03},{15500,8.07E+03},{16000,8.41E+03},
  {16500,8.72E+03},{17000,9.02E+03},{17500,9.31E+03},{18000,9.58E+03},
  {18500,9.84E+03},{19000,1.01E+04},{19500,1.03E+04},{20000,1.05E+04},
  {20500,1.07E+04},{21000,1.08E+04},{21500,1.09E+04},{22000,1.09E+04},
  {22500,1.09E+04},{23000,1.08E+04},{23500,1.08E+04},{24000,1.07E+04},
  {24500,1.06E+04},{25000,1.05E+04},{25500,1.04E+04},{26000,1.04E+04},
  {26500,1.04E+04},{27000,1.04E+04},{27500,1.05E+04},{28000,1.06E+04},
  {28500,1.07E+04},{29000,1.08E+04},{29500,1.09E+04},{30000,1.10E+04}
 };
 real Jx,Jy,Jz;
 double temp = C_T(c,t);   //possible to overwrite in a non-LTE zone
 double x[2],y[2];
 double sigmaval=1.0;
 int n;

 for(n = 0; n < TABLESIZE-1; n++){
    if((temp > sigma[n][0]) && (temp <= sigma[n+1][0])){
      x[0]=sigma[n][0];
      x[1]=sigma[n][1];
        y[0]=sigma[n+1][0];
        y[1]=sigma[n+1][1];
     sigmaval=(y[1]-x[1])/(y[0]-x[0])*(temp-x[0])+x[1];
    }
 }
 C_UDMI(c,t,4)=sigmaval;
 return sigmaval;
}
else {return 1;}   //the A-component equations have diffusivity 1
}
```

```
// --------- 3: Source Term Macros ----------
// Source terms:lorentz forces, ohmic heating plus source terms for A-field equation
// Source term for Phi-equation can be neglected for low magnetic Reynolds number
// Effects of external magentic field can easily be hardcoded into the Fx-routine

DEFINE_SOURCE(Fx, c, t, dS, eqn)
{
 real Bx,By,Bz,Jx,Jy,Jz,JJ,Fx,Fy,Fz,sigma;
 real x[ND_ND];

 sigma=C_UDSI_DIFF(c,t,3);
 F_CENTROID(x,c,t);
 Jx=-sigma*C_UDSI_G(c,t,3)[0];
 Jy=-sigma*C_UDSI_G(c,t,3)[1];
 Jz=-sigma*C_UDSI_G(c,t,3)[2];
 JJ=Jx*Jx+Jy*Jy+Jz*Jz;
 Bx=C_UDSI_G(c,t,1)[2]-C_UDSI_G(c,t,2)[1];
 By=C_UDSI_G(c,t,2)[0]-C_UDSI_G(c,t,0)[2];
 Bz=C_UDSI_G(c,t,0)[1]-C_UDSI_G(c,t,1)[0];

 //F=JxB *effects of external field is added here*
 Fx=Jy*Bz-Jz*By;
 Fy=Jz*Bx-Jx*Bz;
 Fz=Jx*By-Jy*Bx;

 C_UDMI(c,t,0) = Fx;
 C_UDMI(c,t,1) = Fy;
 C_UDMI(c,t,2) = Fz;
 C_UDMI(c,t,5) = Bx;
 C_UDMI(c,t,6) = By;
 C_UDMI(c,t,7) = Bz;
 C_UDMI(c,t,8) = Jx;
 C_UDMI(c,t,9) = Jy;
 C_UDMI(c,t,10)= Jz;
 C_UDMI(c,t,13)= JJ;
 return Fx;
}
DEFINE_SOURCE(Fy, c, t, dS, eqn)
{
 return C_UDMI(c,t,1);
}
DEFINE_SOURCE(Fz, c, t, dS, eqn)
{
 return C_UDMI(c,t,2);
}

DEFINE_SOURCE(VP_egy_Ar, c, t, dS, eqn)
```

```
{
 double T,sigma,dTdx,dTdy,dTdz,Jx,Jy,Jz,JJ,Q,e_diff,Srad,source;

 static double a[52][2]= {  //computed radiation data for argon
  {1000,0},{5000,2.13E-02},{5500,2.54E-01},{6000,8.88E+02},{6500,6.61E+03},
  {7000,8.60E+04},{7500,5.18E+05},{8000,1.95E+06},{8500,5.82E+06},
  {9000,1.54E+07},{9500,3.63E+07},{10000,7.79E+07},{10500,1.55E+08},
  {11000,2.88E+08},{11500,5.00E+08},{12000,8.18E+08},{12500,1.25E+09},
  {13000,1.80E+09},{13500,2.41E+09},{14000,3.06E+09},{14500,3.67E+09},
  {15000,4.20E+09},{15500,4.66E+09},{16000,5.03E+09},{16500,5.39E+09},
  {17000,5.83E+09},{17500,6.29E+09},{18000,6.90E+09},{18500,7.67E+09},
  {19000,8.62E+09},{19500,9.79E+09},{20000,1.12E+10},{20500,1.28E+10},
  {21000,1.48E+10},{21500,1.68E+10},{22000,1.93E+10},{22500,2.18E+10},
  {23000,2.45E+10},{23500,2.75E+10},{24000,3.05E+10},{24500,3.30E+10},
  {25000,3.51E+10},{25500,3.74E+10},{26000,3.95E+10},{26500,4.12E+10},
  {27000,4.27E+10},{27500,4.43E+10},{28000,4.54E+10},{28500,4.65E+10},
  {29000,4.75E+10},{29500,4.86E+10},{30000,4.989E+10}};
 double x[2],y[2];
 int n;

 T=C_T(c,t);
 dTdx=C_T_G(c,t)[0];
 dTdy=C_T_G(c,t)[1];
 dTdz=C_T_G(c,t)[2];
 Jx=C_UDMI(c,t,8);
 Jy=C_UDMI(c,t,9);
 Jz=C_UDMI(c,t,10);
 JJ=C_UDMI(c,t,13);

 dS[eqn]=0.0;
 sigma=C_UDSI_DIFF(c,t,3);

 //calculate heat source including electron diffusion and radiation
 e_diff=5*1.38066E-23/(2*1.602177E-19)*(Jx*dTdx+Jy*dTdy+Jz*dTdz);

 for(n = 0; n < 26; n++){
     if((T > a[n][0]) && (T <= a[n+1][0])){
 x[0]=a[n][0];
       x[1]=a[n][1];
       y[0]=a[n+1][0];
       y[1]=a[n+1][1];
    Srad=(y[1]-x[1])/(y[0]-x[0])*(T-x[0])+x[1];
    }}
 C_UDMI(c,t,3)=Q;
 C_UDMI(c,t,11)=Srad;
 source=Q+e_diff-Srad;
 C_UDMI(c,t,16)=source;
 return source;
```

```
}

DEFINE_SOURCE(Ax_src, c, t, dS, eqn)
{
 real source;
 source= -mu0*C_UDMI(c,t,8);
 return source;
}

DEFINE_SOURCE(Ay_src, c, t, dS, eqn)
{
 real source;
 source= -mu0*C_UDMI(c,t,9);
 return source;
}

DEFINE_SOURCE(Az_src, c, t, dS, eqn)
{
 real source;
 source= -mu0*C_UDMI(c,t,10);
 return source;
}


// --------- 4: Example Boundary condition ----------

DEFINE_PROFILE(parabol1kA, t,i)
{
// parabolic profile j(r)=A(1-r^2/R^2)  where the constant A = 3/4 J/pi R^2
// grad Phi = j / sigma, but sigma at cathode spot is set to 1 because wall is cold
// flux = n dot (- sigma ddxi Phi) = jz

 real xvec[ND_ND];
 real r;
 face_t f;
 real R=0.005; //cathode spot radius
 real Jtot=1000;
 real A=2*Jtot/M_PI/R/R;

 begin_f_loop(f,t){
F_CENTROID(xvec,f,t);
r=sqrt(xvec[0]*xvec[0]+xvec[1]*xvec[1]);
if(r<R){
  F_PROFILE(f,t,i)=A*(1-r*r/R/R);}
else{
  F_PROFILE(f,t,i)=0;}
 }end_f_loop(f,t)
}
```

Appendix B

Characteristic radiation absorption length

In the Lowke approximation (ch.2.3.4), the same characteristic absorption radius R_{eff} is used for the whole arc. In this work a constant radius of 8.9 mm was used in all the cases presented. The non-obvious choice of 8.9 mm (rather than say 10 mm) is because the IMPC code output is given for equidistant values of y=log(r).

For the full IMPC model, the reabsorption is calculated explicitly, and no characteristic radius is needed. However, as the Lowke method is so much faster, it is still interesting to use it for fast approximations. The results from rotating arcs show that even though the arc expands and gets a larger cross-section area, the drag forces can flatten it so that the actual absorption radius may in fact become much smaller when averaging over all directions.

The figure B.1 illustrates how the net emitted radiation depends on the absorption radius for the Lowke method. It is obvious that a flattened arc will have a larger radiation loss and thus may get more constricted (and thus even flatter).

However, the model is not overly sensitive to this parameter: a factor 2 shorter absorption radius only gives about 10 percent higher radiation loss. The effect of including the reabsorption rather than assuming an optically thin plasma is on the other hand large. The conclusion is then that the Lowke radiation model performs better than other simple models with comparable computational costs.

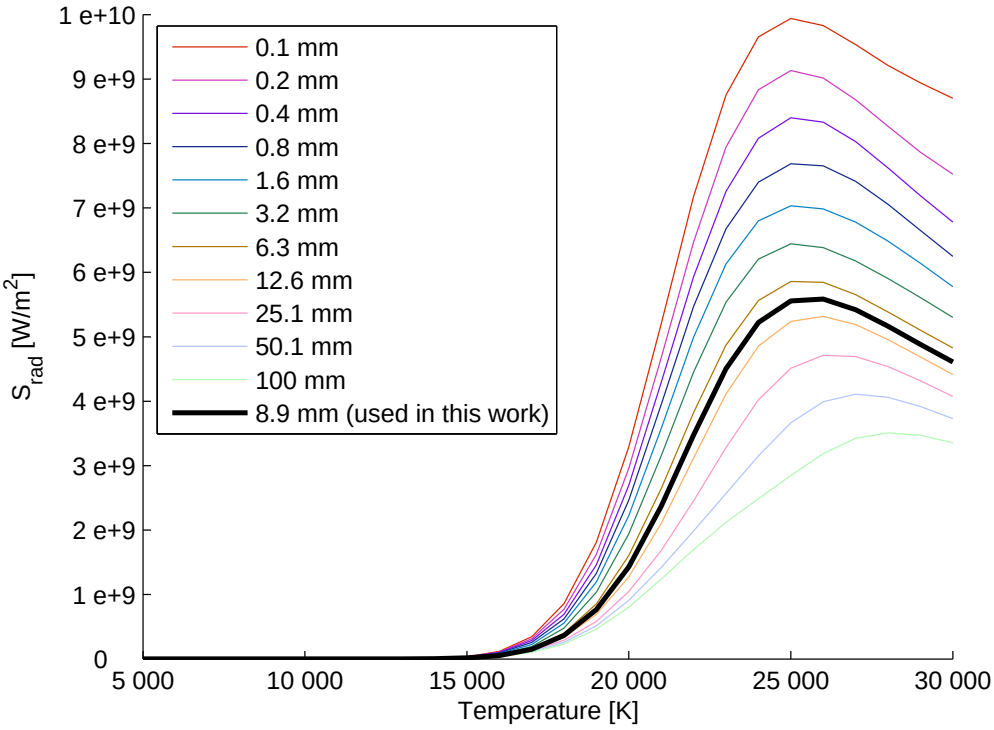

Figure B.1: Computed Lowke method radiation data S_{rad}[W(m^3] for different characteristic absorption radii R_{eff} in a 0.6 bar He plasma. For the computations in this work, a radius r=8.9 mm was used (fat line)

Appendix C

Scott-T transformer

The Scott-T transformer (Scott connection) is used for converting three-phase to two-phase or vice versa. Figure (C.1) shows the basic circuit diagram. The transformer connection consists of a center-tapped 1:1 ratio transformer T1 and a $\frac{1}{2}\sqrt{(}5)$ ratio transformer T2. The center tapped side of T1 is connected between two phases on the 3 phase side (Y2, Y3). The lower turn count side of T2 connects to the center tap of T1 and to the remaining phase (Y1). The other sides of the transformers (R1-R4) are connected directly to the two pairs of a two-phase 4 wire system.

To sum up, a three-phase current into Y1-Y3 generates a two-phase current in R1-R4 or the other way around. This means a two-phase magnetic field easily can be run on a three-phase power supply by just adding a Scott-T transformer.

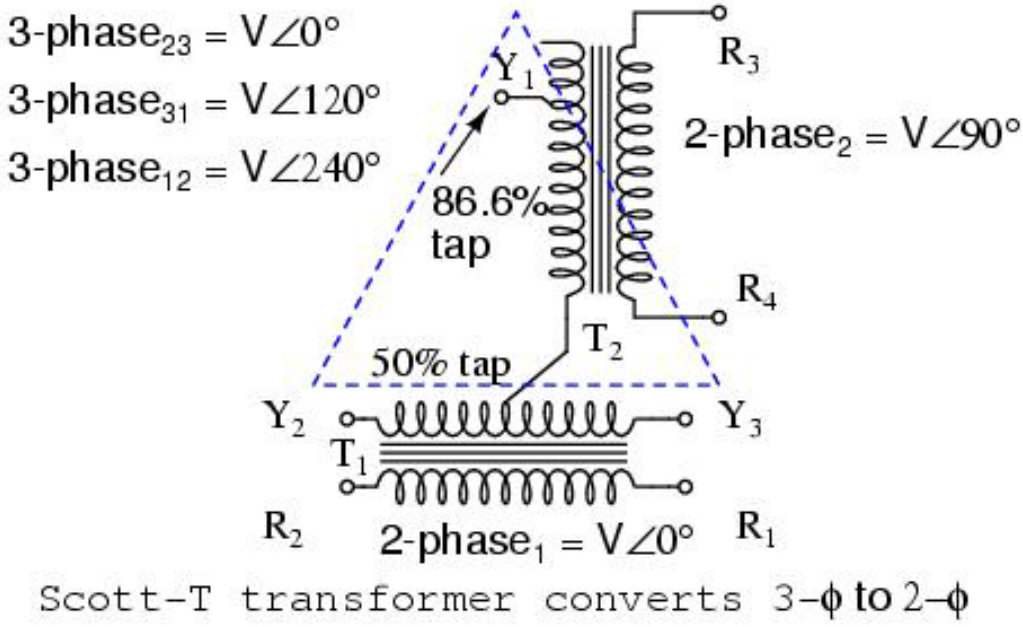

Figure C.1: Scott-T transformer circuit diagram. Source: wikipedia (http://en.wikipedia.org/wiki/Scott-T_transformer)

Appendix D

Computed external magnetic field in the PPM reactor

These plots show computed magnetic fields for two different coil setups in the real PPM reactor. One setup is the one currently used in the PPM reactor, the other is one of several other possible setups. The computations were made using FEMLAB 3.0, now called COMSOL Multiphysics.

Note that the magnetic field strength in all cases scales proportionally to the total current, so that *the shape of the field depends only on the position of the coils and the distribution of current (actually current times number of windings) between them.* Computed field strengths should then not be compared across different plots as they can easily be scaled to match. The critical parameter is the shape of the plot (the spatial field distribution), since it is the sign of the B_r component that determines whether we get a stabilising magnetic bottle effect or not.

In the PPM experiments, focus has been on preventing the arc from short-circuiting to the top of the reactor, as well as to prevent the arc from burning to the substrate. Since the current distribution between the coils, as well as the total current (and hence the rotation speed and centripetal force) can be adjusted dynamically, the anode attachment position can be pushed up or down.

There are five basic possibilities, with variations: If the B_r has the same sign in the whole reactor, there will be a force pushing the rotating arc up or down. If the B_r changes sign, then the force either pushes the arc towards the $B_r = 0$ position (magnetic bottle) or away from it. Finally, if B_r is zero or very close to it, so is the resulting force. For the two cases where the sign changes, the position of the change determines the stable or unstable equilibrium position. However, due to the centripetal force of the rotating arc pushing it upwards, the equilibrium anode at-

tachment position also depends on rotation speed (and thus depends on the material properties of the plasma gas, the total arc current and the total coil currents).

The computations were done with a set current of 1 Ampere-winding in the top coil and variations in the bottom coil. B_r was plotted along two lines going vertically up from 20 cm below the anode top to 20 cm above it; one along the inner surface of the anode (r=10 cm) and the other along the other surface of the cathode (r=5 cm). Multiplying the obtained magnetic field values by realistic coil currents and winding numbers (and a factor μ_0 to convert between $\vec{B}$ and $\vec{H} where necessary$) gives magnetic field strengths of order 1-10 mT in the arc region, similar to what is used on the modeling.

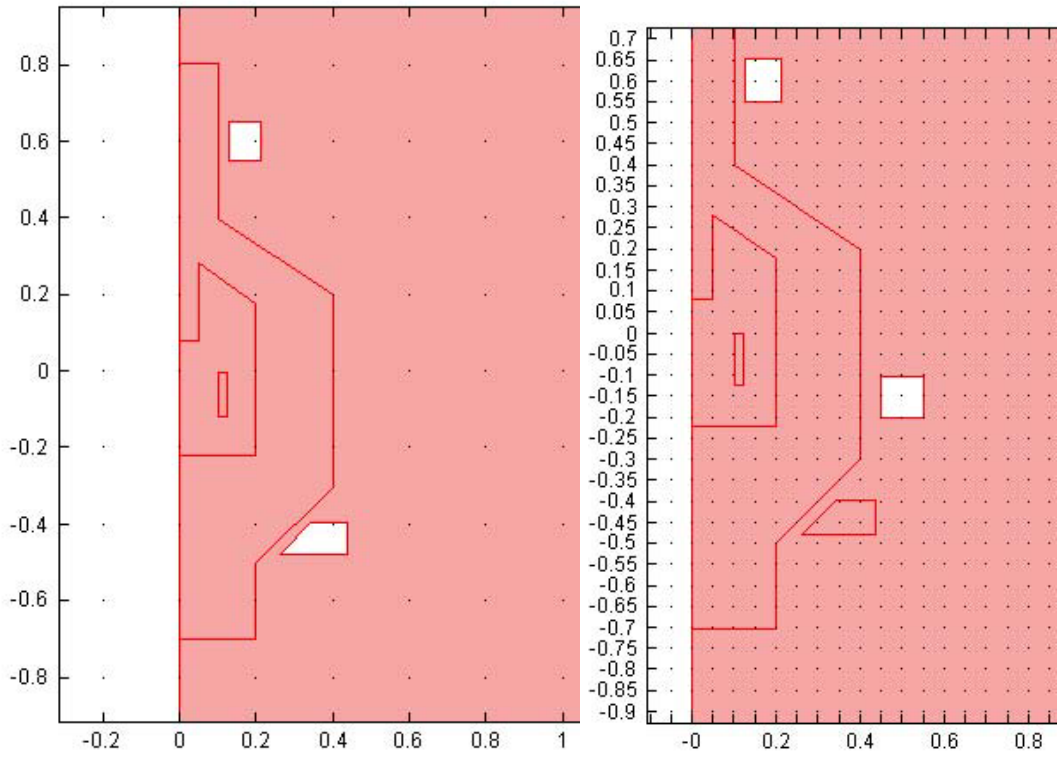

Figure D.1: Coil setup geometries. *Left:* the current PPM setup. *Right:* one of several alternative setups. White areas indicate the coils, red lines illustrate the reactor interior and exterior.

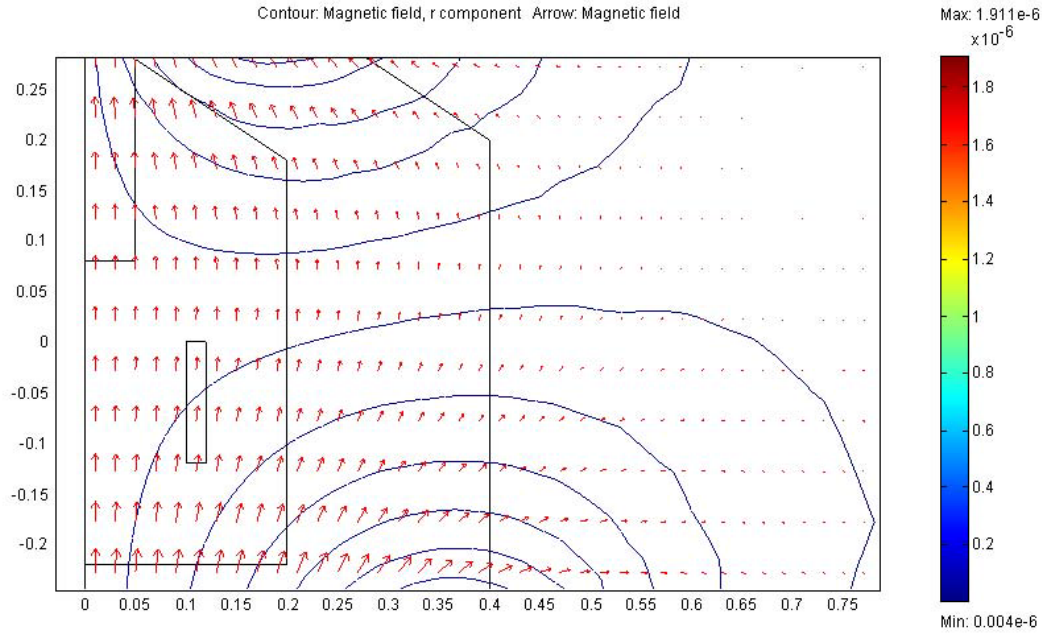

Figure D.2: $\vec{B}$ vectors and B_r contours for setup A: the lower coil has 1/5 the current density of the upper coil.

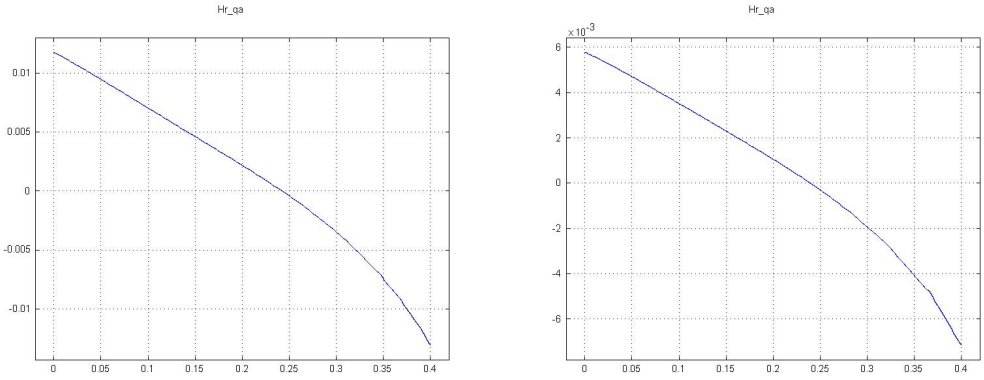

Figure D.3: B_r line plots. Both show a bottle effect centered about 25 cm above the bottom of the line, which is midway between cathode and anode.

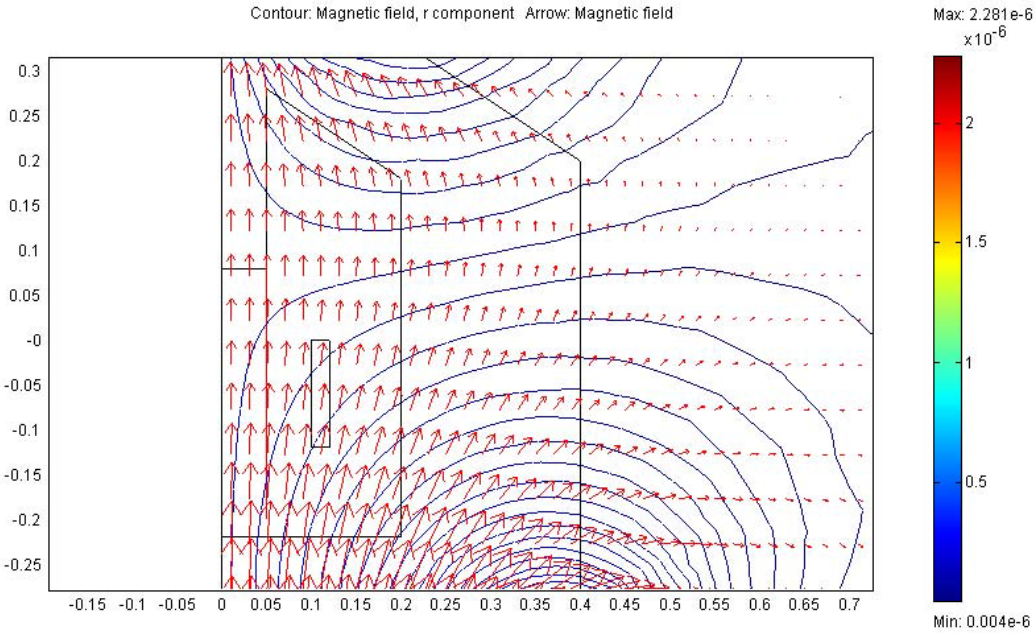

Figure D.4: $\vec{B}$ vectors and B_r contours for setup B: the lower coil has 1/2 the current density of the upper coil.

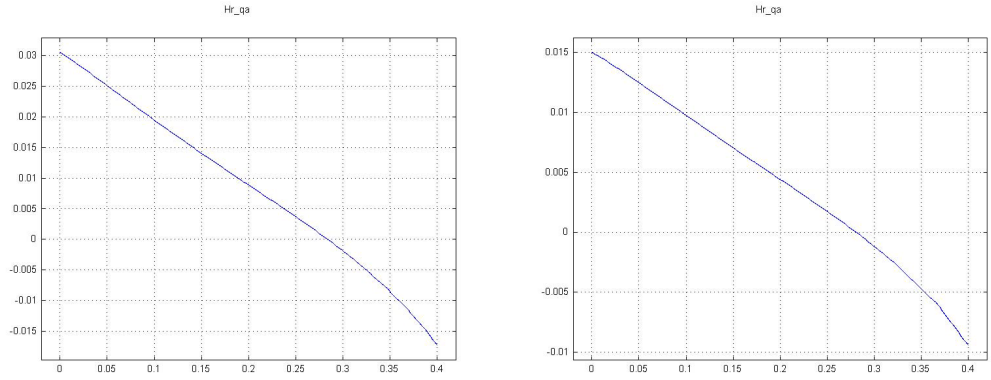

Figure D.5: B_r line plots. Both show a bottle effect centered about 28 cm above the bottom of the line, just below the cathode tip height.

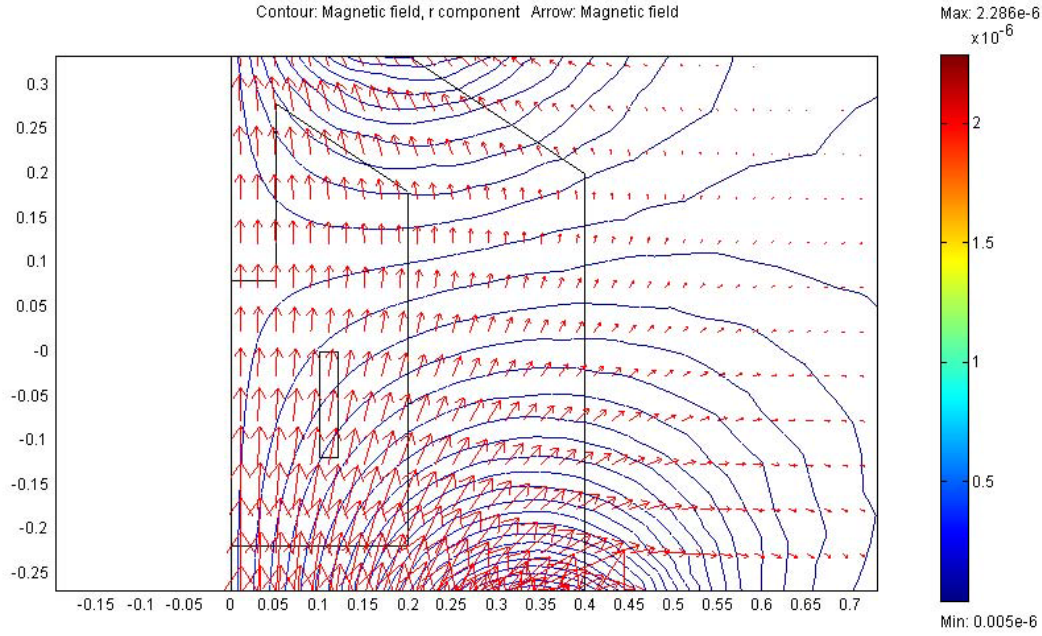

Figure D.6: $\vec{B}$ vectors and B_r contours for setup C: the lower coil has same current density as the upper coil.

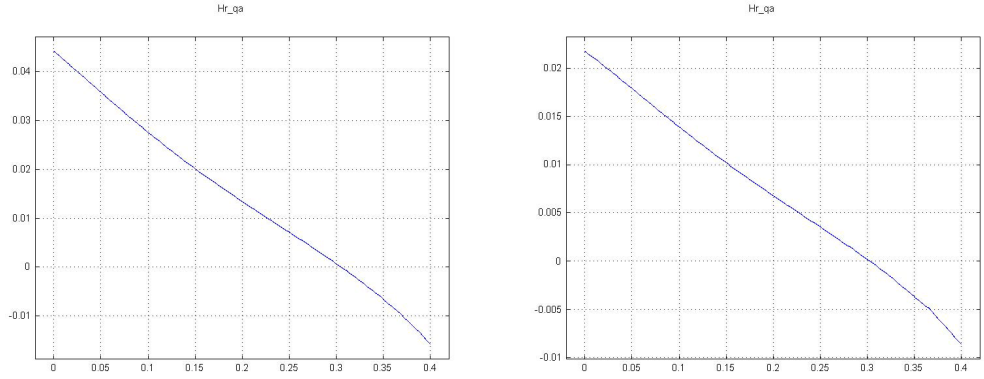

Figure D.7: B_r line plots. Both show a bottle effect centered about 30 cm above the bottom of the line, corresponding to the cathode tip height.

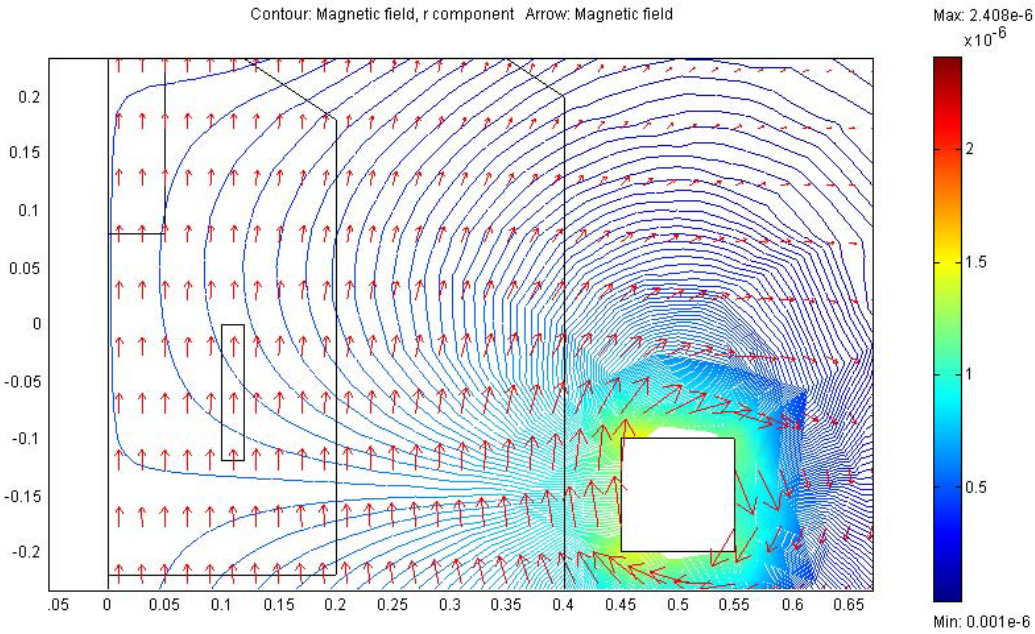

Figure D.8: $\vec{B}$ vectors and B_r contours for setup D: Geometry 2, the lower coil has same current density as the upper coil. The lower coil can be seen in the plot.

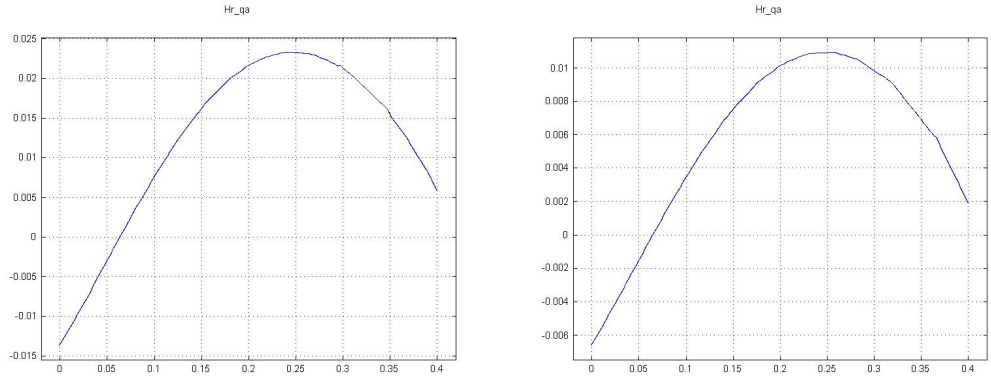

Figure D.9: B_r line plots. Both indicate an unstable equilibrium some 13 cm below the anode top, and hint of a stable equilibrium near the top of the reactor. In the whole relevant zone, a rotating arc will be pushed upwards.

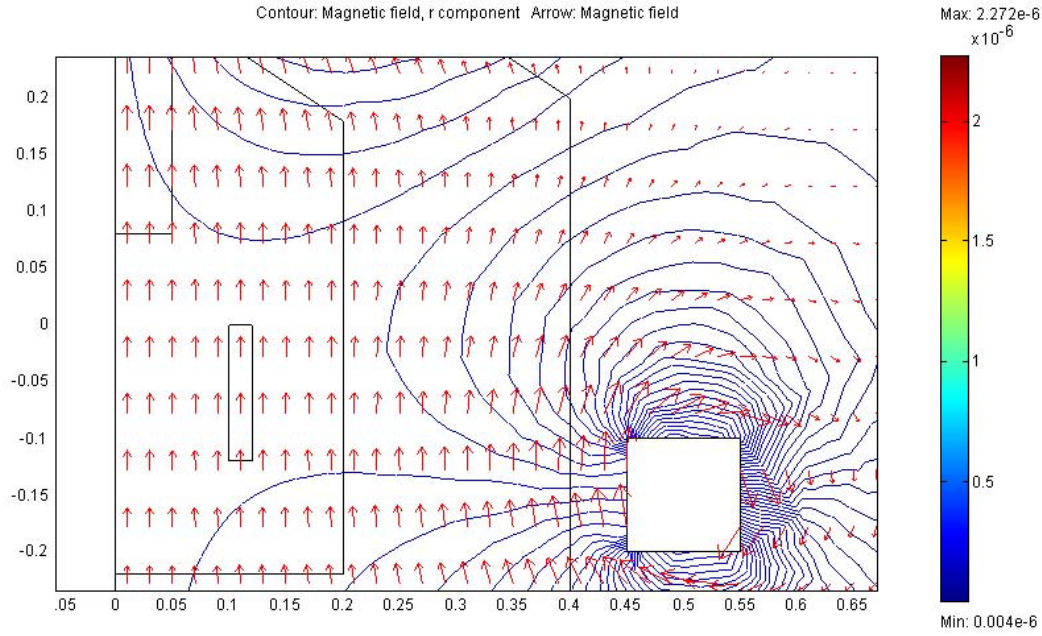

Figure D.10: $\vec{B}$ vectors and B_r contours for setup E: Geometry 2, the lower coil has 1/5 the current density of the upper coil.

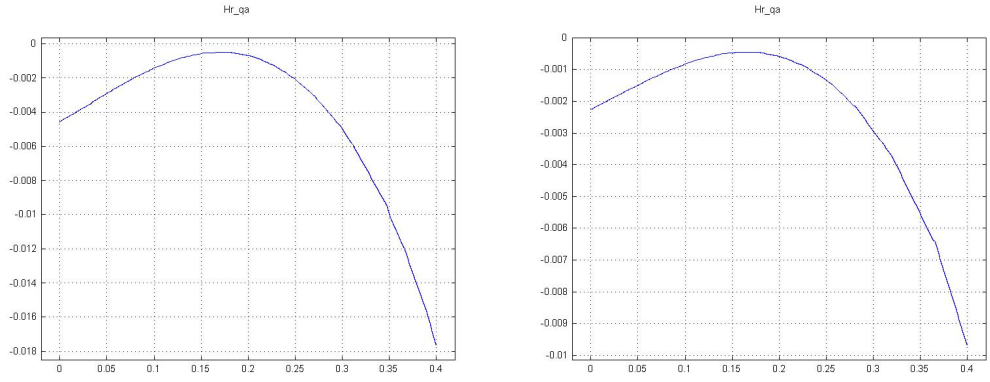

Figure D.11: B_r line plots. No equilibrium points. A rotating arc will be pushed down no matter where it burns. However, the push is much stronger near the reactor top, and weak near the desired anode attachment positions.

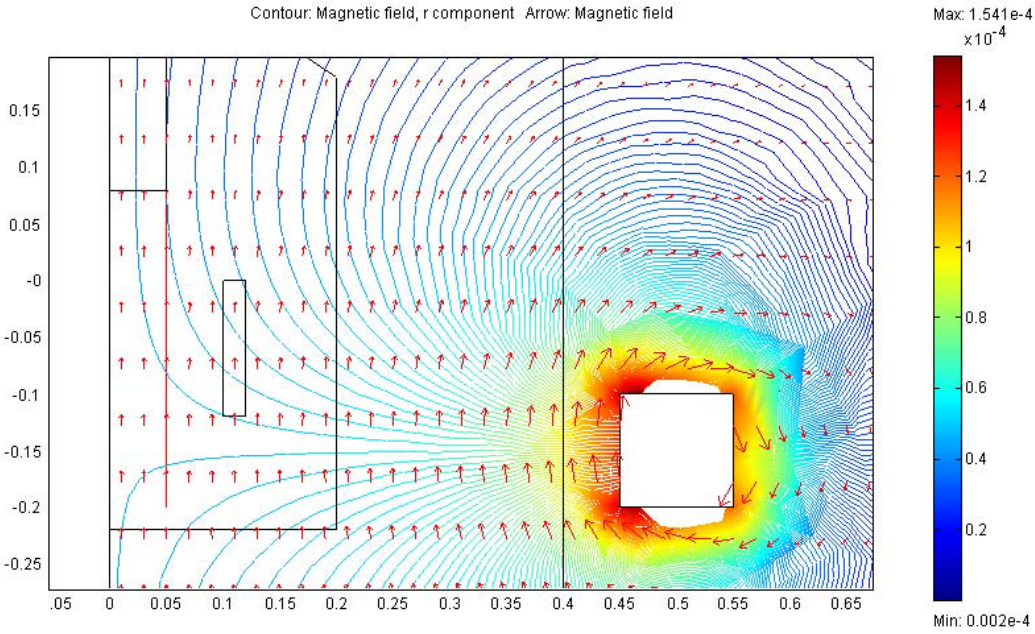

Figure D.12: $\vec{B}$ vectors and B_r contours for setup F: Geometry 2, the lower coil has 99 times the current density of the upper coil: this is essentially a single coil setup.

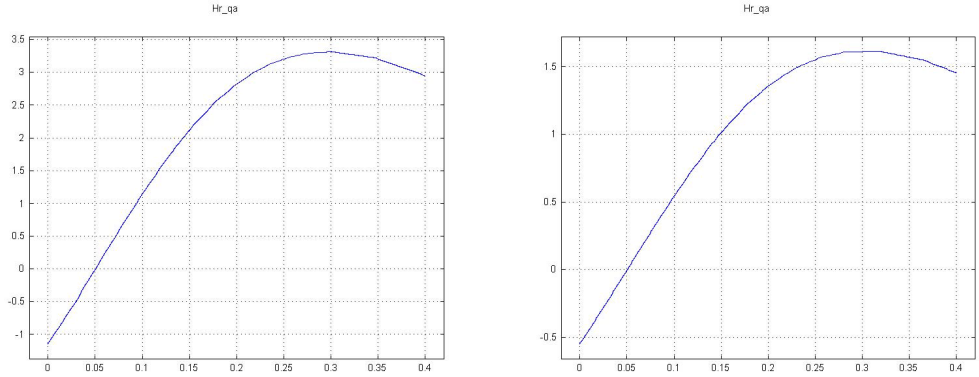

Figure D.13: B_r line plots. Strong unstable equilibrium some 15 cm below the cathode top.

Appendix E

Particle flow in the PPM reactor (SD model)

This work was performed by Dr. Benjamin Ravary for [58], and illustrates how easy it is to add functionality to the SD model: here the fluent DPM (Discrete Particle Mode) is used to compute particle paths in the field computed by the 3D SD-I model.

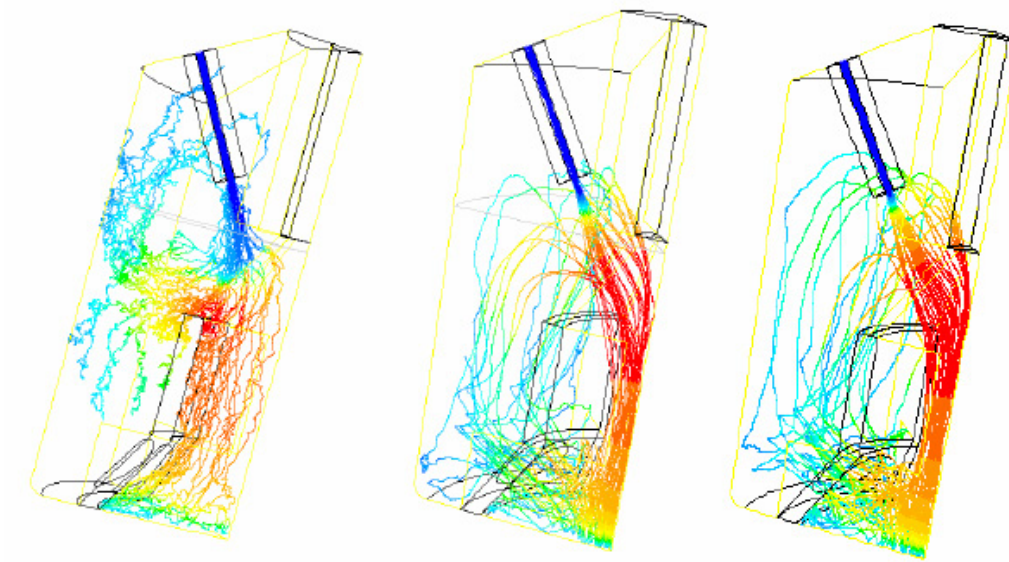

Figure E.1: Computed paths for 40 particles released in the reactor. The different cases correspond to different gas flow rates through the injection lance and in an annular inlet around the cathode. Recirculation patterns are identified for the particles which are not necessarily the same as for the gas itself.